Nanostructure Stabilization and Mechanical Behavior of Binary Nanocrystalline Alloys

by

Jason R. Trelewicz

B.E., Materials Science and Engineering
State University of New York at Stony Brook, 2004

SUBMITTED TO THE DEPARTMENT OF MATERIALS SCIENCE AND ENGINEERING
IN PARTIAL FULFILLMENT OF THE REQUIREMENTS FOR THE DEGREE OF

DOCTOR OF PHILOSOPHY IN MATERIALS SCIENCE AND ENGINEERING
AT THE
MASSACHUSETTS INSTITUTE OF TECHNOLOGY

September 2008

Signature of Author:_____

Department of Materials Science and Engineering
September 11, 2008

Certified by: _____

Christopher A. Schuh
Danae and Vasilios Salapatas Associate Professor of Metallurgy
Thesis Supervisor

Accepted by: _____

Christine Ortiz
Chair, Departmental Committee for Graduate Students

Nanostructure Stabilization and Mechanical Behavior of Binary Nanocrystalline Alloys

by

Jason R. Trelewicz

Submitted to the Department of Materials Science and Engineering on September 12, 2008 in Partial Fulfillment of the Requirements for the Degree of Doctor of Philosophy in Materials Science and Engineering

ABSTRACT

The unique mechanical behavior of nanocrystalline metals has become of great interest in recent years, owing to both their remarkable strength and the emergence of new deformation physics at the nanoscale. Of particular interest has been the breakdown in Hall-Petch strength scaling, which is frequently attributed by atomistic simulations to a mechanistic shift to interface-dominated plasticity. Experimental validation has been less abundant, primarily due to the processing challenges associated with achieving homogeneous nanocrystalline samples suitable for mechanical testing. Alloying has been proposed as a potential route to high-quality nanocrystalline metals, although choice of an appropriate alloy system, based on available thermodynamic data, remains elusive. In this thesis, we propose a thermodynamic model for nanostructure stabilization that derives from the energetic state variables characteristic of binary alloys. These modeling results motivate the study of Ni-W alloys in particular, which may be synthesized via aqueous electrodeposition, accessing grain sizes across the entire Hall-Petch breakdown regime as characterized by x-ray diffraction and transmission electron microscopy. Ambient temperature nanoindentation testing is employed to evaluate the mechanical behavior of the as-deposited alloys, assessing the nature of flow, the rate sensitivity, and pressure sensitivity of deformation, with emphasis on property inflections required to bridge the behavior of nanocrystalline metals to amorphous solids. The rate sensitivity, in particular, demonstrates an inherent dependence on nanocrystalline grain size, exhibiting a maximum in the vicinity of the Hall-Petch breakdown as a consequence of a shift to glass-like shear localization. In light of this finding, we study the Hall-Petch breakdown at high strain rates, and show that an "inverse Hall-Petch" weakening regime emerges at high rates. Additional effects from structural relaxation are investigated, and illustrated to strongly influence the strength scaling behavior and shift to inhomogeneous flow. Relaxed samples are also subjected to elevated temperature indentation tests, and the results discussed in the context of thermally-activated plasticity, thus providing a more quantitative analysis of the nanoscale deformation mechanisms.

Thesis Supervisor: Christopher A. Schuh

Title: Danae and Vasilios Salapatas Associate Professor of Metallurgy

Acknowledgements

I would like to thank the members of my thesis committee, Professor Thomas Eagar, Dr. David Stepp, and Professor Krystyn Van Vliet for their time, insightful discussions, and guidance throughout my graduate career. I am also grateful to have had the opportunity to work with the members of the Schuh research group, both past and present, and would like to especially thank Dr. Andrew Detor, Professor Megan Frary, Dr. Alan Lund, David Fischer, Tim Rupert, Corinne Packard, Eric Homer, Jon Trenkle, Jeremy Mason, Ying Chen, and Shiyun Ruan. These people have provided constructive insight and informative discussions over the years, and have helped make my experience at MIT an enjoyable one.

I would like to especially thank my wife, Lauren Trelewicz, who has always been there for me, no matter what; you are truly my best friend and I can't express enough how much I appreciate everything you've helped me with over recent years. I am extremely grateful to my parents, Ken Trelewicz and Debbie Saparito, for all their inspiration, guidance, and support; you have both pushed me and stood by me when I needed it most, and I thank you for that. I would also like to thank Brian Hohmann and Trey Holtzwarth, who have been great friends since our first thermo class together at MIT. Dr. Jeff Brogan, Jon Gutleber, and Professor Sanjay Sampath have remained good friends and colleagues from my time at SUNY Stony Brook, and their continued support is greatly appreciated. There are a number of friends that I have grown with over the years, and would like to thank for helping me keep a healthy balance between work and life, including Drew Hoelzer, Tom Skoblicki, Chris Jones, Rob Crosby, Ryan DeStefano, Scott Petit, Jeff Duncan, Ryan Bonti, Dominic Briante, Jon Pinola, Greg Levita, Allison Meiselbach, Joe Olive, Mike Gibson, and Mike Burk. I would also like to thank my grandparents, Olga and Teddy Trelewicz, brother Jeff Trelewicz, in-laws Joe, Donna, Lyndsey and Allyson Frank, Kevin Reilly, and step-parents Vicki Trelewicz and Joe Cullen for their great support.

Lastly, I would like to thank my advisor Professor Chris Schuh for everything over the past four years. Chris has challenged me in so many ways, and his positive attitude and creativity have inspired me time and time again. He has taught me so much about performing good research, and instilled the idea in me that anything can be figured out, despite how frustrating or difficult it may appear. Chris has served as a great role model and has been central in all aspects of my professional development. Working with Chris throughout the Ph.D. process has truly been a pleasure, and I will continue to look up to him in the future.

Table of Contents

Acknowledgements **3**
Table of Contents **4**
List of Figures **6**
List of Tables **13**
Chapter 1: Introduction **14**
1.1 Hall-Petch strengthening at the nanoscale: a shift to interface-dominated physics 14
1.2 The Hall-Petch breakdown 18
1.3 Processing and nanostructure stability 22
1.4 Problem statement 26
Chapter 2: Analytical modeling of thermodynamically stable nanocrystalline alloys **28**
2.1 Analytical framework 28
2.1.1 Solution model 28
2.1.2 Bond distribution 31
2.1.3 Free energy function 33
2.1.4 Equilibrium equations 36
2.2 Parametric study 43
2.2.1 Temperature 43
2.2.2 Bulk interaction energy 45
2.2.3 Intergranular interaction energy 47
2.2.4 Solvent grain boundary energy 49
2.2.5 Grain structure dimensionality 51
2.3 Implications for design of stable nanocrystalline alloys 52
2.4 Concluding remarks 54
Chapter 3: Experimental materials **56**
3.1 Electrodeposition procedures 56
3.2 Characterization procedures 58
3.3 As-deposited Ni-W alloys by electrodepositon 59
3.4 Isothermal annealing of Ni-W alloys 62
3.5 Concluding remarks 64
Chapter 4: Mechanical behavior of as-deposited nanocrystalline Ni-W alloys **65**

4.1 Instrumented nanoindentation procedures 66
4.2 Hardness and flow behavior of nanocrystalline Ni-W alloys 67
4.3 Rate sensitivity of deformation 71
4.4 Pressure sensitivity of deformation 74
4.5 Implications 78
4.6 Concluding remarks 80
Chapter 5: The Hall-Petch breakdown at high strain rates 82
5.1 Experimental procedures 82
5.2 Dynamic hardness and the Hall-Petch breakdown at high strain rates 85
5.3 High strain rate flow behavior of nanocrystalline Ni-W alloys 87
5.4 Concluding remarks 89
Chapter 6: Mechanical behavior of heat treated Ni-W alloys 90
6.1 The role of structural relaxation in nanoscale plasticity 91
6.2 Elevated temperature deformation behavior of heat treated Ni-W alloys 96
6.2.1 High-temperature nanoindentation procedures 96
6.2.2 Determination of the activation energy 98
6.2.3 Implications for the underlying deformation mechanisms 101
6.3 Concluding remarks 102
Conclusions 104
Directions for future work 107
Appendix A: Coding script for determining thermodynamically stable states 109
Appendix B: The Hall-Petch breakdown at constant W content 116
Appendix C: Methodology for analyzing high rate indentation data 122
References 131

List of Figures

Figure 1.1: Strength scaling of nanocrystalline Ni from the studies of Erb et al. [18], Hughes et al. [13], and Ebrahimi et al. [11]. A breakdown in the classical Hall-Petch relationship is suggested at a grain size in the range of 10-20 nm.

Figure 1.2: The activation volume for deformation in Ni [10, 47, 54], Ni-Co [53], Cu [46, 48-51, 53], and Cu alloy [49] systems as a function of grain size. Nanocrystalline metals exhibit drastically lower values of V when compared to their microcrystalline counterparts, corresponding to an enhancement in the rate sensitivity.

Figure 1.3: The Mohr-Coulomb coefficient as a function of grain size for pure Ni [57, 60] and Zn [58, 59], and Cu alloys [55, 56]. Finer nanocrystalline metals are more sensitive to pressure down to a grain size of about 20 nm, and an inflection is suggested when the simulation results from Lund et al. [63] are added. A typical value of $\alpha \sim 0.12$ for amorphous solids is included for reference [64, 65].

Figure 1.4: Deformation mechanism map for nanocrystalline metals after Cheng et al. and Lund et al. At large grain sizes, classical dislocation plasticity is expected , which transitions to grain boundary sources of unit and partial dislocations, and ultimately plasticity is confined to the grain boundary regions, e.g. grain boundary sliding. Lund and Schuh [63] have predicted a transition to shear localization at the finest nanocrystalline grain sizes.

Figure 1.5: Gibbs free energy as function of nanoscale grain size for a given solute content, after Weissmuller [177]. A minimum is predicted in the free energy, corresponding to the thermodynamically stable grain size; image courtesy of Dr. A.J. Detor.

Figure 1.6: Scaling of nanocrystalline grain size with alloy composition for the strongly-segregating Ni-P system, and the weakly-segregating Ni-W system, taken from the works of Liu et al. [183] and Detor et al. [77], respectively. A higher alloy composition promotes finer grain sizes, regardless of the segregation tendency.

Figure 2.1: Schematic of an arbitrary grain shape, with the atomic configuration at the interface between the pictured and adjacent grain highlighted. The two planes of atoms at the boundary

between the grains, indicated by the dotted line, are denoted the intergranular region. Intergranular bonds are those located entirely within the intergranular region, and transitional bonds connect these atoms to those in the bulk region.

Figure 2.2: Two dimensional slices of the free energy surface as a function of (a) the intergranular solute content at a grain size of 20 nm, and (b) grain size at an intergranular solute content of 44 at %, for a given global composition of 10 at %. The minimum identified in the free energy of mixing represents the global minimum, and defines the thermodynamically stable state: note that these two sections have been chosen such that they each intersect the true energy minimum, whereas plots of Eq. (2.17) as a function of either variable alone would generally not.

Figure 2.3: Equilibrium grain size as a function of the global solute content for a given set of interaction energies. A power-law-like decay in grain size is observed with increasing global composition, indicating that more solute is required to stabilize finer nanocrystalline grain sizes.

Figure 2.4: Interfacial excess and intergranular solute content plotted against the global solute content; the corresponding axes are indicated. For the given set of interaction energies, both quantities are independent of global composition, and thus denote the critical intergranular coverage level required to achieve equilibrium.

Figure 2.5: Thermodynamic equilibrium states as a function of temperature for interaction energies defined as: ω_b = 0.03 eV, ω_{ig} = 0 eV, and $\gamma_A^o = \gamma_B^o$ = 0.48 J/m^2. With increasing temperature, (a) the segregation energy decreases, (b) the grain size trends first shift to higher solute contents, followed by a scaling inflection and shift to lower global compositions as shown in the inset, and (c) the interfacial excess decreases, indicating that temperature promotes a more random solute distribution.

Figure 2.6: Thermodynamic equilibrium states as a function of the bulk interaction energy for the state variables: T= 1000 °C, ω_{ig} = 0 eV, and $\gamma_A^o = \gamma_B^o$ = 0.48 J/m^2. With increasing bulk interaction energy, (a) the segregation energy increases and (b) the grain size trends shift to lower global solute contents, indicating that less solute is required to stabilize the nanostructure for large bulk interaction energies. (c) The interfacial excess is initially independent of composition at low ω_b, then scales with the global solute content as ω_b further deviates from ω_{ig}.

Figure 2.7: Thermodynamic equilibrium states as a function of the intergranular interaction energy for the state variables: T= 1000 °C, ω_b = 0.03 eV, and $\gamma_A^o = \gamma_B^o$ = 0.48 J/m^2. With increasing intergranular interaction energy, (a) the segregation energy decreases, (b) the grain size trends shift to higher global solute contents, and (c) the interfacial excess increases towards higher coverage levels, all of which support that higher solute contents are required to stabilize the nanostructure as ω_{ig} tends towards large, positive values.

Figure 2.8: Thermodynamic equilibrium states as a function of the solvent grain boundary energy for the state variables: T= 1000 °C, ω_b = 0.03 eV, and ω_{ig} = 0 eV . With increasing grain boundary energy, (a) the segregation energy generally decreases, although, depends to a large extent on the global solute content and relative magnitudes of the solute-solvent grain boundary energies, (b) the grain size trends shift to higher global solute contents, and (c) the interfacial excess increases towards higher coverage levels. These observations indicate that more solute is required to drive higher energy grain boundaries to equilibrium.

Figure 2.9: (a) Equilibrium grain size vs. global composition as a function of grain structure dimensionality. (b) Interfacial excess plotted for D = 1, 2, or 3 as a function of global solute content. The trends in (a) shift to higher global solute contents as D increases, attributed to the concurrent increase in grain boundary volume fraction. The interfacial excess in (b) is independent of dimensionality, and its functional dependence on X is imparted by the assigned state variables.

Figure 2.10: Grain size as a function of global composition for high and low heat of mixing systems. The low ΔH_{mix} trend is shifted to higher global solute contents, and exhibits a more moderate curvature as compared to the high heat of mixing system.

Figure 3.1: Schematic of the pulse cycling used in the deposition of Ni-W alloys, where the magnitude of the reverse pulse current density is varied to manipulate alloy composition, after Detor et al. [77].

Figure 3.2: X-ray diffraction spectra and corresponding grain sizes for the as-deposited nanocrystalline Ni-W alloys. All the specimens are single-phase FCC solid solutions, and the respective alloy compositions are indicated.

Figure 3.3: Bright field TEM images and selected area diffraction patterns for representative specimens. Panels (a)-(d) correspond to grain sizes of approximately 150, 40, 20, and 6 nm, respectively. In (d), a high resolution TEM image with lattice fringes is shown, and three discernible grains are circled for reference.

Figure 3.4: XRD spectra for three grain size specimens in the as-deposited state, and following a 300 °C anneal for 24 hours. While the as-deposited and annealed spectra are observed to be consistent for the finest nanocrystalline specimens, the d = 70 nm diffraction peaks are subtly sharper in the annealed condition, indicating grain growth.

Figure 4.1: Hardness as a function of grain size on double logarithmic scales. Classical Hall-Petch strengthening is observed with grain size refinement down to about ~20 nm, followed by an apparent breakdown regime.

Figure 4.2: SEM images of residual impressions on Ni-W alloy specimens with a grain size of (a) 20 nm, (b) 12 nm, (c) 6 nm, and (d) 3 nm. A cube corner indenter geometry was used in testing and all the images were taken at the same magnification. Note the shear offsets in the pile-up of the d = 3 nm sample shown in (d).

Figure 4.3: (a) Typical load-displacement responses for the finest grain size specimens resulting from indentation with a cube corner indenter at a strain rate of 0.15 s^{-1}. As identified by the series of arrows, discrete ripples or discontinuities are evident in the d = 3 nm data, while the d = 6 and 12 nm curves (offset for clarity by 50 and 100 nm on the depth axis, respectively) are smooth and continuous. (b) Strain rate plotted as a function of depth for the data shown in (a). Several prominent peaks occur in the d = 3 nm data that correlate exactly to the discontinuities identified in the load-displacement response from (a).

Figure 4.4: (a) Typical load-displacement curves for nanoindentation of a d = 20 nm grain size specimen at three strain rates. The curves shift to lower contact depths with increasing strain rate, corresponding to higher hardness values. (b) Hardness compiled as a function of strain rate for four representative grain size specimens; error bars are smaller than the data points in this figure.

Figure 4.5: Activation volume for deformation of nanocrystalline Ni-W alloys, along with literature data for Ni [10, 47, 54], Ni-Co [53], Cu [46, 48-51, 53], and Cu alloy [49] systems. The activation volume is normalized by the cubed Burger's vector, b^3, and the present data reveal an inflection near a grain size of 10-20 nm.

Figure 4.6: Hardness-cohesion ratio as a function of the Mohr-Coulomb coefficient for Berkovich and cube corner geometries, following Ref. [251]. The H/c ratios for the two geometries diverge as the pressure sensitivity increases (i.e. higher α), which results from the higher confining pressure imposed by the Berkovich tip relative to the cube corner.

Figure 4.7: SEM images of indentations made with (a) a Berkovich and (b) a cube corner indenter geometry on a Ni-W alloy of 20 nm grain size. (c) Representation of the two imprints from (a) and (b) showing that the cube corner indenter requires a larger projected area to support the same applied load (10 mN).

Figure 4.8: The Mohr-Coulomb friction coefficient, α, as a function of grain size. A maximum is observed for the present nanocrystalline Ni-W alloys at a grain size near 10-20 nm. Also shown are results from various literature data on Ni [57, 60] and Zn [58, 59], and Cu alloys [55, 56] which all lie to the right of the maximum, as well as simulation results on nanocrystalline Ni [63] that are exclusively to the left of the maximum. An approximate value of α typical of amorphous metals is also shown for reference at a grain size of 1 nm [65].

Figure 5.1: Representative raw data from an impact test on a 12 nm grain size Ni-W specimen, where the upper panels demonstrate the output displacement time data, from which the velocities, shown in the lower panels, are calculated. (a) Displacement and velocity over the full acquisition time, where the solid arrows denote initial acceleration of the tip, and the dotted arrows deceleration as the tip is driven into the specimen surface. The primary impact event circled in (a) is magnified in (b), where the critical displacements and corresponding velocities are highlighted. Note that the time scale has been arbitrarily assigned in (b).

Figure 5.2: Magnified view of the first two impact events from Figure 5.1(a). Calculating h_{res} and v_{out} rely on accurately identifying the point of deceleration (denoted with velocity v_{si}) associated with the tip coming back into contact with the sample surface after the initial rebound event.

Figure 5.3: Dynamic hardness as a function of grain size on double logarithmic scales. Hall-Petch scaling is observed down to a grain size of ~20 nm, followed by a breakdown manifested as a strengthening peak and region of "inverse Hall-Petch" weakening. The quasi-static hardness measurements from Section 4.2 are included for reference.

Figure 5.4: Hardness as a function of strain rate for specimens with grain sizes in the range $3 \leq d \leq 40$ nm. The dynamic measurements from the present work align well with the extrapolation from quasi-static nanoindentation results reproduced from Chapter 4. Corresponding SEM images of the residual impressions reveal discernible shear offsets around the impact sites for grain sizes as large as 12 nm. (Some of the impressions have a scar across them, made upon withdrawal of the tip; these scars are formed after the conclusion of the test and are not relevant to the discussion).

Figure 6.1: Hardness as a function of grain size on double logarithmic scales for as-deposited and relaxed Ni-W alloys at an indentation strain rate of 1.5×10^{-1} s^{-1}. The dashed trend lines are included for clarity, and shift to higher hardness values as the annealing temperature is increased, especially in the vicinity of the Hall-Petch breakdown.

Figure 6.2: Activation volume for the present Ni-W alloys in as-prepared and relaxed states, normalized by the cubed Burger's vector, b^3. Measurements of V from Chapter 4 are included for reference, as well as general trend lines. While the activation volumes for the relaxed specimens are in-line with the as-deposited values for grain sizes $\geq$12 nm, finer grain size specimens exhibit noticeable increases in V with increasing annealing temperature.

Figure 6.3: Scanning electron micrographs of the residual impressions on 3 nm grain size Ni-W specimens, in the (a) as-deposited condition, and annealed at (b) 150 °C and (c) 300 °C. An increase in the shear offset width is evident from (a)-(c), indicating that grain boundary relaxation promotes inhomogeneous flow at the finest nanocrystalline grain sizes.

Figure 6.4: Microhardness for the 3 nm grain size Ni-W specimen annealed to different extents. For a given annealing time of 24 hours, an increase in the annealing temperature leads to an increase in strength, attributed to grain boundary relaxation in Section 6.1, followed by a time-independent plateau; grain size also remains constant.

Figure 6.5: Yield stress as a function of temperature for three nanocrystalline grain size specimens, as calculated from the indentation hardness. A linear regression procedure is used to determine each of the slopes, which are included for reference.

Figure 6.6: Activation energy as a function of grain size determined from Eq. (6.4). Hall-Petch scaling and breakdown regimes, and the grain size associated with the minimum activation volume, are indicated. An inflection is observed in the activation energy, implying fundamental changes in the underlying deformation mechanisms.

Figure B.1: XRD spectra for specimens exposed to the isothermal heat treatments shown in Table B.1; annealing temperatures and resultant grain sizes are indicated. The diffraction peaks sharpen, and additional FCC reflections become evident, as the annealing temperature is increased.

Figure B.2: XRD spectrum for an as-deposited 6 nm grain size Ni-W specimen annealed at 700 ^{o}C for 24 hours. Primary FCC Ni reflections are observed, as are diffraction peaks corresponding to the Ni_4W intermetallic phase. The latter peaks are seen more clearly in the insets, which show a magnified view of the indicated regions. An additional tungsten oxide peak is evident, which is due solely to a small amount of remnant oxide remaining after a rough polishing step following the heat treatment.

Figure B.3: Hardness as a function of grain size for the isothermally annealed Ni-W alloys with a given W content of 21.3 at % at 1.5 x 10^{-1} s^{-1}; the hardness values for the 300 ^{o}C heat treated alloys is reproduced from Figure 6.1, and trend lines are included for reference. The 21.3 at % W alloys are substantially harder than the varying W content samples across the Hall-Petch breakdown regime.

Figure B.4: Activation volume as a function of grain size for the 21.3 at % W alloys, plotted along with varying W content measurements from Figure 6.2; trend lines are included for reference. While the measurements of V for the 21.3 at % W samples align with the varying W data at fine nanocrystalline grain sizes, a noticeable deviation is observed when the grain size exceed ~ 10 nm.

List of Tables

Table 2.1: Possible bulk, intergranular, and transitional bond configurations and their corresponding energies. Note that transitional bonds are assigned energies characteristic of the intergranular region.

Table 2.2: Bond configurations and existence probabilities, derived from the solute concentration in each of the respective regions, central to the free energy of mixing.

Table 3.1: Chemical composition of the ammoniacal citrate plating bath used in the synthesis of the present nanocrystalline Ni-W alloys, following Ref. [188].

Table 3.2: Deposition conditions for the specimens used in evaluating the mechanical properties at room temperature in Chapters 4 and 5. The table is organized according to descending grain size, as listed in the first column.

Table 3.3: Summary of the isothermal heat treatments used to study the effect of grain boundary state in Chapter 6. Heat treated grain sizes are included, and specimens used for elevated temperature indentation testing are indicated.

Table 6.1: Activation quantities for the three grain size specimens subjected to elevated temperature nanoindentation testing. The respective W contents and activation energy normalized by the shear modulus and cubed Burger's vector are also included.

Table B.1: Isothermal heat treatments used to vary the grain size for specimens with a given alloy composition of 21.3 at. %, and an as-deposited grain size of 6 nm, as indicated. Note that the heat treated grain sizes span the entire Hall-Petch breakdown.

Chapter 1: Introduction

1.1 Hall-Petch strengthening at the nanoscale: a shift to interface-dominated physics

The unique behavior of nanostructured metals has motivated extensive fundamental studies over recent years. Great emphasis has been placed on the scaling of mechanical properties with grain size reduction, and its connection to the underlying deformation mechanisms [1-6]. The most widely discussed scaling law is the classical Hall-Petch equation:

$$\sigma = \sigma_o + k_{HP} \times d^{-1/2} \tag{1.1}$$

which describes the increase in yield strength, σ, with the reciprocal square root of the grain size, d, and material-dependent constants, σ_o and k_{HP}. This relationship was empirically determined by Hall [7] and Petch [8], and implies that large increments in strength can be realized when the characteristic microstructural length scale approaches values of $d \leq 100$ nm (termed the nanocrystalline regime); experiments on a variety of materials have confirmed this implication [9-17]. An example in this regard is shown in Figure 1.1, which compiles strength scaling data for Ni from a number of studies. As grain size is refined to the nanoscale, the strength (or hardness) increases by almost an order of magnitude, in accordance with the Hall-Petch relation. However, the deformation physics responsible for the very high strengths in Fig. 1.1 remain an area of great controversy. Of course, grain boundaries act as obstacles that impede the motion of lattice dislocations, in turn, increasing the stress required to initiate slip. However, dislocations must gradually transition from collective to individual behavior as they become confined in extremely small nanometer-scale grains, which cannot support multiple dislocations.

The mechanistic nature of Hall-Petch strengthening, based on the dislocation-grain boundary interactions described above, has been proposed to change for grain sizes below ~500 nm, when

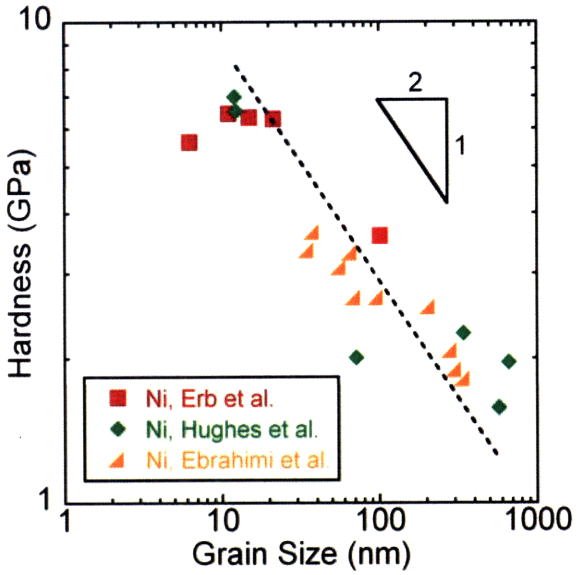

Figure 1.1: Strength scaling of nanocrystalline Ni from the studies of Erb et al. [18], Hughes et al. [13], and Ebrahimi et al. [11]. A breakdown in the classical Hall-Petch relationship is suggested at a grain size in the range of 10-20 nm.

conventional dislocation mechanisms become more confined [6, 19, 20]. Molecular dynamics simulations have demonstrated that dislocation activity gradually becomes dominated by grain boundary sources [6, 21-31], and although the nature of these mechanisms are not yet fully understood, system-dependent energy landscapes, referred to as generalized planar fault energy curves [32-36], are believed to dictate whether boundary-nucleated leading partials transect the entire grain, or are followed by trailing partials to form a full dislocation. While experimental confirmation of grain boundary-mediated dislocation plasticity has been more elusive, a number of transmission electron microscopy studies of deformed nanostructures [23, 33, 37-45] have detected enhanced dislocation activity in the vicinity of the grain boundaries in nanocrystalline specimens; such observations indeed suggest that dislocation activity is mediated by the grain boundaries at the nanoscale.

While the Hall-Petch relation and strength scaling in nanocrystalline solids has constituted a primary focus in the study of mechanical behavior at the nanoscale, the shift to interface-mediated plasticity influences the scaling of other mechanical properties as well, including the

rate and pressure dependence of strength [10, 46-60]. The rate sensitivity is commonly quantified through calculation of the activation volume for deformation, V [61, 62]:

$$V = 3\sqrt{3}kT\frac{\partial \ln \dot{\varepsilon}}{\partial H} \tag{1.2}$$

where $\dot{\varepsilon}$ is the strain rate, H is the hardness, k is the Boltzmann constant, and T is absolute temperature. According to Eq. (1.2), higher rate dependence is associated with lower activation volumes. Figure 1.2 compiles measurements of the activation volume from a variety of face-centered cubic (FCC) metals [10, 46-54], and clearly demonstrates an associated enhancement in the rate sensitivity (indicated by lower values of the activation volume) with decreasing grain size.

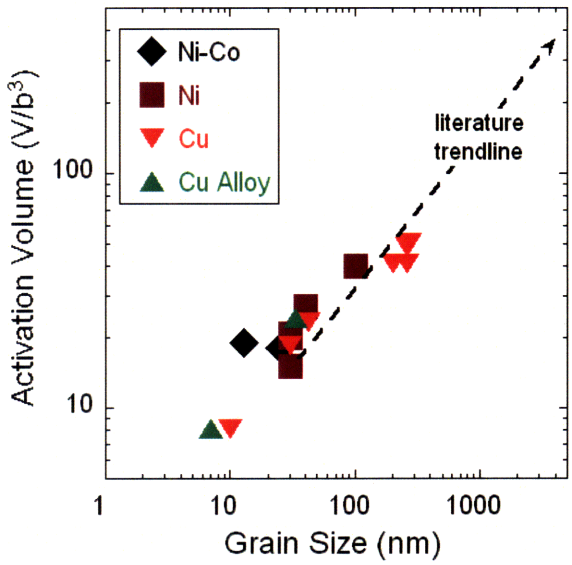

Figure 1.2: The activation volume for deformation in Ni [10, 47, 54], Ni-Co [53], Cu [46, 48-51, 53], and Cu alloy [49] systems as a function of grain size. Nanocrystalline metals exhibit drastically lower values of V when compared to their microcrystalline counterparts, corresponding to an enhancement in the rate sensitivity.

Another property believed to shift as the grain size is reduced to the nanoscale is the pressure dependence of deformation. This property is captured by normal stress-modified yield criteria,

such as the classical Mohr-Coulomb relation, which describes the effective yield strength under shear loading, τ, for a cohesive-frictional material:

$$\tau = \tau_o - \alpha\sigma_n \tag{1.3}$$

where τ_o is the cohesive strength and σ_n is the normal stress on the shear plane. The parameter α is a friction coefficient that quantifies the effect of normal stress, and can be regarded essentially as an index of pressure or normal-stress dependence. Measurements of the pressure sensitivity in the nanocrystalline regime are summarized in Figure 1.3 for a variety of materials systems [55-60]. While microcrystalline metals are known to generally be pressure-insensitive Von Mises solids, studies have shown that their nanocrystalline counterparts could in fact exhibit a pronounced pressure sensitivity, as indicated by the increase in α in Figure 1.3.

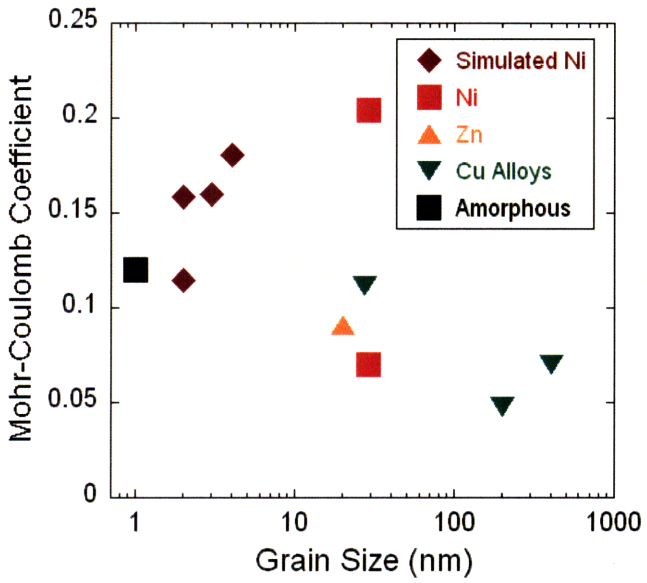

Figure 1.3: The Mohr-Coulomb coefficient as a function of grain size for pure Ni [57, 60] and Zn [58, 59], and Cu alloys [55, 56]. Finer nanocrystalline metals are more sensitive to pressure down to a grain size of about 20 nm, and an inflection is suggested when the simulation results from Lund et al. [63] are added. A typical value of $\alpha \sim 0.12$ for amorphous solids is included for reference [64, 65].

Based on the concept of grain boundary-mediated dislocation plasticity, analytical models have been proposed to interpret the intriguing scaling of the rate and pressure sensitivity in nanocrystalline FCC metals [30, 31, 61, 66-72]. In particular, the enhanced strain rate sensitivity and low experimental activation volumes can be attributed to nucleation of partial dislocations from a grain boundary facet [61]. A similar theoretical argument can also rationalize the elevated pressure sensitivity of deformation for ultrafine polycrystals. Cheng et al. [68] have argued that if plasticity is indeed controlled by grain boundary dislocation sources, then the uniaxial yield strength can be described in terms of the self-energy of a bowed dislocation pinned at a grain boundary. Because this energy is pressure-dependent [73], the yield strength becomes a function of pressure and thus exhibits a measurable tension-compression asymmetry [63, 68].

An interesting implication of the Hall-Petch relation and the idea of confined dislocation plasticity is that the strength should continue to increase with further refinement of the nanocrystalline grain size. However, early comparisons of the properties of polycrystals with amorphous solids, such as in the classic work of Nieh and Wadsworth [74], implied that an ultimate limit exists to the attainable strength, which is often far less than predicted by Eq. 1.1. As such, many researchers have asked the question: down to what grain size is the Hall-Petch relation valid? Referring back to the data compiled in Figure 1.1, scaling in accordance with the Hall Petch relation is demonstrated at large nanocrystalline grain sizes, but at d ~ 20 nm, a divergence from this scaling is suggested. This divergence is referred to as the Hall-Petch breakdown, and understanding its nature, and the underlying physics, represents a large subject of research over the past decade in the field of nanocrystalline metals.

1.2 The Hall-Petch breakdown

A breakdown in the Hall-Petch relation has been suggested in a number of material systems at grain sizes in the range of 10–30 nm [4, 74-83], and this deviation from classical strength scaling is believed to signal a transition in the underlying deformation mechanisms [66, 70, 84-91]. The Hall-Petch breakdown has been discussed at length as a continuous change in mechanisms as grain size is refined from the microcrystalline to nanocrystalline regime. The transition from unit dislocation plasticity to grain boundary-mediated sources of partials has been suggested to be accompanied by competing deformation mechanisms at the finest nanocrystalline grain sizes.

Molecular dynamic simulations have demonstrated that plasticity becomes confined to grain boundaries, locally in the form of atomic shuffling [88, 92], and globally through grain boundary sliding [26, 93-97]. Several micromechanical models have incorporated grain boundary sliding, accommodated by atomic shearing events [84, 86, 98-100], or dislocation plasticity [101, 102], to address the breakdown of the Hall-Petch relation.

An interesting aspect associated with the apparent onset of grain boundary sliding, such as that assumed in the aforementioned modeling efforts, is that it frequently occurs at grain sizes well below ~10 nm, where the structure becomes dominated by interfaces and the long-range atomic order characteristic of the intragranular regions disappears. Grain size-induced mechanistic shifts at the finest nanocrystalline grain sizes can thus be understood through comparison with the behavior of amorphous solids of similar composition. The heterogeneity of polycrystals tends to naturally distribute plasticity over many grains and/or grain boundaries, whereas there is no intrinsic microstructural barrier to severe plastic strain localization in amorphous metals [103]. Consequently, the plastic flow of metallic glasses is inhomogeneous, occurring through a series of shear banding events [104-111]. As the characteristic length scale of a crystalline microstructure approaches the amorphous limit, inhomogeneous flow can be expected to emerge, as suggested by Lund and Schuh [63] and further substantiated by the rotational diffusion model developed by Joshi and Ramesh [112-114], implying that many intriguing properties should be realized in fine nanocrystalline metals. For example, when the pressure sensitivity measurements in Figure 1.3 are supplemented by the simulation results of Lund and Schuh [63], an inflection in the pressure sensitivity is suggested, implying that the friction coefficient will converge upon the finite value representative of an amorphous solid [64, 65]. This viewpoint is analogous to the argument presented by Nieh and Wadsworth [74] addressed earlier, identifying a practical limit on the strength scaling of polycrystals. More recently, some authors have pursued this line of thinking quantitatively to model the yield behavior of nanocrystalline metals, where the nanostructure response is governed by a phase-mixture of the constitutive flow laws for the intragranular and intergranular regions [91, 115-125].

As implied in the above discussion, the scientific community has relied heavily on atomistic computer simulations as a central tool in studying mechanical behavior at the nanoscale [92,

126-131]. This technique is highly advantageous as it offers unprecedented control of the nanostructure, and the ability to directly observe the plastic deformation mechanisms. Many of the processing techniques employed to synthesize nanocrystalline metals do not provide such control over the nanostructure, leading to recurring inconsistencies and a lack of systematic experimental data. This is evident in the strength scaling data presented in Figure 1.1, and the rate and pressure sensitivity data shown in Figure 1.2 and Figure 1.3: no single set of experiments accesses the full range of grain sizes spanning the nanocrystalline regime, and the existing data are highly sporadic and incomplete. What is more, the strength scaling behavior of nanocrystals determined through atomistic simulations often conflict with experimental results; while molecular dynamics (MD) simulations illustrate that the Hall-Petch breakdown manifests as a "strongest grain size" and weakening regime, sometimes referred to as "inverse Hall-Petch" scaling [81, 90], experimental studies on as-prepared samples more frequently demonstrate a grain size-independent strength plateau [4, 77]. Of course, it is widely appreciated that direct comparison of such results is not possible, as simulations are restricted to extremely high strain rates on the order of 10^8 s^{-1}, whereas experiments are typically performed at quasi-static strain rates. These conflicting simulation and experimental results, combined with the scarcity of systematic experimental data, have generated considerable debate as to nature of the Hall-Petch breakdown [66, 78, 80, 89, 132].

The lack of experimental mechanical data across the breakdown regime has motivated some researchers to pursue post-processing means to try to obtain more systematic variations in nanocrystalline grain size, such as isothermal heat treatments to grow the grains. To some extent, this has led to even further ambiguity as to the nature of the Hall-Petch breakdown. Such annealed samples frequently suggest the presence of a strengthening peak and "inverse" weakening regime [15, 133-136], similar to behavior determined from molecular dynamics simulations. However, some of these results have been criticized, as the samples were prepared using powder metallurgy techniques, and can therefore suffer from a large number of processing defects, including most notably residual porosity. A final caveat arises when as-processed samples are exposed to low homologous temperature anneals ($T < 0.25 \cdot T_m$), well below the onset temperature for grain growth, ordering, or intermetallic precipitation. The strength (or hardness) measured at a given grain size is markedly greater in the annealed state as compared to that

determined in the as-prepared condition [15, 133, 136, 137]. This effect has been attributed in literature to a change in the grain boundary state, i.e., grain boundary relaxation, and is demonstrated by a variety of pure nanocrystalline metals [40, 138-142] and alloys [133, 143, 144]. Because driven processes are commonly employed to produce these materials, the grain boundaries often consist of a large number of excess dislocations [145-148], and can be considered far-from-equilibrium. The thermal energy introduced upon annealing is sufficient to overcome the kinetic barrier for annihilation of these dislocations, thereby increasing the order in the grain boundary and removing potential sources for grain boundary-mediated dislocation activity. This is believed to increase the resistance to deformation, and manifests as an apparent increase in strength [134, 149]. Nevertheless, strength scaling in annealed samples remains a signification point of confusion in the literature.

In light of the above discussion, the strength scaling behavior and shift to grain boundary-dominated physics at the nanoscale can be summarized in the schematic presented in Figure 1.4, after Cheng et al. [150] and Lund et al. [63]. Traditional dislocation interactions, responsible for classical Hall-Petch strengthening, transitions to grain boundary sources of unit and partial dislocations below ~200 nm, which is believed to induce a shift in the Hall-Petch slope. Further reduction in grain size beyond ~10 nm leads to the onset of grain boundary-confined plasticity, and the deformation behavior should ultimately converge to inhomogeneous, glass-like plasticity, similar to that exhibited by metallic glasses as noted by Lund and Schuh [63]. While many experimental studies have sought to validate the mechanistic shift so often observed in atomistic simulations and assumed in analytical models, robust experimental data remain relatively sparse. This lack of consistent, systematic data can be largely attributed to the difficulty in processing homogeneous nanocrystalline specimens of high quality, which has made bridging the deformation behavior of nanocrystalline and amorphous metals, across the entire Hall-Petch breakdown regime, a formidable task.

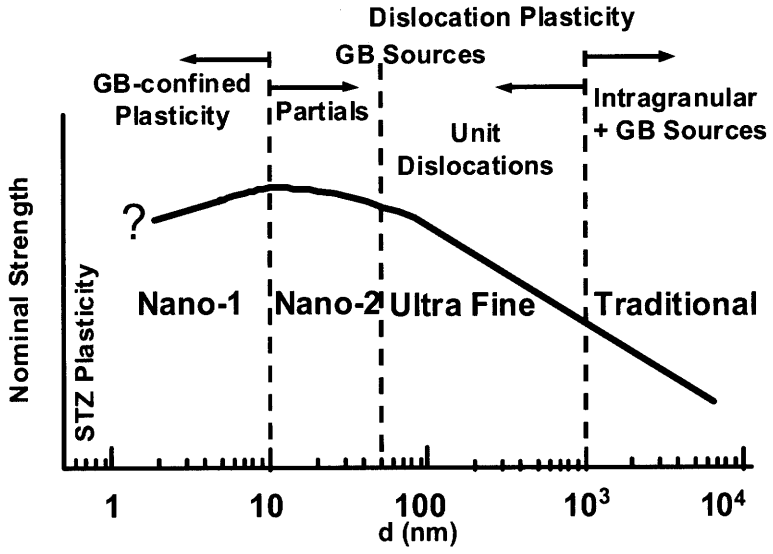

Figure 1.4: Deformation mechanism map for nanocrystalline metals after Cheng et al. and Lund et al. At large grain sizes, classical dislocation plasticity is expected , which transitions to grain boundary sources of unit and partial dislocations, and ultimately plasticity is confined to the grain boundary regions, e.g. grain boundary sliding. Lund and Schuh [63] have predicted a transition to shear localization at the finest nanocrystalline grain sizes.

1.3 Processing and nanostructure stability

Processing of pure nanocrystalline metals has proven a challenging undertaking, and there are currently a number of routes available [2, 4, 5, 18, 151], with severe plastic deformation [152, 153], inert gas condensation [79, 154, 155], and electrodeposition [9, 16, 156-158] comprising some of the more common techniques. Whereas severe plastic deformation is limited by the minimum achievable grain size (~50 nm) and inert gas condensation by the difficulty in obtaining dense specimens, electrodeposition has proven to be a successful technique for producing single-component, fully-dense metal deposits; this has been demonstrated for materials such as Cu [156], Ni [157-163], Al, [164, 165], and Pd [166, 167], with grain sizes approaching ~20 nm. While the high deposit quality of pure electrodeposited metals is suitable for mechanical testing, the far-from-equilibrium state occupied by these materials render them unstable with respect to thermally-activated structural changes [168-170]. Such instabilities can

be understood in the thermodynamic context formalized by Gibbs. The change in the Gibbs free energy, G, with respect to the interfacial area, A, is proportional to the grain boundary energy, γ:

$$dG \propto \gamma dA \tag{1.4}$$

An elemental metal has a positive grain boundary energy, so a reduction in the interfacial area (i.e., an increase in grain size) will always lower the Gibbs free energy.

Alloying has the potential to suppress the instability of pure nanocrystalline metals, as evidenced by the enhanced thermal stability of a number of binary nanocrystalline alloys relative to their single component counterparts [133, 159, 171-173]. While such behavior has been traditionally linked to kinetic phenomena such as solute drag [174], recent studies have suggested that nanocrystalline alloys could in fact be thermodynamically stabilized by solute enrichment at the grain boundaries [175-177]. The idea of segregation-induced thermodynamic stability in nanocrystalline solids was first addressed analytically by Weissmüller [177-179], who considered the change in the Gibbs free energy of a polycrystal upon alloying. Under certain simplifying assumptions, a minimum free energy is predicted at a specific solute content for a given grain size, as schematically shown in Figure 1.5 [177]. Finer grains are characterized with grain boundaries lacking solute (i.e. under-full), coarser with supersaturated grain boundaries (i.e. over-full), and either scenario leads to an increase in the system free energy. As such, the critical segregant level can be physically interpreted as the amount required to fill the available grain boundary sites without supersaturating the interface.

By solving the Gibbs adsorption equation in the dilute limit assuming McLean-type segregation [180], the grain boundary energy takes the following form [177]:

$$\gamma = \gamma_o - \Gamma\big|_{X\to 0, f_{ig}\to 0}\left(H_{seg} + kT\ln X\right) \tag{1.5}$$

where γ_o is the grain boundary energy of the pure solvent, $\Gamma\big|_{X\to 0, f_{ig}\to 0}$ is the solute excess in the

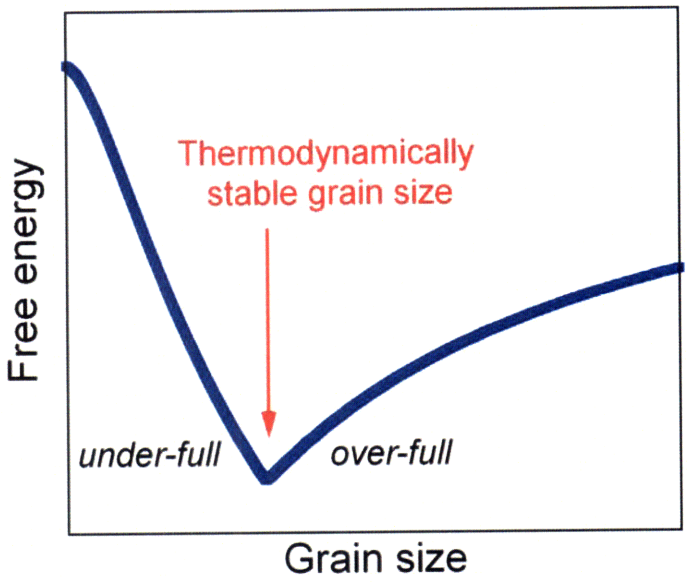

Figure 1.5: Gibbs free energy as function of nanoscale grain size for a given solute content, after Weissmuller [177]. A minimum is predicted in the free energy, corresponding to the thermodynamically stable grain size; image courtesy of Dr. A.J. Detor.

grain boundary (the subscript denotes the limiting assumptions, where X is the global solute content and f_{ig} is the interfacial volume fraction), and H_{seg} is the segregation energy, i.e. the difference in energy of a solute atom occupying a grain boundary site vs. a grain interior site. From Eq. (1.5), it is evident that the grain boundary energy can be reduced by enhancing the solute excess, and if the magnitude of this reduction is sufficient to drive γ to zero, the grain boundaries can apparently exist in equilibrium. A particularly clear illustration of the principle behind Eq. (1.5) is provided by the molecular dynamics simulations of Millet et al. [181], which explicitly show that for artificial states of segregation in Lennard-Jones polycrystals, the grain boundary energy can indeed reach zero.

Extremely fine nanocrystalline grain sizes have been realized in a variety of binary alloy systems, for example Y-Fe [182], Ni-P [183], Pd-Zr [176, 184], and Fe-Zr [185]. Because the elements composing these alloys are highly immiscible with a large positive heat of mixing, these systems are classified as strongly segregating, with high assumed values of H_{seg} ($\geq$ 0.5 eV) that can substantially reduce the grain boundary energy via Eq. (1.5). In all the alloy systems

identified above, higher alloy compositions have been experimentally correlated with finer grain sizes (i.e. a higher volume fraction of grain boundaries), as demonstrated specifically for Ni-P in Figure 1.6, suggesting grain boundary segregation as the essential driving force for nanostructure stabilization. Alloys exhibiting some solid solubility and a weaker apparent segregation tendency have also been synthesized with nanocrystalline grain sizes; examples in this regard are Ni-W [77, 186-188] and Ni-Fe [173, 189]. For some of the binary alloy systems described above, solute enrichment at grain boundaries has indeed been confirmed by atom probe tomography [190, 191], and studied extensively by computer simulations both for individual grain boundaries [192] and, more recently, for simulated nanocrystalline structures [181, 193, 194]. The Ni-W system, in particular, has been found to display a low segregation energy (~0.1 eV) in the dilute limit, and reduces further with increasing solute (W) addition [194]; still, any grain size in the nanocrystalline range can be produced by controlling the solute content [77, 186-188], as evidenced in Figure 1.6. However, a large discrepancy is observed in the range of grain sizes accessible in each system, where Ni-P is limited to a much smaller range.

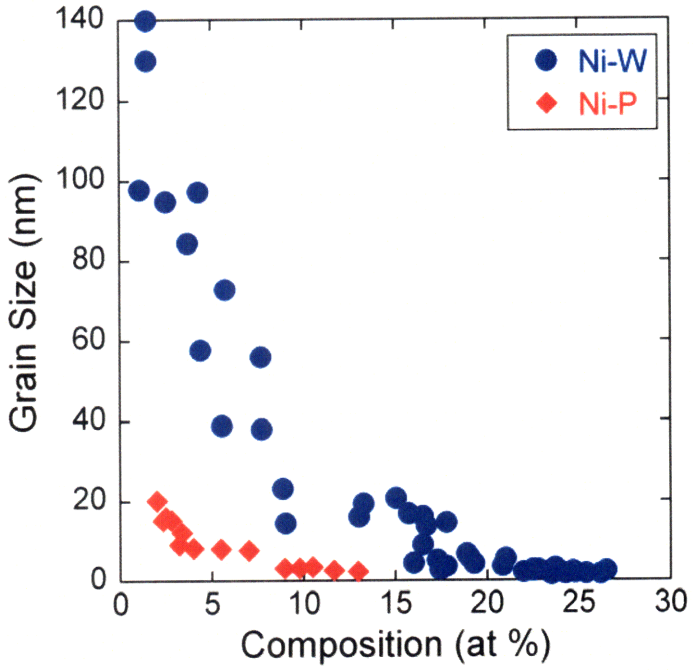

Figure 1.6: Scaling of nanocrystalline grain size with alloy composition for the strongly-segregating Ni-P system, and the weakly-segregating Ni-W system, taken from the works of Liu et al. [183] and Detor et al. [77], respectively. A higher alloy composition promotes finer grain sizes, regardless of the segregation tendency.

Analytical models have been developed to rationalize grain size-composition trends in strongly segregating systems, such as Ni-P, based on the fundamental principles of grain boundary segregation. Many studies have sought to extend the early work of Weissmüller [177] to understand the nature of grain boundary energy reduction and solute distributions in terms of the unique thermodynamic properties of binary nanocrystalline systems [175, 183, 195-197]. However, the key assumptions used in most of these models are quite severe, generally limiting the discussion to dilute solutions with extremely high segregation tendencies. This is unfortunate because most of the experimental nanocrystalline alloys described earlier are non-dilute, and not all of them exhibit a strong tendency for segregation (e.g. Ni-W). Recently, Beke et al. [198, 199] relaxed some of these assumptions in a statistical model, and considered segregation to free surfaces on one-dimensional nanocrystals. The statistical nature of this model is attractive in principle, providing a concrete framework to evaluate the conditions for equilibrium directly from a free energy function. Although, being derived for segregation to a free surface with no unique interfacial energies, this model lacks some of the thermodynamic parameters associated with grain boundary properties that are essential in differentiating various nanocrystalline alloys.

Despite the progress cited above, there is as yet no simple analytical model for grain boundary segregation-based nanostructure stabilization that extends to general (non-dilute) alloys, and incorporates energetic interactions that derive from the characteristic thermodynamic quantities governing the mixing behavior of binary systems. Consequently, the central thermodynamic variables dictating whether an alloy system has the potential to access the full nanocrystalline regime (e.g. Ni-W), or will be constrained to a small range of achievable grain sizes (e.g Ni-P), are not well understood, which has severely limited the design of stable nanostructures.

1.4 Problem statement

While atomistic simulations and complementary analytical models have provided useful insight into the deformation behavior of nanocrystalline metals, experimental validation of these results across the full Hall-Petch breakdown regime has proven a challenging task, and continues to plague mechanical behavior studies at the nanoscale. This lack of systematic experimental data is generally attributed to the difficultly in processing high-quality nanocrystalline specimens suitable for mechanical testing. Although alloying has been suggested as a viable route to stable

nanocrystalline metals, the tailorability of the nanostructure depends to a great extent on the chosen material system. Existing analytical models used to predict nanostructure stability are often limited by a number of severe assumptions, rendering them inapplicable to general alloy systems.

The deficiencies described above present a number of areas for fundamental scientific research in nanostructured materials, and the central aim of the present work is to (i) study alloying-induced nanostructure stabilization and its implications for the design of stable nanocrystalline alloys, and (ii) learning from this modeling, exploit a tailorable alloy system to first synthesize specimens with grain sizes ranging from just a few to hundreds of nanometers, and then explore the mechanical behavior across the entire Hall-Petch breakdown regime.

The present work is divided into five sections, according to the following outline:

- Based on the principles of statistical thermodynamics, an analytical model is developed in Chapter 2 to describe thermodynamic stabilization of binary nanocrystalline alloys, and provide improved guidelines for the design of stable nanostructures.
- With an understanding of how to access grain sizes across the entire Hall-Petch breakdown regime, nanocrystalline Ni-W alloys are synthesized with grain sizes from 3-150 nm, and the relevant processing methodologies and specimen characterization results are presented in Chapter 3.
- The as-deposited nanocrystalline Ni-W alloys are subjected to ambient temperature nanoindentation testing to examine strength, as well as the rate and pressure dependence of strength in Chapter 4, with an emphasis on the nanocrystalline-amorphous transition.
- In Chapter 5, dynamic indentation experiments are performed on the as-deposited Ni-W specimens, with an indentation strain rate of $\sim 10^3$ s^{-1}. The results are discussed in comparison with the quasi-static results to address the elusive nature of the Hall-Petch breakdown.
- The influence of grain boundary state on the mechanical behavior is studied in Chapter 6 on heat treated Ni-W specimens, followed by elevated temperature nanoindentation tests to explore signatures of thermally-activated plasticity.

Chapter 2: Analytical modeling of thermodynamically stable nanocrystalline alloys

The analytical models developed by Weissmüller [177] and Kirchheim [175, 183] discussed in Chapter 1 are limited to dilute solutions with extremely high segregation tendencies, and the statistical model derived by Beke [198, 199] is generally for free surface segregation. Although instructive, such severe assumptions hinder their applicability to general binary alloy systems. In this chapter, we formulate a generalized analytical thermodynamic model, without restricting ourselves to the dilute limit or to strongly segregating solute species. The derivation is presented for grain geometries of arbitrary dimensionality, and for arbitrary pair-wise interactions among segregated solute atoms, which alleviates the need to assume saturated grain boundaries. The result is a simple model that permits comparative analysis of various binary alloys, and provides improved guidelines for design of nanocrystalline materials.

2.1 Analytical framework

The statistical framework required to analyze grain boundary segregation in binary alloy systems is developed in this section. We begin by presenting a modified form of the regular solution model that captures the additional energetic penalty associated with introducing internal interfaces (i.e. grain boundaries) of a finite volume fraction into a single-phase crystalline solution. The possibility of any additional competing secondary or intermetallic phases is explicitly neglected, as are contributions from any additional thermodynamic potentials. The enthalpy of mixing is formulated by incorporating the distribution of bonds in the grains and intergranular regions into a modified solution model, and combined with entropic contributions to establish the free energy of mixing. A series of equilibrium equations are finally derived from the free energy function, which can be used to investigate thermodynamically stable grain sizes.

2.1.1 Solution model

To describe a binary mixture of solvent "A" and solute "B" atoms, we consider a statistical framework that employs pairwise interaction energies in a manner analogous to that which yields the regular solution model. However, we divide the full volume of the system into two separate

regions— that belonging to the grains, and that belonging to intergranular regions. The latter region shall represent energetic contributions from all intergranular structural elements, including grain boundaries, triple junctions, and quadruple nodes, which are averaged together in this construction. The atomic interactions are uniquely defined in the bulk and intergranular regions, as illustrated in Table 2.1.

Table 2.1: Possible bulk, intergranular, and transitional bond configurations and their corresponding energies. Note that transitional bonds are assigned energies characteristic of the intergranular region.

Bond Region	Bonds	Energies
Bulk	N_b^{AA}	E_b^{AA}
	N_b^{BB}	E_b^{BB}
	N_b^{AB}	E_b^{AB}
Intergranular	N_{ig}^{AA}	E_{ig}^{AA}
	N_{ig}^{BB}	E_{ig}^{BB}
	N_{ig}^{AB}	E_{ig}^{AB}
Transitional	N_t^{AA}	E_{ig}^{AA}
	N_t^{BB}	E_{ig}^{BB}
	N_t^{AB}	E_{ig}^{AB}

It also becomes necessary to introduce additional bonding pairs to capture bonds that bridge between the two distinct regions, as depicted in Figure 2.1; we define these "transitional" bonds to have pairwise energies characteristic of the intergranular region (cf. Table 2.1). The solution energy can be written as a sum over the individual bond energies, E, of all the possible atomic pairs, N, in each bonding region, r:

$$U_{\text{soln}} = \sum_r \left\{ N_r^{AA} E_r^{AA} + N_r^{BB} E_r^{BB} + N_r^{AB} E_r^{AB} \right\} \tag{2.1}$$

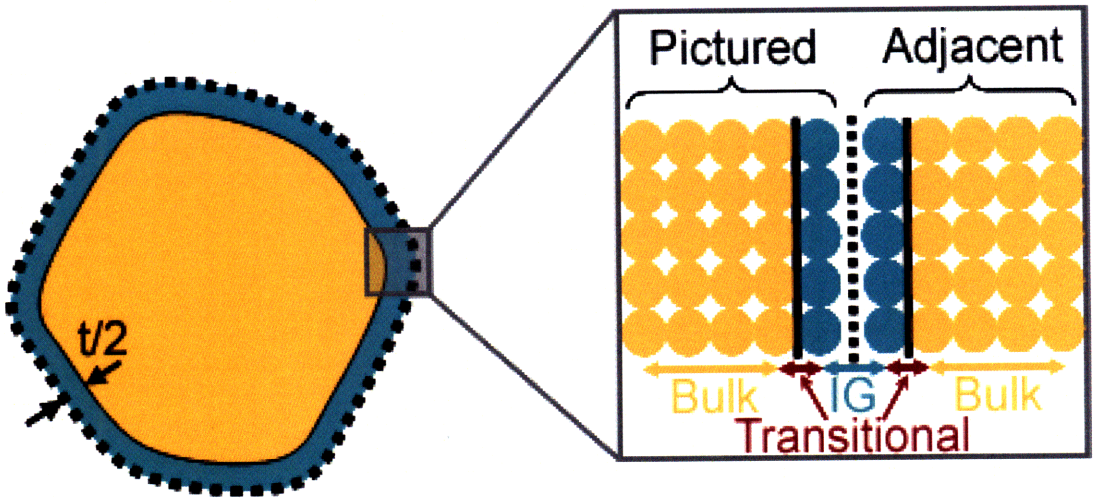

Figure 2.1: Schematic of an arbitrary grain shape, with the atomic configuration at the interface between the pictured and adjacent grain highlighted. The two planes of atoms at the boundary between the grains, indicated by the dotted line, are denoted the intergranular region. Intergranular bonds are those located entirely within the intergranular region, and transitional bonds connect these atoms to those in the bulk region.

where the superscripts denote the atom types involved, and the subscript 'r' distinguishes bulk (b), intergranular (ig), and transitional (t) bonds; all the possible bonding configurations are shown in Table 2.1. Within this framework, the energy of mixing, ΔU_{mix}, not only accounts for chemical interactions in the solid solution, but also incorporates the interfacial energy characteristic of the intergranular region:

$$\Delta U_{mix} = U_{\text{soln}} - U_{ref} \tag{2.2}$$

where U_{ref} represents the energy of an unmixed, interface-free state:

$$U_{ref} = \left(\frac{zN^{A}}{2}\right)E_{b}^{AA} + \left(\frac{zN^{B}}{2}\right)E_{b}^{BB} \tag{2.3}$$

The coordination number is denoted by z, and N^A and N^B are the total numbers of A and B atoms in solution, respectively.

For a system with a given global composition, the total number of each atom type is related to the number of bonds via:

$$zN^A = 2N_b^{AA} + 2N_t^{AA} + 2N_{ig}^{AA} + N_b^{AB} + N_t^{AB} + N_{ig}^{AB} \tag{2.4a}$$

$$zN^B = 2N_b^{BB} + 2N_t^{BB} + 2N_{ig}^{BB} + N_b^{AB} + N_t^{AB} + N_{ig}^{AB} \tag{2.4b}$$

where the factors of two account for each like bond connecting two like atoms. We can express Eqs. (2.4a) and (2.4b) in terms of the numbers of like bonds in the bulk, and substitute these relations into Eqs. (2.1) and (2.3) to obtain the change in the internal energy upon mixing:

$$\begin{aligned}\Delta U_{mix} = N_b^{AB}\left(E_b^{AB} - \frac{E_b^{AA} + E_b^{AA}}{2}\right) + \left(N_t^{AA} + N_{ig}^{AA}\right)\left(E_{ig}^{AA} - E_b^{AA}\right) + \ldots \\ \ldots + \left(N_t^{BB} + N_{ig}^{BB}\right)\left(E_{ig}^{BB} - E_b^{BB}\right) + \left(N_t^{AB} + N_{ig}^{AB}\right)\left(E_{ig}^{AB} - \frac{E_b^{AA} + E_b^{BB}}{2}\right)\end{aligned} \tag{2.5}$$

where terms involving the like bonding pairs in the bulk have cancelled with the equivalent terms contributed by the reference state. We now examine the geometric constraints imposed by a grain structure and the pairwise probabilities for forming the various bond types to determine explicit expressions for the seven remaining values of N in Eq. (2.5).

2.1.2 Bond distribution

The number of bonds of each type present in each of the three bonding regions can be resolved by considering the total number of bonds inherent to each region, and the probability that each of these bonds is of a given type. To address the bonding distribution, we consider the volumetric density of atoms in each region, normalized by the total number of atoms in the system. Given an arbitrary grain geometry, the intergranular region is assigned as a shell of finite thickness, t/2, with a geometrically similar shape to the grain; this is illustrated in Figure 2.1 for a two-dimensional grain of irregular shape.

Normalizing the volumetric atomic density by the total number of atoms eliminates the numerical shape factor associated with any specific grain geometry, and the intergranular volume fraction, f_{ig}, can be expressed as:

$$f_{ig} = 1 - \left(\frac{d-t}{d} \right)^{D} \tag{2.6}$$

where d is the grain size, and D is the dimensionality of the grain structure. D = 3 should be used for a general three-dimensional polycrystal, while D = 2 is useful for columnar or highly-elongated grain structures and D = 1 applies to lamellar or plate-like grains. We can also uniquely define the solute content in the bulk, X_b, and intergranular, X_{ig}, regions, which are related to the global solute content, X, by a volume fraction-weighted average:

$$X = \left(1 - f_{ig}\right) X_b + f_{ig} X_{ig} \tag{2.7}$$

The probability of each possible bond configuration can be enumerated by assuming random site occupation based on the defined compositions in each of the regions, as listed in Table 2.2.

The total number of bonding pairs present in the bulk (P_b), intergranular (P_{ig}), and transitional regions (P_t) are functions of f_{ig} and the total number of atoms, N_o:

$$P_b = \frac{z}{2}\left(1 - f_{ig}\right) N_o \tag{2.8a}$$

$$P_{ig} = \left(\frac{z}{2} f_{ig} - z\upsilon f_{ig} \right) N_o \tag{2.8b}$$

$$P_t = z\upsilon f_{ig} N_o \tag{2.8c}$$

According to Eq. (2.8a), the number of bulk bonds is simply equal to the total number of bonds in the system, $zN_o/2$, weighted by the bulk volume fraction.

Table 2.2: Bond configurations and existence probabilities, derived from the solute concentration in each of the respective regions, central to the free energy of mixing.

Bond Region	Bonds	Energy	Probability	Bonds/ Region
Bulk	N_b^{AB}	E_b^{AB}	$2X_b(1-X_b)$	P_b
Intergranular	N_{ig}^{AA}	E_{ig}^{AA}	$(1-X_{ig})^2$	P_{ig}
	N_{ig}^{BB}	E_{ig}^{BB}	X_{ig}^2	
	N_{ig}^{AB}	E_{ig}^{AB}	$2X_{ig}(1-X_{ig})$	
Transitional	N_t^{AA}	E_{ig}^{AA}	$(1-X_b)(1-X_{ig})$	P_t
	N_t^{BB}	E_{ig}^{BB}	X_bX_{ig}	
	N_t^{AB}	E_{ig}^{AB}	$X_{ig}(1-X_b)+ X_b(1-X_{ig})$	

The leading term in Eq. (2.8b) has the same form, weighting the total number of system bonds by the grain boundary volume fraction; the second term subtracts off the number of transitional bonds, which are counted separately in Eq. (2.8c). The factor, υ, termed the transitional bond fraction, represents the effective coordination for atoms contributing bonds to the transitional bonding region, and will be defined for all subsequent numerical calculations as 1/2. This essentially assigns half the atomic bonds at the bulk-intergranular interface as transitional bonds, with type probabilities deriving from both the bulk and intergranular solute fractions. When the occupation probabilities shown in Table 2.2 are scaled by the respective number of regional bonds, expressions for the seven bonding pairs central to the change in internal energy upon mixing are obtained.

2.1.3 Free energy function

The free energy of mixing, ΔG_{mix}, is a combination of enthalpic and entropic contributions expressed as:

$$\Delta G_{mix} = \Delta H_{mix} - T\Delta S_{mix} \tag{2.9}$$

where ΔH_{mix} and ΔS_{mix} represent the system enthalpy and entropy of mixing, respectively. As is customary for condensed phases, we neglect the change in volume upon mixing, and the enthalpy of mixing is thus represented by the change in internal energy given by Eq. (2.5), i.e., $\Delta H_{mix} = \Delta U_{mix}$. The entropy of mixing is derived by considering the distribution of atoms over distinct atomic sites randomly throughout the system, and simplifies to a volume fraction-weighted average of the random mixing entropy for the bulk and intergranular regions:

$$\Delta S_{mix} = -kN_o \begin{Bmatrix} \left(1-f_{ig}\right)\left[X_b \ln X_b + \left(1-X_b\right)\ln\left(1-X_b\right)\right] + \ldots \\ \ldots + f_{ig}\left[X_{ig} \ln X_{ig} + \left(1-X_{ig}\right)\ln\left(1-X_{ig}\right)\right] \end{Bmatrix} \tag{2.10}$$

where k is Boltzmann's constant.

Because the enthalpy and entropy of mixing both scale with system size, N_o, the free energy can be expressed on a per atom basis by normalizing with respect to N_o. Introducing Eq. (2.10) and Eq. (2.5) into Eq. (2.9) yields the complete form of the free energy of mixing for our system. However, before introducing its full functional form, it is useful to examine the physical limits on grain size, which is bounded by $0 \le f_{ig} \le 1$, corresponding to $t \le d \le \infty$. For $d \to \infty$, the free energy of mixing takes the form:

$$\Delta G_{mix}\big|_{d\to\infty} = zX\left(1-X\right)\left(E_b^{AB} - \frac{E_b^{AB}+E_b^{AB}}{2}\right) + kT\left[X\ln X + \left(1-X\right)\ln\left(1-X\right)\right] \tag{2.11}$$

where X_b and X are equivalent via Eq. (2.7). As expected, in the infinite grain size limit the free energy of mixing converges to a regular solution model for the bulk phase, and the combination of bond energies in Eq. (2.11) is accordingly recognized as the regular solution interaction energy:

$$\omega_b = \left(E_b^{AB} - \frac{E_b^{AA}+E_b^{BB}}{2}\right) \tag{2.12}$$

Eq. (2.12) has important implications for bond preference in the bulk, where $\omega_b = 0$ is characteristic of an ideal solution, $\omega_b > 0$ prefers like bonds, and $\omega_b < 0$ unlike bonds.

In the other limit, $d \to t$ represents the reduction of grain size to the "amorphous limit", where only the intergranular region exists, with a corresponding free energy:

$$\begin{aligned}\Delta G_{mix}\big|_{d\to t} &= \frac{z}{2}(1-X)\left(E_{ig}^{AA} - E_b^{AA}\right) + \frac{z}{2}X\left(E_{ig}^{BB} - E_b^{BB}\right) + \ldots \\ \ldots &+ zX(1-X)\left(E_{ig}^{AB} - \frac{E_{ig}^{AA} + E_{ig}^{BB}}{2}\right) + kT\left[X\ln X + (1-X)\ln(1-X)\right]\end{aligned} \tag{2.13}$$

and X_{ig} is now equivalent to X. This expression may essentially be regarded as a regular solution model for the "amorphous" intergranular phase, and contains a characteristic regular solution parameter analogous to Eq. (2.12):

$$\omega_{ig} = \left(E_{ig}^{AB} - \frac{E_{ig}^{AA} + E_{ig}^{BB}}{2}\right) \tag{2.14}$$

In addition, the differences in like bond energies between the grain and intergranular sites are incorporated by the first two terms in Eq. (2.13), and are proportional to the grain boundary energies of the pure solvent, γ_A, and solute, γ_B, phases:

$$\gamma_A \propto \frac{z}{2}\left(E_{ig}^{AA} - E_b^{AA}\right) \tag{2.15a}$$

$$\gamma_B \propto \frac{z}{2}\left(E_{ig}^{BB} - E_b^{BB}\right) \tag{2.15b}$$

Introducing these relations into Eq. (2.13), the resultant free energy in the amorphous limit is written more succinctly as:

$$\Delta G_{mix}\big|_{d\to t} = \frac{\Omega}{t}(1-X)\gamma_A + \frac{\Omega}{t}X\gamma_B + zX(1-X)\omega_{ig} + kT\left[X\ln X + (1-X)\ln(1-X)\right] \quad (2.16)$$

where the solvent atomic volume, Ω, normalized by the intergranular shell thickness is taken for the proportionality constant in Eqs. (2.15). Interestingly, Eq. (2.16) suggests that the free energy of a binary amorphous phase involves both the chemical mixing preference and a weighted average of the grain boundary energies of the pure components.

Making use of some the above definitions, but without carrying any simplifying assumptions, the full mixing free energy function is written:

$$\begin{aligned}\Delta G_{mix} = {} & z(1-f_{ig})X_b(1-X_b)\omega_b + \frac{\Omega}{t}f_{ig}(1-X_{ig})\gamma_A + \frac{\Omega}{t}f_{ig}X_{ig}\gamma_B + zf_{ig}X_{ig}(1-X_{ig})\omega_{ig} + \ldots \\ & \ldots + z\upsilon f_{ig}\left\{\left[X_{ig}(X_{ig}-X_b) - (1-X_{ig})(X_{ig}-X_b)\right]\omega_{ig} - \frac{\Omega}{zt}(X_{ig}-X_b)(\gamma_B-\gamma_A)\right\} + \ldots \\ & \ldots + kT\left\{(1-f_{ig})\left[X_b\ln X_b + (1-X_b)\ln(1-X_b)\right] + f_{ig}\left[X_{ig}\ln X_{ig} + (1-X_{ig})\ln(1-X_{ig})\right]\right\}\end{aligned} \quad (2.17)$$

The leading three terms represent the enthalpic contribution from the two distinct bulk and intergranular regions, while the fourth term captures the transitional bond enthalpy. The last term is the mixing entropy directly from Eq. (2.10). Thus, the free energy function now explicitly accounts for energetics unique to both the grains and grain boundaries in a binary alloy system.

2.1.4 Equilibrium equations

To derive the necessary equilibrium conditions, we simultaneously minimize ΔG_{mix} with respect to the intergranular composition and grain size for a closed system (i.e. constant X):

$$\left.\frac{\partial \Delta G_{mix}}{\partial X_{ig}}\right|_X \to 0 \quad (2.18a)$$

$$\left.\frac{\partial \Delta G_{mix}}{\partial f_{ig}}\right|_X \to 0 \quad (2.18b)$$

If we apply only the condition of Eq. (2.18a), an expression for the characteristic segregation isotherm is obtained, which describes the solute distribution for a given grain size, and exhibits an analogous form to the classical McLean equation [180]:

$$\frac{X_{ig}}{1-X_{ig}} = \frac{X_b}{1-X_b} \cdot \exp\left[\frac{\Delta H_{seg}}{kT}\right] \tag{2.19}$$

but with a modified segregation energy, ΔH_{seg}, expressed as:

$$\begin{aligned} \Delta H_{seg} = z\left[\omega_b - \omega_{ig}\left(1-\frac{\upsilon}{1-f_{ig}}\right) - \frac{\Omega}{zt}\left(\gamma_B - \gamma_A\right)\left(1-\frac{\upsilon}{1-f_{ig}}\right)\right] + \ldots \\ \ldots + 2zX_{ig}\omega_{ig}\left(1-\frac{\upsilon}{1-f_{ig}}\right) - 2z\left[X_b\omega_b + \upsilon\left(X_{ig}-X_b\right)\omega_{ig}\right] \end{aligned} \tag{2.20}$$

The leading bracketed term in Eq. (2.20) is a combination of bond energies that describes McLean-type segregation for a free surface, with no segregated solute-solute interactions. The additional terms account for such interactions, which in the present model are functions of υ and f_{ig}, thus imparting a grain size-dependence on the effective coordination in the intergranular region.

The second equilibrium condition of Eq. (2.18b) is analogous to imposing $\gamma \rightarrow 0$, as the alloy grain boundary energy, γ, is directly related to the partial derivative:

$$\gamma = \frac{t}{\Omega} \cdot \frac{\partial \Delta G_{mix}}{\partial f_{ig}} \tag{2.21}$$

where the scaling factor t/Ω is the reciprocal of the proportionality constant introduced in Eq. (2.16). To calculate corresponding equilibrium grain sizes for the solute distributions given by Eqs. (2.7) and (2.19), Eq. (2.18b) must be concurrently evaluated and introduced into Eq. (2.21):

$$\begin{aligned}\gamma = \gamma_A - \frac{ztX_{ig}}{\Omega}\left[\omega_b - \omega_{ig}\left(1-\frac{\upsilon}{1-f_{ig}}\right) - \frac{\Omega}{zt}\left(\gamma_B-\gamma_A\right)\left(1-\frac{\upsilon}{1-f_{ig}}\right)\right] - \ldots \\ \ldots - \frac{zt}{\Omega}\left[\left(X_b^2 - 2X_bX_{ig}\right)\omega_b + X_{ig}^2\omega_{ig}\left(1-\frac{\upsilon}{1-f_{ig}}\right)\right] + \ldots \\ \ldots + \frac{zt\upsilon}{\Omega\left(1-f_{ig}\right)}\left[\left\{X_{ig}\left(X_{ig}-X_b\right) + X_b\left(1-X_{ig}\right)\right\}\omega_{ig} + X_b\frac{\Omega}{zt}\left(\gamma_B-\gamma_A\right)\right] + \ldots \\ \ldots + \frac{tkT}{\Omega}\left[X_{ig}\ln\left(\frac{X_{ig}}{X_b}\right) + \left(1-X_{ig}\right)\ln\left(\frac{1-X_{ig}}{1-X_b}\right)\right] = 0\end{aligned} \tag{2.22}$$

While Eq. (2.22) appears cumbersome at first glance, its form can be understood by considering a simplified system: one in which we assume a dilute solute concentration (X→0), a high segregation tendency ($\Delta H_{seg} >> kT$), and McLean-type segregation ($f_{ig} \rightarrow 0$), assumptions that were central in the prior models of nanostructure stability by Weissmüller [177] and Liu and Kirchheim [183]. Under these simplifying conditions, with υ=1/2, the isotherm and alloy grain boundary energy simplify to:

$$\Delta H_{seg}^{o} = z\left[\omega_b - \frac{\omega_{ig}}{2} - \frac{\Omega}{2zt}\left(\gamma_B-\gamma_A\right)\right] \tag{2.23a}$$

$$\gamma = \gamma_A - \frac{tX_{ig}}{\Omega}\left[\Delta H_{seg}^{o} + kT\ln\left(X_b\right)\right] \tag{2.23b}$$

where Eq. (2.23a) characterizes McLean-type segregation, as discussed above in reference to the leading term of Eq. (2.20). Eq. (2.23b) is incorporated as the leading two terms of Eq. (2.22), and simplifies exactly to Eq. (1.5); the solute excess in this dilute, infinite grain size limit is expressed as:

$$\Gamma\big|_{X,f_{ig}\rightarrow 0} = \frac{t\cdot X_{ig}}{\Omega} \tag{2.24}$$

which is identical to the form provided in Ref. [183]. Higher order effects from solute-solute and solute-solvent interactions in the bulk, transitional, and intergranular regions are captured by the remaining terms in Eq. (2.22).

The true equilibrium state of a polycrystal is determined by simultaneously applying the two criteria of Eqs. (2.18) recast as Eqs. (2.19) and (2.22), and solving for the two unknowns, intergranular solute content and grain size. Because constant X is imposed, the equilibrium grain size is coupled to the global solute content; for any given composition there is one equilibrium grain size, and for any grain size there is one energy-minimizing composition. To illustrate this more clearly, we have plotted ΔG_{mix} as a function of the two unknown variables, X_{ig} and d, in Figure 2.2 for a representative set of interaction energies at a given composition of X = 10 at %.

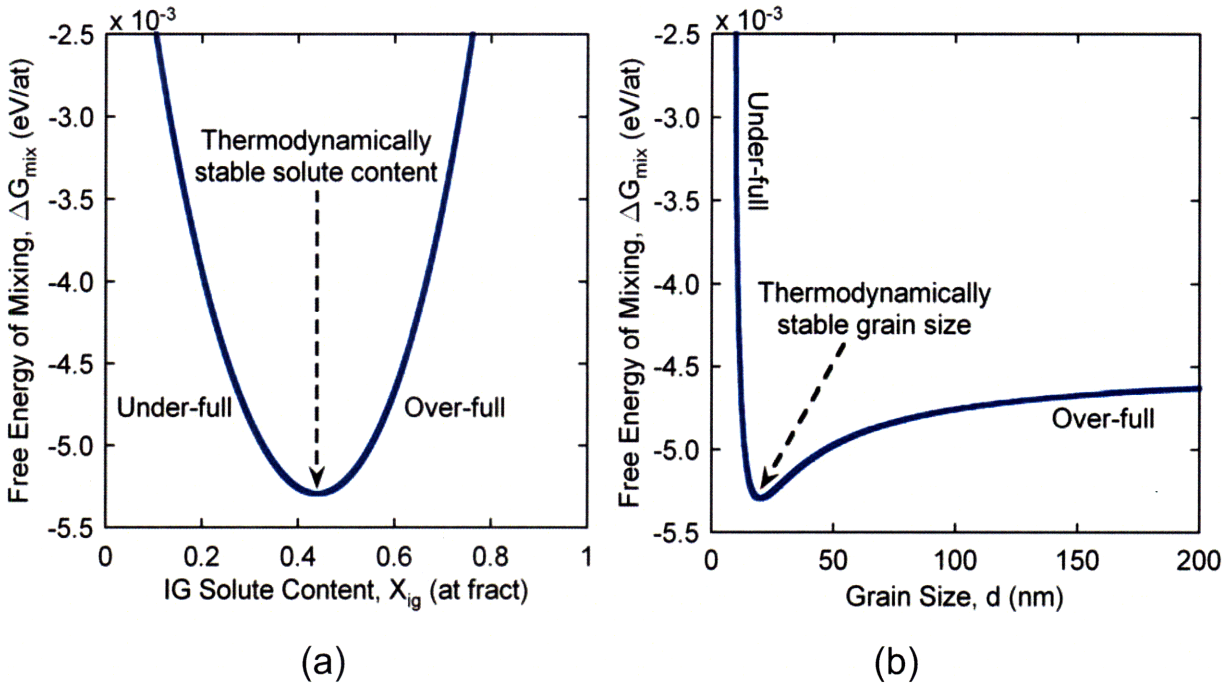

Figure 2.2: Two dimensional slices of the free energy surface as a function of (a) the intergranular solute content at a grain size of 20 nm, and (b) grain size at an intergranular solute content of 44 at %, for a given global composition of 10 at %. The minimum identified in the free energy of mixing represents the global minimum, and defines the thermodynamically stable state: note that these two sections have been chosen such that they each intersect the true energy minimum, whereas plots of Eq. (2.17) as a function of either variable alone would generally not.

For a fixed grain size of d = 20 nm, the free energy monotonically decreases when solute is initially added to the system, as observed in Figure 2.2(a). In order to satisfy Eq. (2.19) and reach a thermodynamically stable solute content, enough solute must be supplied to minimize ΔG_{mix} as indicated; at lower solute contents, the grain boundaries can be viewed as "under-full" with additional sites available for solute atoms, whereas when X_{ig} surpasses the stable composition, the grain boundaries become saturated and solute atoms occupy energetically unfavorable sites in the bulk, resulting in the subsequent increase in ΔG_{mix}. Similarly, for the equilibrium solute content identified in Figure 2.2(a), the grain size corresponding to the minimum ΔG_{mix} identified in Figure 2.2(b) represents the thermodynamically stable grain size, with $\gamma = 0$. Grain sizes less than the equilibrium value can again be characterized as having "under-full" grain boundaries with $\gamma > 0$, while larger grain sizes (i.e. lower f_{ig} or grain boundary area) contain "over-full" grain boundaries with a higher ΔG_{mix}.

The minimization procedure described above can be employed to calculate equilibrium grain sizes and intergranular solute contents as a function of global composition for alloys with various interaction energies. The prototypical output of this model is illustrated in Figure 2.3 for one specific set of interaction energies: the equilibrium grain size decreases with increasing global solute content in a power-law-like decay. The functional form of this relationship is a signature of thermodynamic stabilization, and is widely observed in experimental data [77, 176, 182-184]. Such scaling is an inherent consequence of Eq. (2.6), where the grain boundary volume fraction is inversely related to grain size. Additional solute is thus required to effectively fill the grain boundaries and lower the system energy, especially at the finest nanocrystalline grain sizes where interfaces become the dominant structural feature.

While grain size correlates with the global composition, the corresponding segregation isotherm in Figure 2.4 indicates that the intergranular composition is unaffected by solute additions. However, because d is coupled to X, the interfacial volume fraction varies with global

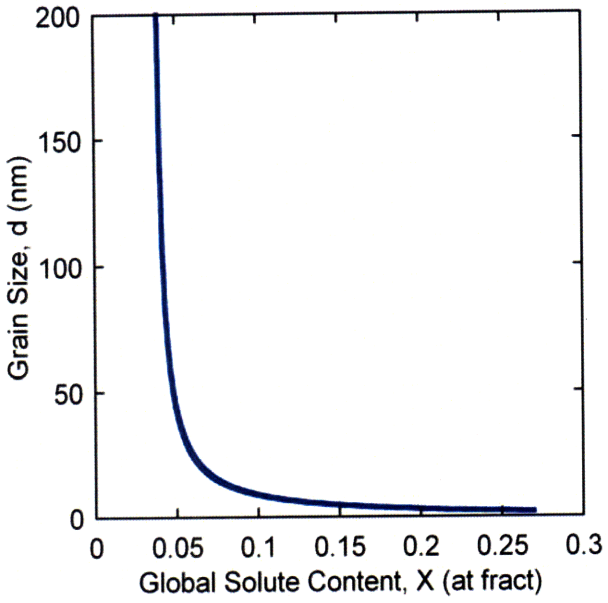

Figure 2.3: Equilibrium grain size as a function of the global solute content for a given set of interaction energies. A power-law-like decay in grain size is observed with increasing global composition, indicating that more solute is required to stabilize finer nanocrystalline grain sizes.

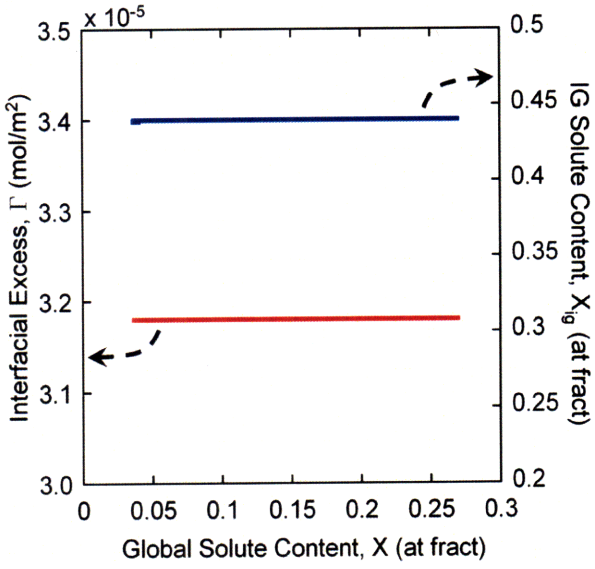

Figure 2.4: Interfacial excess and intergranular solute content plotted against the global solute content; the corresponding axes are indicated. For the given set of interaction energies, both quantities are independent of global composition, and thus denote the critical intergranular coverage level required to achieve equilibrium.

composition, making it very difficult to analyze the segregation behavior from a characteristic isotherm. To address this complexity, we turn our attention to an alternate thermodynamic quantity commonly employed in describing solute segregation to surfaces: the Gibbsian excess, or intergranular solute excess, Γ [180, 200], which is derived by considering the distribution of atoms, N, in the system:

$$\Gamma = \frac{1}{A_{ig}}\left[N_{ig}^{B} - N_{b}^{B}\left(\frac{N_{ig}^{A}}{N_{b}^{A}}\right)\right] \tag{2.25}$$

This representation is convenient as Γ is normalized by the interfacial area, A_{ig}, thus incorporating the inherent variation in interfacial volume fraction. A_{ig} can be calculated from the system volume, V_T, and the intergranular volume fraction and shell thickness:

$$A_{ig} = \frac{V_T \cdot f_{ig}}{t} \tag{2.26}$$

When Eq. (2.26) is introduced into Eq. (2.25), the interfacial excess takes the form:

$$\Gamma = \frac{\eta t\left(X_{ig} - X_b\right)}{1 - X_b} \tag{2.27}$$

where the scaling factor, η, is the ratio of the density to atomic weight, and is required to convert atomic fraction to mole concentration. This expression simplifies exactly to Eq. (2.24) in the dilute, infinite grain size limit, with $\eta = 1/\Omega$. Introducing the results for X_{ig}, X, and f_{ig} from the segregation isotherm into Eq. (2.27), we obtain Γ as a function of X, as illustrated in Figure 2.4. As the segregation isotherms imply, the interfacial excess is indeed unaffected by solute additions for the given set of energetic state variables. However, this does not imply that Γ is universally independent of X, and is only observed here as a consequence of the chosen interaction energies. This will be demonstrated in the following parametric study, which will

also emphasize the importance of incorporating grain size variations when analyzing segregation behavior.

2.2 Parametric study

The equilibrium equations derived in Section 2.1 are parameterized by a number of geometric and thermodynamic state variables that influence both the segregation tendency and equilibrium grain size, including T, ω_b, ω_{ig}, γ_A^o, γ_B^o, and D. In this section, we will illustrate the individual effects of these parameters by numerically evaluating Eqs. (2.19) and (2.22) to solve for equilibrium pairs of d and X, with an assumed constant intergranular shell thickness of t = 0.5 nm.

2.2.1 Temperature

The free energy of mixing is derived here for a system limited to pairwise nearest-neighbor interactions, an assumption that leads to a temperature-independent enthalpy, with T predominantly coupled to the entropy via Eq. (2.10). To evaluate the influence of temperature, state variables are assigned such that the driving force for segregation is derived from bulk interactions for three-dimensional grains with ideal intergranular interactions, and additional influences from other system parameters are minimized: ω_b = 0.03 eV (~2.9 kJ/mol), ω_{ig} = 0 eV, $\gamma_A^o = \gamma_B^o$ = 0.48 J/m^2, and D = 3.

The most general influence of temperature, due to its connection to entropy, is to randomize the distribution of solute throughout the system, thus desegregating systems that exhibit a segregation tendency. Figure 2.5(a) illustrates that temperature lowers the segregation energy, indeed suggesting that the system prefers a more random configuration. Equilibrium grain size decreases with global composition in Figure 2.5(b), and the temperature-dependent segregation energy affects this scaling in subtle and complex ways. First, for lower global compositions (X < 10 at %), the reduced driving force for segregation at elevated temperatures results in a lower interfacial excess, as evidenced in Figure 2.5(c), and the system therefore requires more solute to effectively eliminate the alloy grain boundary energy; this is manifested in Figure 2.5(b) as a

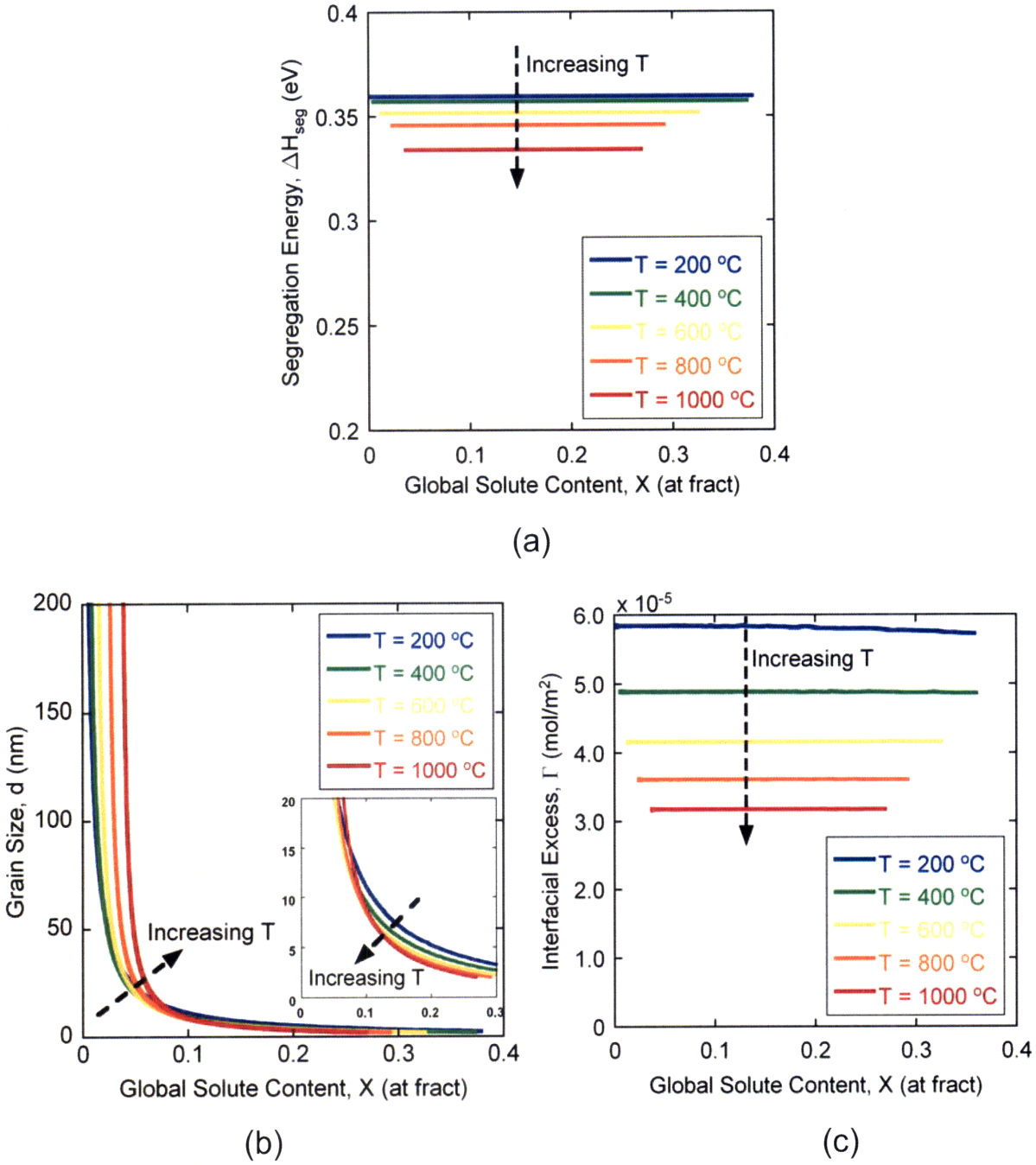

Figure 2.5: Thermodynamic equilibrium states as a function of temperature for interaction energies defined as: ω_b = 0.03 eV, ω_{ig} = 0 eV, and $\gamma_A^o = \gamma_B^o$ = 0.48 J/m^2. With increasing temperature, (a) the segregation energy decreases, (b) the grain size trends first shift to higher solute contents, followed by a scaling inflection and shift to lower global compositions as shown in the inset, and (c) the interfacial excess decreases, indicating that temperature promotes a more random solute distribution.

shift of the d-X trends to higher global compositions. However, as X is increased beyond 10 at%, the d-X trends instead shift to lower global compositions with increasing T, as demonstrated in the inset of Figure 2.5(b). While this appears counter-intuitive, the observed reduction in Γ (cf. Figure 2.5(c)) indicates that the system transitions to a more random configuration with increasing X, which is favored at elevated temperatures. Less solute is required to achieve equilibrium in a more random system, thus accounting for the observed inflection in the scaling of the grain size-composition relationships with temperature.

2.2.2 Bulk interaction energy

The bulk interaction energy is one of the principal driving forces for segregation as it directly scales with the heat of mixing. Accordingly, in this section we examine the influence of ω_b, for fixed values of the remaining state variables: T = 1000°C, ω_{ig} = 0 eV, $\gamma_A^o = \gamma_B^o$ = 0.48 J/m^2, and D = 3. An elevated temperature is employed to study the effect of ω_b (in competition with entropy) over a more extensive range of values.

The segregation energy, shown in Figure 2.6(a), markedly increases with increasing ω_b, as expected from Eq. (2.20); all other things being equal, higher heat-of-mixing alloys should exhibit a greater tendency for segregation. The resulting effect on the equilibrium grain size-composition relationships is shown in Figure 2.6(b); for greater values of ω_b, less global solute is required to stabilize a given nanocrystalline grain size, thereby shifting the characteristic d-X trends downward. However, the effect of ω_b on the interfacial excess, illustrated in Figure 2.6(c), is more complex. For low bulk interaction energies (ω_b < 0.05 eV), the interfacial excess is independent of global composition, as shown specifically for ω_b = 0.04eV; further decreasing ω_b reduces the interfacial excess, and such trends are not included in Figure 2.6(c) for clarity of presentation. As ω_b is increased beyond 0.05 eV, not only do the bulk atomic interactions more strongly dictate the segregation behavior, like bond formation also becomes more energetically favorable in the bulk. At higher global compositions where the probability to form like bonds is greatly enhanced, solute atoms prefer to occupy bulk sites to minimize the system free energy. This leads to a more rapid decrease in Γ with increasing X, as observed in Figure 2.6(c), especially when ω_b exceeds 0.06 eV.

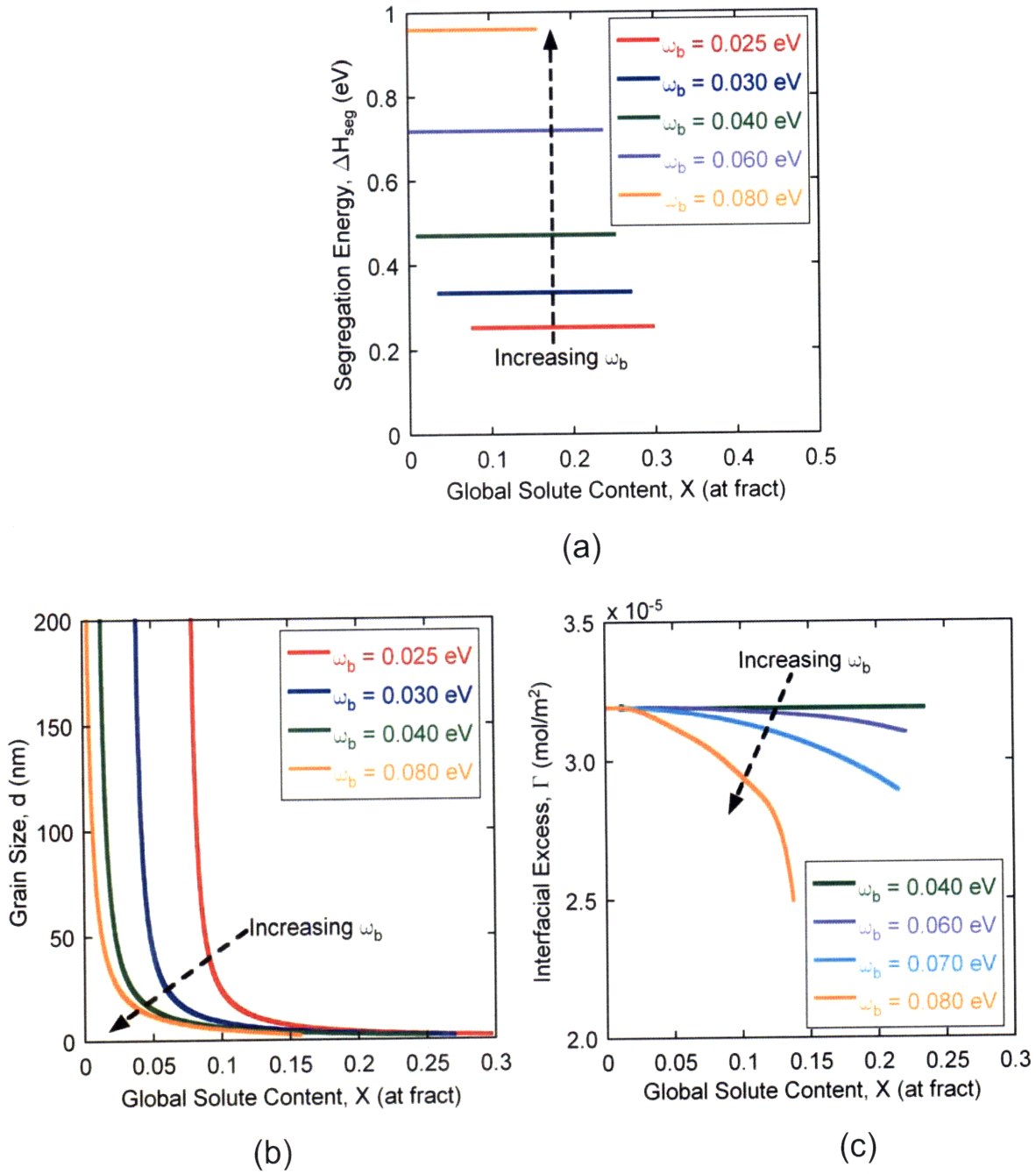

Figure 2.6: Thermodynamic equilibrium states as a function of the bulk interaction energy for the state variables: T= 1000 °C, ω_{ig} = 0 eV, and $\gamma_A^o = \gamma_B^o$ = 0.48 J/m^2. With increasing bulk interaction energy, (a) the segregation energy increases and (b) the grain size trends shift to lower global solute contents, indicating that less solute is required to stabilize the nanostructure for large bulk interaction energies. (c) The interfacial excess is initially independent of composition at low ω_b, then scales with the global solute content as ω_b further deviates from ω_{ig}.

2.2.3 Intergranular interaction energy

One of the essential features of the present model is its adaptability to a variety of alloy systems via distinct, tunable mixing energies. For clarity in evaluating the effect of T and ω_b in the previous sections, the intergranular region was assumed to behave as an ideal solution, with no particular inclination for specific bond types. In this section, the intergranular interaction energy is varied and the results are contrasted with the effect of the bulk interaction energy. While we focus mostly on positive interaction energies, $\omega_{ig} < 0$ is also briefly investigated to impart a preference for unlike bonds in the intergranular region. The remaining state variables are defined as: T = 1000°C, ω_b = 0.03 eV, $\gamma_A^o = \gamma_B^o$ = 0.48 J/m^2, and D = 3, where the elevated temperature is employed to facilitate comparisons with the previous section.

The equilibrium results are summarized in Figure 2.7 as a function of ω_{ig}, and generally exhibit opposite trends as compared to the effect of ω_b. Figure 2.7(a) illustrates that as ω_{ig} is increased, a noticeable reduction in the driving force for segregation results, owing to the enhanced energetic penalty imparted on segregating atoms. The equilibrium d-X relationships, shown in Figure 2.7(b), shift to higher global compositions to counteract the reduced driving force for segregation. A second, less pronounced effect is exhibited in the scaling of ΔH_{seg} and Γ with global composition. The inclination for unlike bonding when $\omega_{ig} < 0$ eV, as substantiated by the lower interfacial excess in Figure 2.7(c), leads to a slight reduction in the segregation energy at higher global compositions (where the formation of like bonds is more probable) in Figure 2.7(a); the interfacial excess also exhibits a decrease with increasing X. Conversely, a higher interfacial excess, reduced driving force for segregation, and subtle increase in ΔH_{seg} and Γ (with increasing X) is observed when $\omega_{ig} > 0$, which can be attributed to the energetic preference for like bond formation.

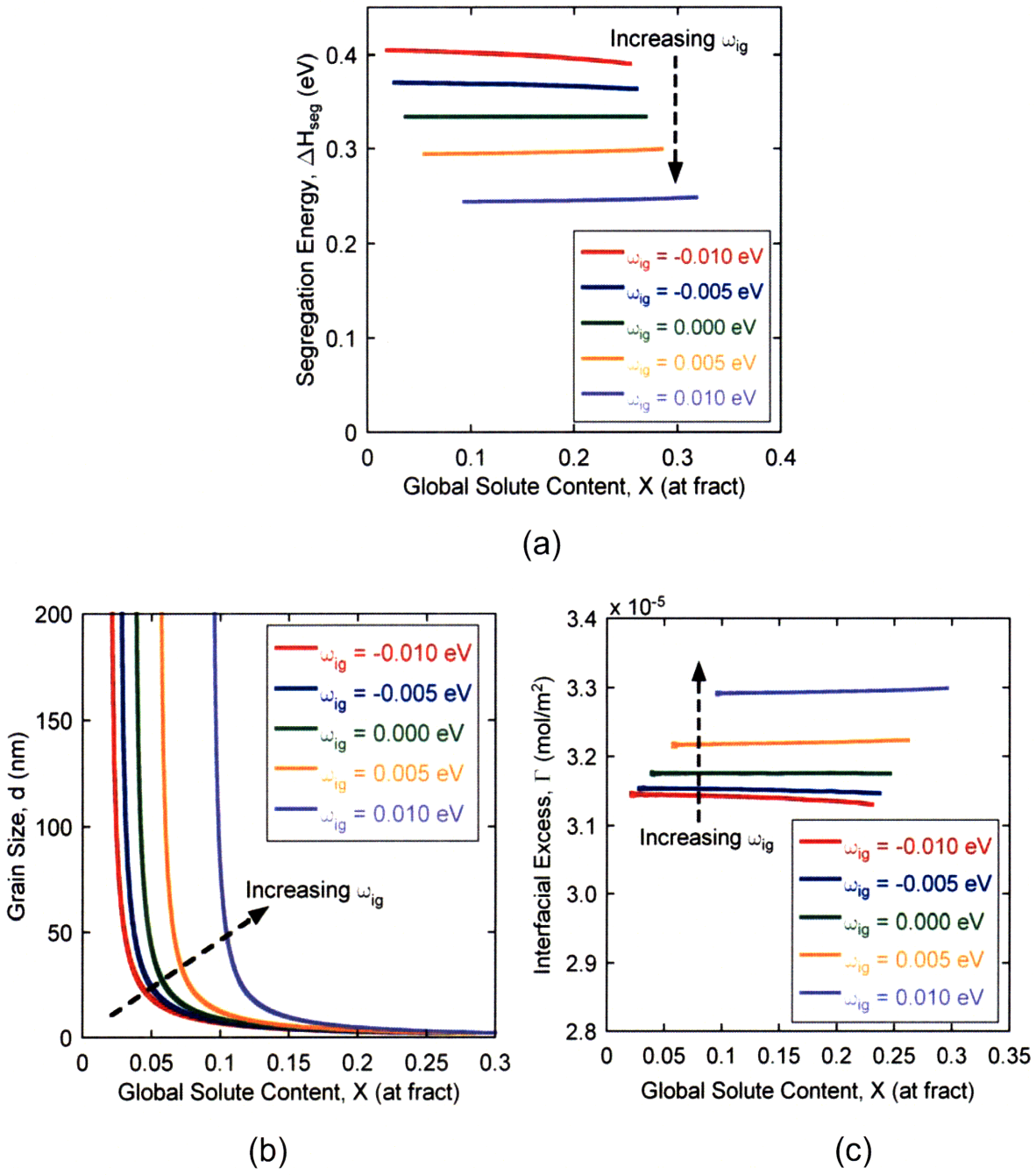

Figure 2.7: Thermodynamic equilibrium states as a function of the intergranular interaction energy for the state variables: T= 1000 °C, ω_b = 0.03 eV, and $\gamma_A^o = \gamma_B^o$ = 0.48 J/m^2. With increasing intergranular interaction energy, (a) the segregation energy decreases, (b) the grain size trends shift to higher global solute contents, and (c) the interfacial excess increases towards higher coverage levels, all of which support that higher solute contents are required to stabilize the nanostructure as ω_{ig} tends towards large, positive values.

2.2.4 Solvent grain boundary energy

The final two energetic state variables are the single component grain boundary energies, γ_A^o and γ_B^o, which in earlier computations have been assumed to be equal for simplicity. In this section, we will systematically vary γ_A^o, while γ_B^o is held constant at 0.48 J/m^2. The remaining parameters are defined as: T = 1000°C, ω_b = 0.03 eV, ω_{ig} = 0 eV, and D = 3. Whereas the driving force for segregation in earlier sections derived from the interaction energies fromo the bulk and intergranular regions, the differential between the pure component grain boundary energies further contributes to the segregation behavior in the subsequent results.

Figure 2.8(a) shows the dependence of the segregation energy on γ_A^o as a function of global solute concentration. Because a greater energetic penalty is imposed on atoms occupying intergranular sites as γ_A^o is increased, the desire for solute atoms to segregate to the grain boundaries diminishes, with a corresponding decrease in ΔH_{seg}. However, since equilibrium requires segregated solute to counteract the interfacial energy, more solute should be required to effectively eliminate a higher grain boundary energy, as is indeed observed in Figure 2.8(b and c) via an upward shift of the d-X relationships and the interfacial excess with increasing γ_A^o. While not shown here, the same basic trends are observed with variations in γ_B^o, although they are much less prominent since we are dealing with A-rich alloys.

The segregation energy also varies with X for various values of γ_A^o, and specifically depends on the relative difference between γ_A^o and γ_B^o. When $\gamma_A^o > \gamma_B^o$, a decrease in the segregation energy is observed with increasing global composition, while the opposite trend is realized when $\gamma_A^o < \gamma_B^o$. For the case where $\gamma_A^o > \gamma_B^o$, an A-rich boundary is characterized by a higher energy and lower driving force for segregation, as discussed above, leading to the observed decrease in ΔH_{seg} with X. The converse case follows the same logic, and when $\gamma_A^o = \gamma_B^o$, the nature of the boundaries no longer influences the propensity for segregation, as illustrated by the composition-independent segregation energy in Figure 2.8(a).

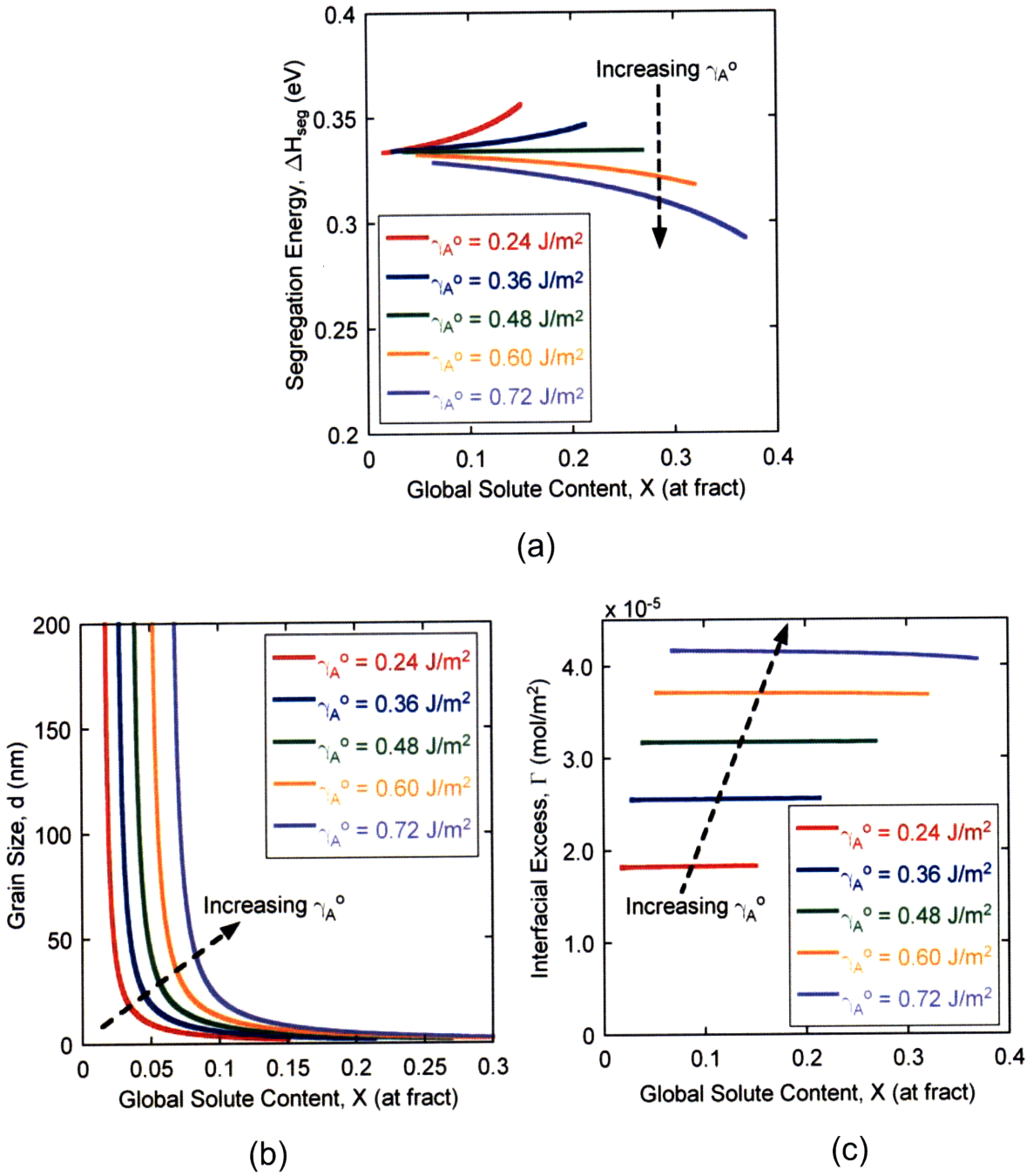

Figure 2.8: Thermodynamic equilibrium states as a function of the solvent grain boundary energy for the state variables: T= 1000 °C, ω_b = 0.03 eV, and ω_{ig} = 0 eV . With increasing grain boundary energy, (a) the segregation energy generally decreases, although, depends to a large extent on the global solute content and relative magnitudes of the solute-solvent grain boundary energies, (b) the grain size trends shift to higher global solute contents, and (c) the interfacial excess increases towards higher coverage levels. These observations indicate that more solute is required to drive higher energy grain boundaries to equilibrium.

2.2.5 Grain structure dimensionality

The present model does not require specification of a distinct grain shape, but the dimensionality of the grains affects the scaling of grain boundary volume fraction with grain size via Eq. (2.6), and thus impacts the final equilibrium state. The state variables are again assigned such that the sole driving force for segregation is derived from bulk interactions: T = 100 °C. ω_b = 0.03 eV, ω_{ig} = 0 eV, and $\gamma_A^o = \gamma_B^o$ = 0.48 J/m^2.

For the chosen set of energetic state variables, the segregation energy is calculated to be 0.36 eV, and is independent of both dimensionality and global composition. However, the equilibrium grain size-global composition relationships are a function of grain dimension in Figure 2.9(a).

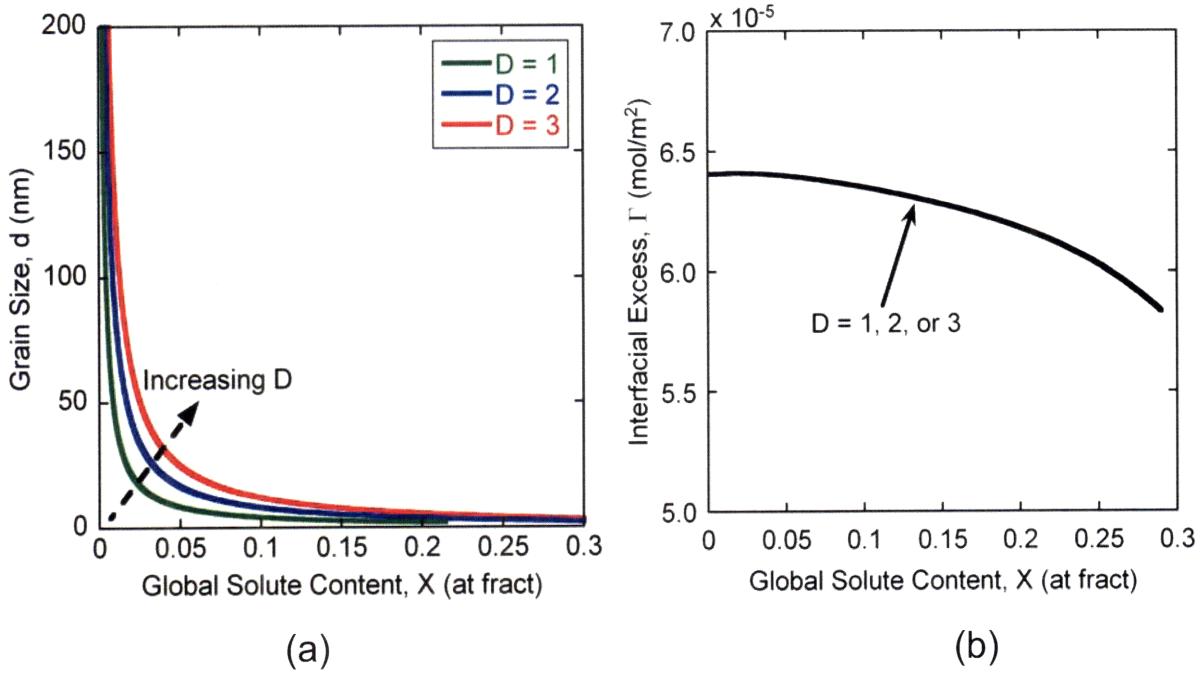

Figure 2.9: (a) Equilibrium grain size vs. global composition as a function of grain structure dimensionality. (b) Interfacial excess plotted for D = 1, 2, or 3 as a function of global solute content. The trends in (a) shift to higher global solute contents as D increases, attributed to the concurrent increase in grain boundary volume fraction. The interfacial excess in (b) is independent of dimensionality, and its functional dependence on X is imparted by the assigned state variables.

As D increases, the d-X curves shift to higher global compositions for the same solute distribution. According to Eq. (2.6), for a specified grain size and intergranular shell thickness, the intergranular volume fraction exponentially increases with grain dimension, and additional solute is therefore required to effectively eliminate the alloy grain boundary energy at higher f_{ig}. However, the critical interfacial excess required for $\gamma \to 0$ is independent of grain dimensionality, as shown in Figure 2.9(b), and decreases with X to reduce the probability for energetically-unfavorable solute-solute interactions in the grain boundary.

2.3 Implications for design of stable nanocrystalline alloys

In the previous section, the contribution of each of the thermodynamic state variables central to segregation-induced nanostructure stabilization were systematically investigated, and the results illustrated the importance of considering the effects of all the energetic parameters that characterize binary alloy systems. In particular, the bulk interaction energy and relative magnitudes of the elemental grain boundary energies strongly influenced the nature of the grain size-composition trends, segregation energy, and solute distribution. The intergranular interaction energy also plays a role in nanostructure formation, although can be anticipated to scale with the bulk interaction energy for a given alloy system. Interestingly, the bulk interaction energy is directly related to the heat of mixing, which was used in Section 1.3 in distinguishing various alloy systems. Generally speaking, two elements with a high positive heat of mixing will be immiscible, with an enhanced propensity for like bond formation. At first glance, this indicates that a high positive heat of mixing system would be desired to promote preferential occupation of grain boundary sites with solute atoms, leading to a higher intergranular excess and greater reduction of the alloy grain boundary energy via Eq. (2.23b). This has motivated a number of studies on nanostructure formation in highly immiscible systems, such as Ni-P [183] and Y-Fe [182].

Before discussing the implications of the present analytical results for alloy design, two criteria essential to the production of stable nanocrystalline specimens from binary systems can be established. First, grain sizes across the entire nanocrystalline regime should be accessible by

control over the alloy composition. Second, subtle compositional fluctuations should not generate large variations in grain size, i.e. a grain size-composition trend with a more moderate curvature is desirable. Referring back to Figure 1.6, Ni-P with a high heat of mixing of ~60 kJ/mol (~0.63 ev/at) [201-203], does not fulfill either one of these criteria, exhibiting only a very limited range of attainable nanocrystalline grain sizes, which increases suddenly at ~3 at % P. This demonstrates that although a high heat of mixing may promote grain boundary segregation, as confirmed in the atom probe tomography experiments on Ni-P [191], it does not necessarily offer the desired control over the nanostructure.

We can now turn our attention to the results from the present analytical model to identify a preferable alloy system based on the criteria presented above. The arguments in Section 2.2.2 demonstrate that while a high bulk interaction energy (i.e. high heat of mixing) will promote nanostructure formation at lower solute contents, the grain size-composition trend will have a relatively high curvature, in line with the experimental observations in the Ni-P system. A more moderate heat of mixing will shift these trends to higher solute contents with a more moderate curvature; higher grain boundary energies will also promote this effect, after Section 2.2.4. As such, a system with a lower positive heat of mixing and higher grain boundary energy should produce stable nanocrystalline alloys with enhanced tailorability of the nanostructure. The Ni-W alloy system, also illustrated in Figure 1.6, exhibits a more moderate heat of mixing of ~26 kJ/mol (~0.27 eV/at) [201-203], which in the context of the present thermodynamic model, will promote a larger range of achievable nanocrystalline grain sizes at higher alloy compositions. Figure 2.10 illustrates the grain size-composition trends computed for both high and low heat of mixing systems, with the magnitudes of ΔH_{mix} modeled after the Ni-P and Ni-W systems, respectively; these results were calculated at an identical temperature of 100 ^{o}C. Whereas the high ΔH_{mix} trend exhibits a relatively sharp increase in grain size at a low global solute content of ~3 at %, analogous to the Ni-P data in Figure 1.6, the low ΔH_{mix} trend is shifted to higher global solute contents with a more moderate curvature, in line with the Ni-W experimental results. Low heat of mixing alloy systems will therefore offer more precise control of the nanocrystalline grain size through manipulation of the alloy composition, representing an improved methodology for producing nanocrystalline samples for systematic studies of material properties.

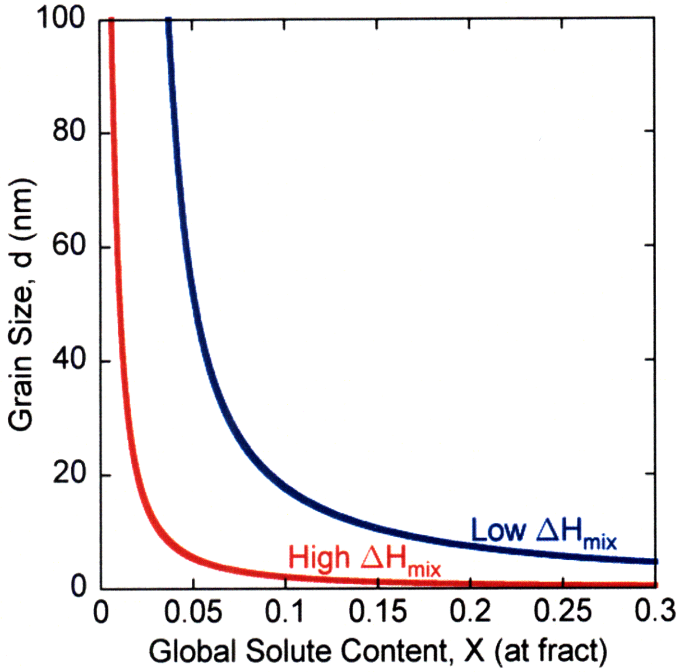

Figure 2.10: Grain size as a function of global composition for high and low heat of mixing systems. The low ΔH_{mix} trend is shifted to higher global solute contents, and exhibits a more moderate curvature as compared to the high heat of mixing system.

2.4 Concluding remarks

Within the framework of statistical thermodynamics, we have developed an analytical model for nanostructure stabilization in binary alloy systems, extending previous works to more general segregation behavior and alloy compositions. Global energetic variables were identified from the various bond energy combinations in the free energy of mixing, and their influence on the equilibrium states were investigated in a parametric study, revealing that:

- A reduced segregation energy is exhibited by systems with a lower bulk interaction energy, higher intergranular interaction energy, and a higher solvent grain boundary energy.
- Lower segregation energies generally shift the equilibrium grain size-composition trends to higher global compositions, and promote a more subtle decrease in grain size with increasing global solute content.

- The interfacial excess is not only influenced by the absolute value of the segregation energy, but depends strongly on the mixing behavior defined by the relative magnitudes of the interaction and grain boundary energies.
- All other things being equal, temperature acts to randomize the solute distribution, generally shifting the grain size-composition trends to higher global solute contents..

In light of these results, we were able to address differences among two alloy systems frequently used in the synthesis of nanocrystalline specimens, including Ni-P and Ni-W, and rationalize the conflicting grain size-composition trends. We demonstrated that the lower heat of mixing associated with the Ni-W system will enable a larger range of achievable grain sizes, with more precise tailorability of the nanostructure. While this has been addressed specifically for Ni-W, these guidelines indicate that a range of nanocrystalline grain sizes should be accessible by tailoring the alloy composition for a binary system exhibiting a more moderate positive heat of mixing. For the purposes of this thesis, the Ni-W alloy system will be the basis for the production of nanocrystalline alloys with grain sizes spanning the entire Hall-Petch breakdown regime. In the chapters that follow, we first introduce the processing techniques used to tailor the W content for the fabrication of nanocrystalline specimens, and then present a detailed study of their mechanical behavior across the Hall-Petch breakdown regime.

Chapter 3: Experimental materials

Of the potential routes for producing nanocrystalline alloys highlighted in Section 1.3, electrodeposition is one of the more promising techniques, owing to its ability to synthesize homogeneous, high-quality specimens suitable for mechanical testing [5, 18, 151]. Our results from the analytical model developed in Chapter 2 support the study of Ni-W alloys as compared with other options (such as Ni-P); the considerable solid solubility of W in the Ni lattice derives from a moderate positive heat of mixing, in turn leading to a broader range of accessible grain sizes. As suggested by Fig. 1.6, the grain size in Ni-W can span from the conventional ultrafine range to the amorphous limit, with a fine degree of control especially in the range of the Hall-Petch breakdown near ~10-20 nm. A number of electrodeposition studies [77, 82, 186-188, 204-220] have been performed to characterize the processing-structure relationships for this alloy system, and we exploit the reverse pulsing technique described in Ref. [77] to manipulate the grain size by precise control of the alloy composition.

In this chapter, we first introduce the set-up and procedure for depositing Ni-W alloy films of 50-100 μm thickness from an aqueous electroplating solution. The characterization procedures used to verify deposit composition, structure, and quality are subsequently discussed. Deposition conditions and structural characterization results are presented for the as-deposited samples used in Chapters 4 and 5, and linked to the resultant alloy composition and grain size. Several specimens are also subjected to a number of isothermal heat treatments prior to the mechanical testing discussed in Chapter 6, for which the annealing conditions and structural characterization results are finally presented.

3.1 Electrodeposition procedures

Ni-W alloys of varying composition have been electrodeposited from an ammoniacal citrate electrolyte solution, with a composition described in Table 3.1 after Yamasaki et al. [188]. Nickel sulfate and sodium tungstate are the metal salts, sodium citrate and ammonium chloride are complexing agents required to facilitate the co-deposition of Ni and W [215], and sodium

Table 3.1: Chemical composition of the ammoniacal citrate plating bath used in the synthesis of the present nanocrystalline Ni-W alloys, following Ref. [188].

Chemical	Formula	Concentration (g/L)
Nickel sulfate hexahydrate	$(NiSO_4 \cdot 6H_2O)$	15.8
Sodium tungstate dihydrate	$(Na_2WO_4 \cdot 2H_2O)$	46.2
Sodium citrate dihydrate	$(Na_3C_6H_5O_7 \cdot 2H_2O)$	147.1
Ammonium chloride	(NH_4Cl)	26.7
Sodium bromide	(NaBr)	15.4

bromide is used to increase the conductivity of the bath and promote specific reactions at the anode. The plating solution, isolated in a beaker, was submerged in a heated oil reservoir maintained at a constant temperature via a VWR immersion circulator model #1122S, and stirred at a rate of ~150 RPM. Commercial purity nickel sheet has been used as the cathode (substrate), with an area of ~12 cm^2 polished to a mirror-like finish via standard metallographic techniques, and inert platinum gauze was used for the anode. A bias was generated between the electrodes using a Dynatronix series PDPR40-50-100 or DPR 20-30-100 power supply using either direct current, or in many cases, reverse pulsing.

A schematic of the pulsing sequence is shown in Figure 3.1, with the magnitude and duration of

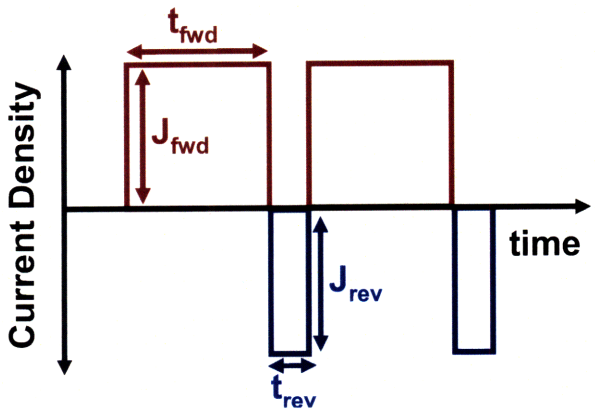

Figure 3.1: Schematic of the pulse cycling used in the deposition of Ni-W alloys, where the magnitude of the reverse pulse current density is varied to manipulate alloy composition, after Detor et al. [77].

each pulse defined by the current density, J, and pulse duration, t, respectively; the subscripts distinguish forward (fwd) and reverse (rev) pulse cycles. For the present work, no off-time was applied during any of the depositions. The alloy composition was controlled by manipulating this current waveform, more specifically the magnitude of the reverse current density, J_{rev}, after Detor and Schuh [77]; this can also be accomplished by varying t_{rev}, although the results are more difficult to reproduce. In some cases, temperature was also included as an additional variable to synthesize a particular solute content specimen, predominantly at the finest nanocrystalline grain sizes. The connection between these processing variables and the as-deposited specimen characteristics are considered in Section 3.3.

3.2 Characterization procedures

Following deposition, specimens were subjected to a series of characterization procedures to ensure they were suitable for nanomechanical testing. Alloy composition was measured to ± 1 at% via energy dispersive spectroscopy (EDS) (X-ray Optics/AAT) in a Leo 438VP scanning electron microscope (SEM). Both planar and cross-sectional SEM was used to measure the deposit thickness, and confirm that each sample was free of processing-induced defects, such as microcracking, pororsity, and/or inclusions. X-ray diffraction (XRD) was performed using a Rigaku RU300 diffractometer operating at 50 kV and 300 mA, in order to (a) confirm that each deposit was a polycrystalline single-phase FCC solid solution, and (b) estimate the mean grain size. Grain size was quantified to ±25 % by applying the integral breadth method [221] to the {111} family of peaks using the Jade software package, and as observed in Refs. [77, 78, 188, 190, 205, 219], such measurements are accurate for nanocrystalline Ni-W. The measured XRD grain sizes were verified on a variety of samples[1] by transmission electron microscopy (TEM), using a JEOL 2010 operating at 200 kV. Specimens were prepared by twin-jet-electropolishing at 10 V, in a 2:1 methanol-nitric acid solution at -60 °C.

[1] Dr. A.J. Detor is gratefully acknowledged for performing some of the transmission electron microscopy

3.3 As-deposited Ni-W alloys by electrodepositon

Across the entire Hall-Petch breakdown regime, nine distinct grain size specimens were produced via electrodeposition, and Table 3.2 summarizes the bath temperatures and pulsing magnitudes used in each deposition. In particular, the W content scales inversely with the

Table 3.2: Deposition conditions for the specimens used in evaluating the mechanical properties at room temperature in Chapters 4 and 5. The table is organized according to descending grain size, as listed in the first column.

Grain Size (nm)	Composition (at % W)	J_{fwd} (A/cm^2)	t_{fwd} (ms)	J_{rev} (A/cm^2)	t_{rev} (ms)	Bath Temp. (°C)
150	1.5	0.2	20	0.3	3	75
95	2.6	0.2	20	0.25	3	75
75	3.9	0.2	20	0.2	3	75
55	4.6	0.2	20	0.2	3	75
40	7.4	0.2	20	0.15	3	80
20	15.2	0.2	20	0.1	3	75
12	17.9	0.2	20	0.05	3	75
6	21.3	0.2	DC			75
3	26.6	0.25	DC			95

reverse pulse current density, indicating that W is selectively removed during the reverse pulse cycle. Reverse pulsing over a specific potential range has been suggested to preferentially strip select elements during the deposition process [220, 222-228]. Temperature also critically influences the alloy composition, with higher bath temperatures promoting W incorporation in the as-deposited films; this is most readily observed for the 40 and 55 nm grain size samples, where for all other things being equal, the sample deposited at 80 °C exhibits a W content 50% greater as compared to the 75 °C deposition. The higher bath temperatures have been suggested to promote ionic diffusion of the slower moving W-containing species, thus enhancing the amount of W available in the boundary layer for deposition onto the cathode [204]. Temperature-induced solute incorporation is especially useful in achieving extremely fine nanocrystalline structures.

Figure 3.2 shows the XRD spectra for select specimens employed in this study, labeled according to the mean grain size as quantified from the observed peak broadening; three additional samples with grain size 55, 95 and 150 nm, as listed in Table 3.2 were also produced, but excluded from Figure 3.2 for clarity of presentation. Note that each of these samples has a

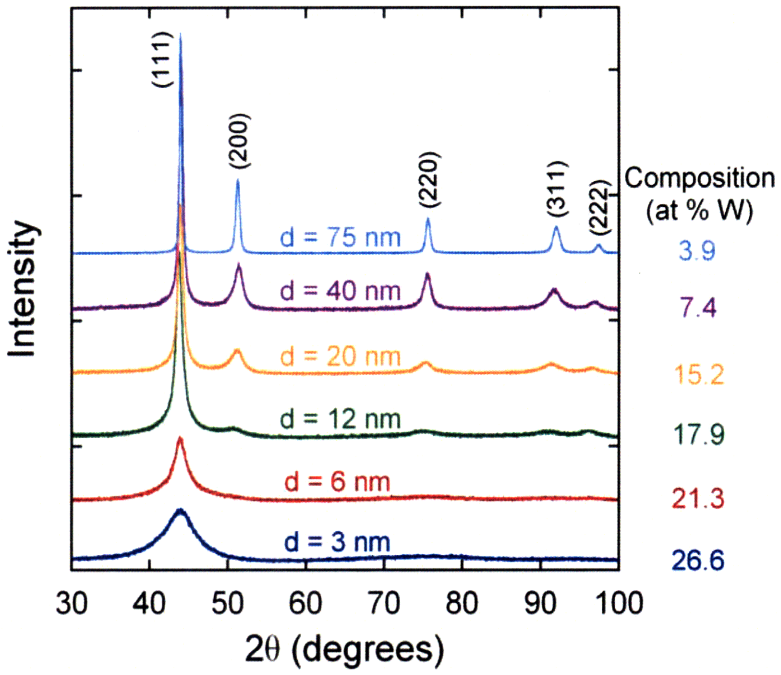

Figure 3.2: X-ray diffraction spectra and corresponding grain sizes for the as-deposited nanocrystalline Ni-W alloys. All the specimens are single-phase FCC solid solutions, and the respective alloy compositions are indicated.

different W content, cataloged on the right of each respective XRD spectrum, which manifests as a slight shift of the peaks towards lower Bragg angles, consistent with a swelling of the FCC lattice at higher W levels. All the identifiable peaks can be indexed with single-phase FCC reflections, indicating that every specimen is indeed a single-phase solid solution. Corroborating bright field transmission electron micrographs are shown in Figure 3.3 for select nanocrystalline specimens; electron diffraction patterns are included for reference. The grain sizes observed through TEM are in good agreement with those calculated from the measured peak broadening in XRD spectra. Lattice fringes associated with three distinct grains are also identified in the high resolution image in Figure 3.3(d).

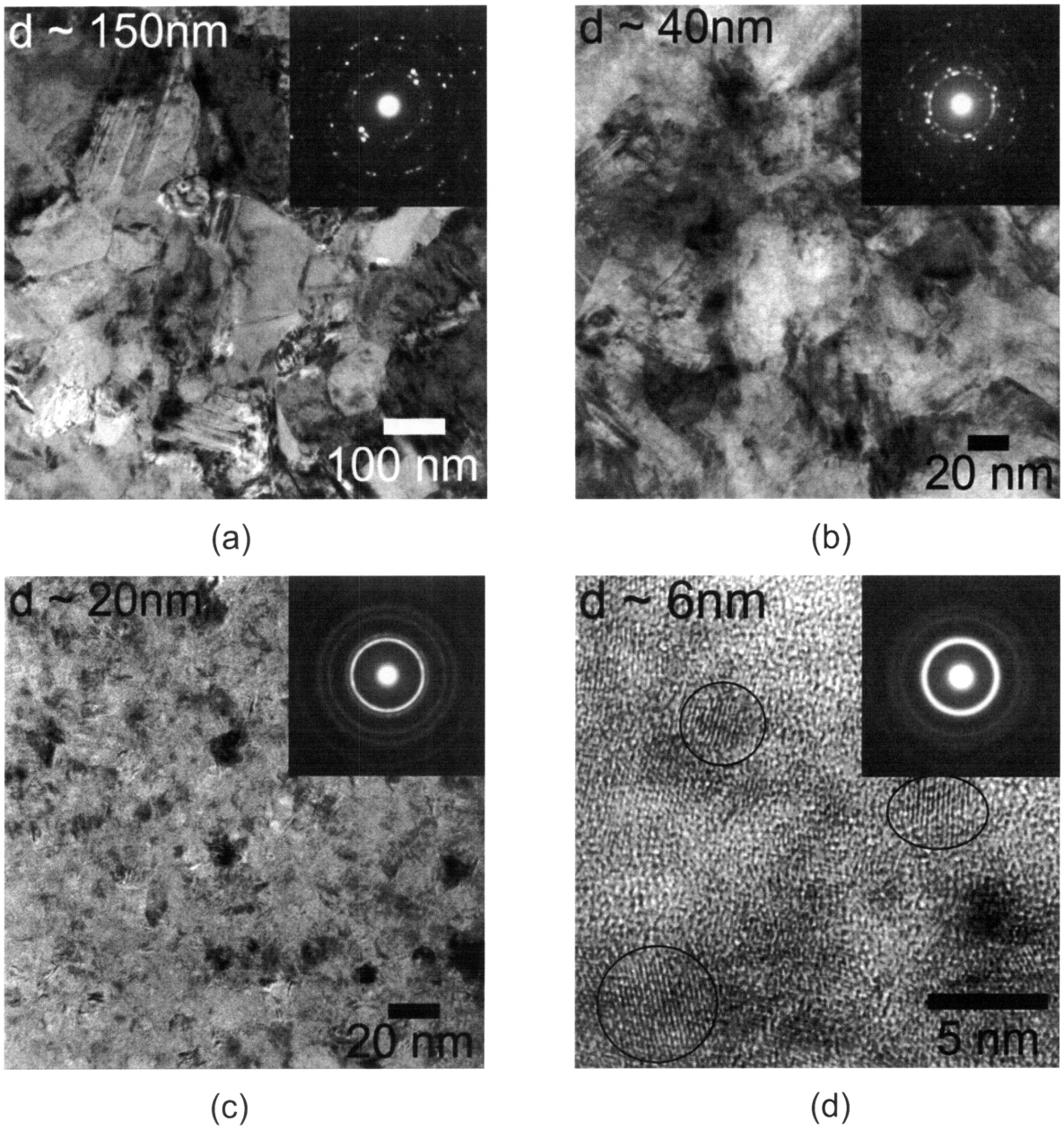

Figure 3.3: Bright field TEM images and selected area diffraction patterns for representative specimens. Panels (a)-(d) correspond to grain sizes of approximately 150, 40, 20, and 6 nm, respectively. In (d), a high resolution TEM image with lattice fringes is shown, and three discernible grains are circled for reference.

For the purposes of the ambient temperature mechanical testing, the alloying effect described above leads to an important caveat: whereas many investigators have studied the mechanical behavior of pure nanocrystalline metals, the following work specifically focuses on a more complex solid solution. In addition to the grain size contribution, there will certainly be effects

from alloying on the deformation mechanisms, but the two contributions are inextricably intertwined. Care must therefore be exercised in comparing the ambient temperature testing results with data for pure nanocrystalline metals, which occupy a distinctly different thermodynamic state from the present alloys. However, the thermodynamic instability of pure nanocrystalline metals, as discussed in Chapter 1, has hampered experimental progress in this area for more than a decade by rendering their synthesis difficult and encouraging grain growth during sample preparation or even during testing [229-240]. As shown in Chapter 2, segregating binary alloy systems with a moderate heat of mixing allow access to the full range of nanocrystalline grain sizes, and are stable over long periods of time even at elevated temperatures. This allows us to produce specimens with stable grain sizes across the entire Hall-Petch breakdown regime for a thorough and systematic study of mechanical behavior. A more detailed discussion of the effect of W additions on the Hall-Petch breakdown is discussed in Appendix B, with specific emphasis on the connection to the deformation mechanisms.

3.4 Isothermal annealing of Ni-W alloys

For Ni-W alloys, Detor and Schuh [133] have shown that the grain boundary relaxation process discussed in Section 1.2 initiates at temperatures as low as 100 °C, and proceeds up to temperatures of >300 °C, before the onset of grain growth, short-range ordering, or precipitation of a Ni_4W intermetallic phase. Specimens employed in elevated temperature indentation experiments must therefore first be subjected to low homologous temperature heat treatments, and mechanically characterized at ambient temperatures. Table 3.3 summarizes the as-deposited grain sizes, heat treatments (performed in an inert Ar atmosphere), and grain sizes subsequent to annealing for specimens used to study the influence of grain boundary state on the mechanical properties; specimens selected for elevated temperature nanoindentation testing are also indicated. Note that only the larger grain size samples exhibited slight grain growth outside of the measurement error, which is suggested in the XRD spectra shown in Figure 3.4 by the sharpening of the (111) and (220) peaks. The as-deposited and annealed spectra for the two finest grain size specimens are essentially unaffected by the heat treatments, and the grain size remains constant at d = 6 and 12 nm.

Table 3.3: Summary of the isothermal heat treatments used to study the effect of grain boundary state in Chapter 6. Heat treated grain sizes are included, and specimens used for elevated temperature indentation testing are indicated.

As-deposited Grain Size (nm)	Annealing Temp. (°C)	Annealing Time (hrs)	Heat Treated Grain Size (nm)	Elevated Temp. Indentation
70	150	24	73	
	300	24	80	X
18	150	24	18	
	300	24	20	X
10	150	24	10	
	300	24	10	
6	150	24	6	
	300	24	6	
3	150	24	3	
	300	24	3	X

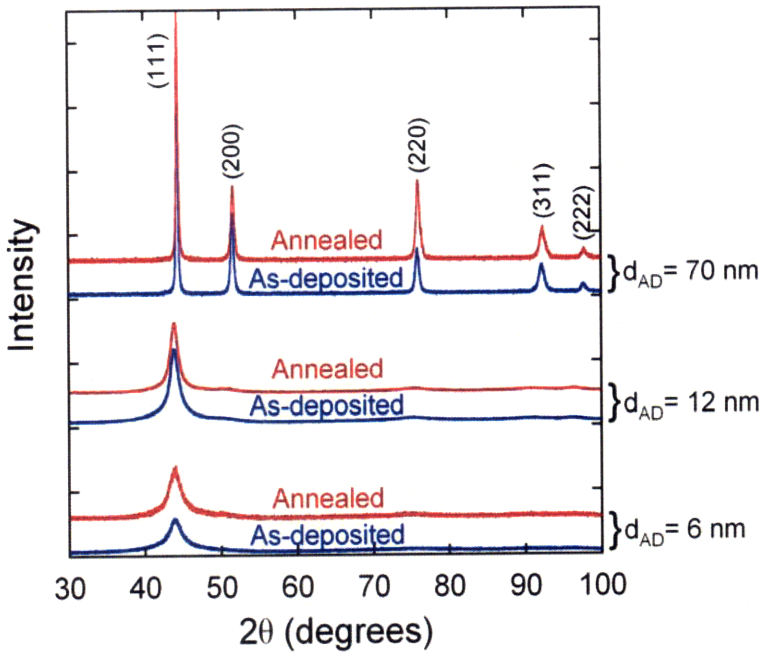

Figure 3.4: XRD spectra for three grain size specimens in the as-deposited state, and following a 300 °C anneal for 24 hours. While the as-deposited and annealed spectra are observed to be consistent for the finest nanocrystalline specimens, the d = 70 nm diffraction peaks are subtly sharper in the annealed condition, indicating grain growth.

3.5 Concluding remarks

Aqueous electrodeposition was used to synthesize high quality, fully dense nanocrystalline Ni-W alloys with grain sizes spanning the entire nanocrystalline regime, ideal for a systematic study of the Hall-Petch breakdown. Grain size was tailored by precise control over the alloy composition, as manipulated by a variety of deposition conditions such as the reverse pulse current density and bath temperature. These materials are used in ambient temperature nanoindentation testing at both quasi-static and dynamic strain rates (cf. Chapters 4 and 5, respectively). Selected as-deposited samples were also subjected to isothermal heat treatments to vary the grain boundary state, and their mechanical behavior at ambient and elevated temperatures is the subject of Chapter 6.

Chapter 4: Mechanical behavior of as-deposited nanocrystalline Ni-W alloys

In this chapter, we will explore the ambient temperature mechanical behavior of the as-deposited Ni-W alloys across the Hall-Petch breakdown regime at quasi-static strain rates, with specific interest in property scaling and its implications for the underlying deformation mechanisms. Because the properties of amorphous metals are so distinctly different from those of polycrystalline metals, there are several dramatic changes that must occur through the breakdown regime. In particular, we predict the following critical inflections in the mechanical behavior of nanocrystalline metals as the grain size is reduced to the amorphous limit:

- The heterogeneity of polycrystals tends to naturally distribute plasticity over many grains and/or grain boundaries, whereas in amorphous metals there is no intrinsic microstructural barrier to severe plastic strain localization. We expect that as the characteristic scale of the microstructure approaches the amorphous limit, the near-atomic-scale (non-adiabatic) shear banding process well known in metallic glasses [104, 106, 109] must emerge. This should be observed as a transition from homogeneous to localized flow at the finest nanocrystalline grain sizes.
- Whereas polycrystalline metals show an increasing strain rate sensitivity as grain size is refined [46, 61], amorphous metals are virtually rate-independent over many decades of strain rate [107]. Consequently, there must be a maximum in rate sensitivity at a finite grain size, corresponding to the shift from polycrystal-like to glass-like deformation mechanisms.
- Microcrystalline FCC metals are usually pressure-insensitive von Mises solids, while amorphous metals are known to be pressure or normal-stress sensitive [64, 65]. Accompanying a reduction of grain size into the nanocrystalline regime is an enhancement of the pressure sensitivity, which should ultimately converge upon that of an amorphous metal. Moreover, as noted by Lund et al. [63], adding microstructural constraints in the form of nanocrystalline grains should actually lead to a further increase in pressure sensitivity near the amorphous limit. Consequently, a maximum must also arise in the pressure dependence of deformation at a finite grain size.

Our purpose in this chapter is to experimentally validate these three predictions by systematically studying the entire Hall-Petch breakdown regime. We explore the homogeneous vs. localized nature of flow, the rate sensitivity, and the pressure sensitivity of nanocrystalline alloys with grain sizes ranging from ~150 to ~3 nm, and provide convincing evidence for a mechanistic shift from polycrystal-like to glass-like deformation. The work in this chapter has been published in Ref. [241].

4.1 Instrumented nanoindentation procedures

We shall make extensive use of instrumented indentation techniques, an approach chosen for several key reasons. First, only small volumes of test material are required for nanoindentation, allowing substantial redundancy in testing and statistically significant results. Second, indentation strain rate can be varied over at least four orders of magnitude, allowing us to quantitatively assess the rate dependence of strength. Third, indentations made with different sharp indenter geometries lead to different stress states, allowing a quick but robust estimation of the strength asymmetry.

The indentation experiments were conducted with a Hysitron Ubi1 indenter on specimens prepared with standard metallographic techniques to a roughness of < 10 nm. Most of our experiments employed a maximum load of 10 mN, corresponding to depths in the range of 200-250 nm, depending on the sample being tested. The standard Oliver-Pharr method [242] was applied to extract the hardness from the unloading part of the load-displacement response. For the hardness measurements, a diamond Berkovich tip was employed and the area function was carefully calibrated on fused silica. A minimum of 30 indentation curves were used to calculate each of the reported hardness values. In some cases which will be described in more detail later, a cube corner diamond tip was used instead of the Berkovich geometry. All of the tests were performed at a constant indentation strain rate, $\dot{\varepsilon}$, given by:

$$\dot{\varepsilon} = \frac{1}{h}\frac{\partial h}{\partial t} \tag{4.1}$$

where h is the indentation depth and t is time. Constant strain rate requires the loading rate divided by the load, $\dot{P}/P$, be held constant [243]; this profile was applied during the loading sequence, followed by linear unloading to 20% of the maximum load, where a 10 s hold was used to characterize the instrumental drift.

4.2 Hardness and flow behavior of nanocrystalline Ni-W alloys

The measured hardness values are compiled in Figure 4.1 as a function of grain size on double-logarithmic scales. The hardness error bars on these data are on the order of the data point size, and therefore cannot be seen; the trends in the data are significantly larger than the uncertainty.

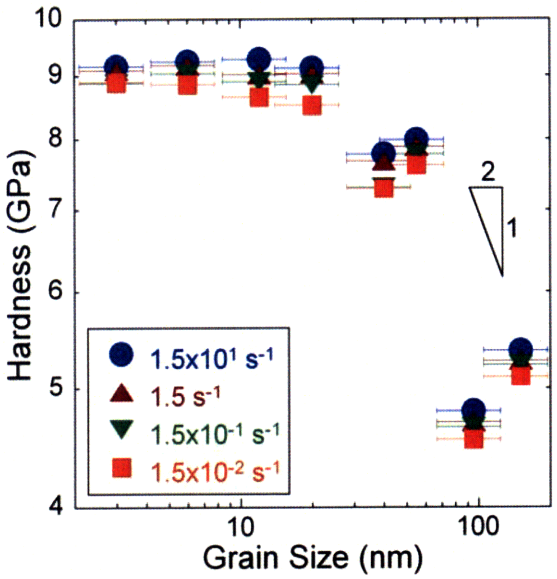

Figure 4.1: Hardness as a function of grain size on double logarithmic scales. Classical Hall-Petch strengthening is observed with grain size refinement down to about ~20 nm, followed by an apparent breakdown regime.

At large grain sizes (i.e. d ≥ 20 nm), the data exhibit a steep grain size dependence consistent with classical Hall-Petch strength scaling; the slope in this region of Figure 4.1 is close to the expected value of -½. However, at grain sizes below about 20 nm, all of the data series show a marked departure from this trend, exhibiting a plateau breakdown regime, or even a slight tendency toward weakening at finer grain sizes. These results are in line with existing

experimental and simulation data in nanocrystalline metals [10, 11, 77, 81, 88, 90], where the Hall-Petch breakdown is consistently observed in the range of d = 10-20 nm.

An interesting aspect of the present data set is that the finest grain sizes tested are quite close to the amorphous limit; the smallest grain size is d = 3 ± 1 nm, extremely close to the 1-2 nm value often assigned to the amorphous state [63, 74]. At ambient temperature, the plastic flow of amorphous metals is inhomogeneous, occurring through a series of shear banding events [104-106, 110, 111, 244], as discussed in Chapter 1. Such inhomogeneous flow has been widely studied by nanoindentation, where it is reflected by the appearance of shear offsets around the residual impression site [245], and often as discrete displacement bursts in the load-displacement response [109]. Both of these signatures of shear banding behavior are more readily observed when a sharper indenter geometry is employed. Consequently, we use the cube corner tip in the following set of experiments to look for signatures of inhomogeneous flow at the finest nanocrystalline grain sizes.

Arrays of indentations were performed on each sample using the procedures outlined in Section 4.1, and the residual impression sites were subsequently imaged with SEM in a FEI/Phillips FEG ESEM operating at 10 kV in high vacuum mode. A variety of indentation strain rates were used, but no trends with rate were discernible in any of the micrographs for the grain sizes studied; in the following, we therefore present results for one rate, 1.5×10^{-1} s^{-1}. Figure 4.2 compiles typical images of residual impression sites as a function of grain size. Referring first to the d = 20 nm sample shown in Figure 4.2(a), the pile up surrounding the residual impression site is smooth and homogeneous, as is characteristic for polycrystals or other materials deforming via conventional homogeneous plasticity. The 12 and 6 nm grain size specimens exhibit similar impression sites, as shown in Figure 4.2 (b, c), although the character of the piled up material is less smooth in these specimens, with small ledges becoming visible. As observed in Figure 4.2(d), the pile up nature around the residual impression site for the d = 3 nm sample is inhomogeneous and dominated by shear offset steps. These steps are traces of shear bands that are characteristic of unstable plastic flow. As noted in the opening comments of this section, such mechanical instabilities are indeed expected at the finest nanocrystalline grain sizes by analogy with shear

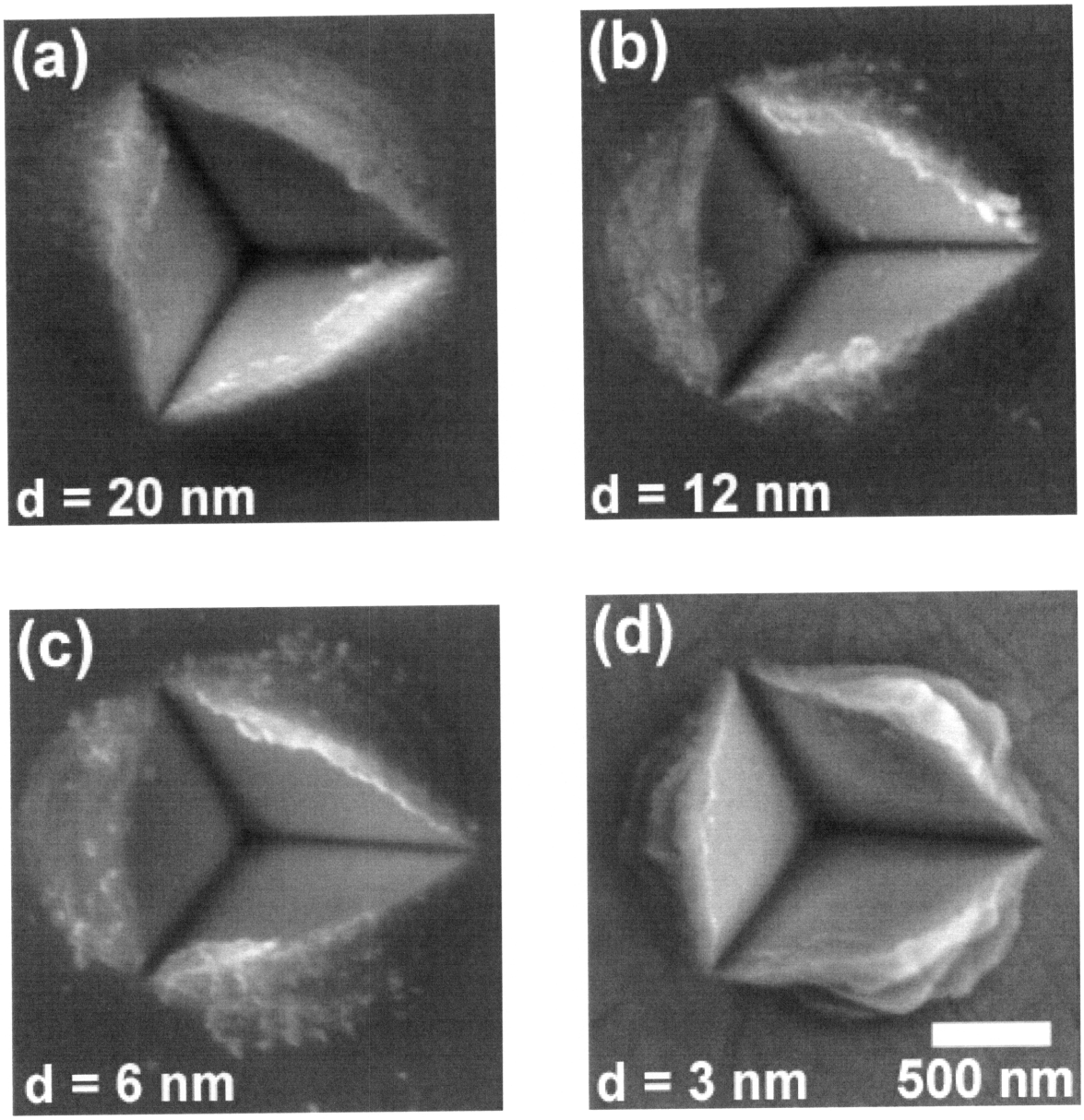

Figure 4.2: SEM images of residual impressions on Ni-W alloy specimens with a grain size of (a) 20 nm, (b) 12 nm, (c) 6 nm, and (d) 3 nm. A cube corner indenter geometry was used in testing and all the images were taken at the same magnification. Note the shear offsets in the pile-up of the d = 3 nm sample shown in (d).

banding in amorphous metals, and further predicted in recent modeling efforts [112-114] at the finest grain sizes, where the grain boundary volume fraction becomes the dominant structural feature []. The observations in Figure 4.2 mark a transition to inhomogeneous flow beyond the Hall-Petch breakdown, near the amorphous limit.

The change in deformation behavior implied by the post-indentation SEM images in Figure 4.2 is also manifested in the load-displacement responses. Three representative indentation curves are presented in Figure 4.3(a) for grain sizes of 3, 6, and 12 nm; for clarity, the curves are offset from one another along the x-axis. While the curves are observed to be smooth and continuous

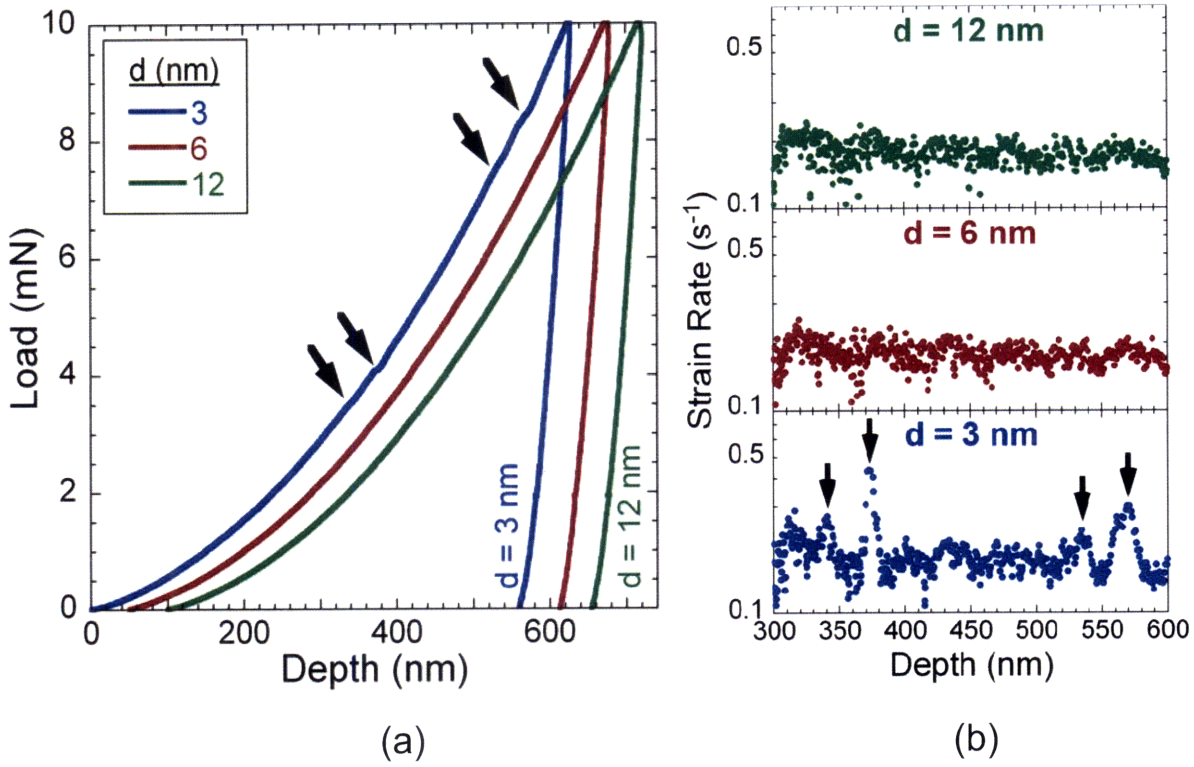

Figure 4.3: (a) Typical load-displacement responses for the finest grain size specimens resulting from indentation with a cube corner indenter at a strain rate of 0.15 s^{-1}. As identified by the series of arrows, discrete ripples or discontinuities are evident in the d = 3 nm data, while the d = 6 and 12 nm curves (offset for clarity by 50 and 100 nm on the depth axis, respectively) are smooth and continuous. (b) Strain rate plotted as a function of depth for the data shown in (a). Several prominent peaks occur in the d = 3 nm data that correlate exactly to the discontinuities identified in the load-displacement response from (a).

for d = 6 and 12 nm, small discontinuities or ripples can be seen in the load-displacement response for the d = 3 nm specimen. We find that these events correspond to periods of rapid travel of the indenter tip. Figure 4.3 (b) plots the strain rate as a function of depth for the three grain sizes represented in Figure 4.3 (a). A nominal indentation strain rate of 1.5 x 10^{-1} s^{-1} was

used in each of these tests, and the data in Figure 4.3(b) are correspondingly distributed around this mean value. For the 6 and 12 nm grain size specimens, strain rate is constant with indentation depth and the minor fluctuations or scatter in the data are measurement noise. While background scatter of a similar magnitude is also detected in the d = 3 nm data, in this case several pronounced peaks are evident, as indicated by the series of arrows in Figure 4.3 (b). These peaks lie convincingly above the experimental noise and correlate exactly to the positions of the discontinuities identified in Figure 4.3 (a) (the arrows denote the same four events in both frames of Figure 4.3). These events are of a similar character to those observed when indenting some amorphous metals [109], and we conclude that their presence is a signature of shear banding. The fact that the displacement bursts appear in the indentation response at the same grain size where we first observe shear offsets around residual impression sites is further support for this interpretation. The evidence in Figure 4.2 and Figure 4.3 is thus self-consistent, and suggests that there is indeed a transition to glass-like deformation behavior (i.e., shear localization) at the finest grain sizes below the Hall-Petch breakdown.

4.3 Rate sensitivity of deformation

To evaluate the rate sensitivity of deformation over the entire nanocrystalline regime, hardness measurements were performed in the same manner as discussed in Section 4.2, but now explicitly investigated as a function of strain rate. The fact that hardness is rate dependent can be seen directly in the raw indentation data, as shown in Figure 4.4(a) for a 20 nm grain size specimen at three different applied rates. For a constant applied maximum load of 10 mN, we see a subtle but reproducible variation in the contact depth with strain rate, as indicated by the shift in the load-displacement response. In particular, lower depths are attained for higher applied rates, indicating that hardness increases with increasing rate. Indentation rate effects of a similar magnitude have been observed in the load-displacement curves of other nanocrystalline metals [246]. A summary of our hardness measurements at various rates is given in the Hall-Petch plot of Figure 4.1.

To extract explicit hardness-rate trends, a series of seven indentation strain rates in the range of 1.5×10^{-2} to 15 s^{-1} was investigated for each of the eight grain size specimens. The results are shown in Figure 4.4 (b), where for clarity, only four representative grain sizes are presented. In

each case, hardness is found to increase with strain rate to within uncertainty. What is more, there is a reproducible grain size dependence in these trends; from d = 95 to 12 nm, the slope of the data series in Figure 4.4 (b) increases. However, further reduction in grain size to d = 3 nm is accompanied by a decrease in the slope of the hardness-rate trend. This grain size-dependent rate effect is also noticeable (but in a subtle way) on the Hall-Petch plot of Figure 4.1; here, a maximum can be seen in the rate-induced spreading of the hardness measurements around d = 12 nm. These observations represent the first suggestion that the rate dependence of strength undergoes an inflection at a finite grain size.

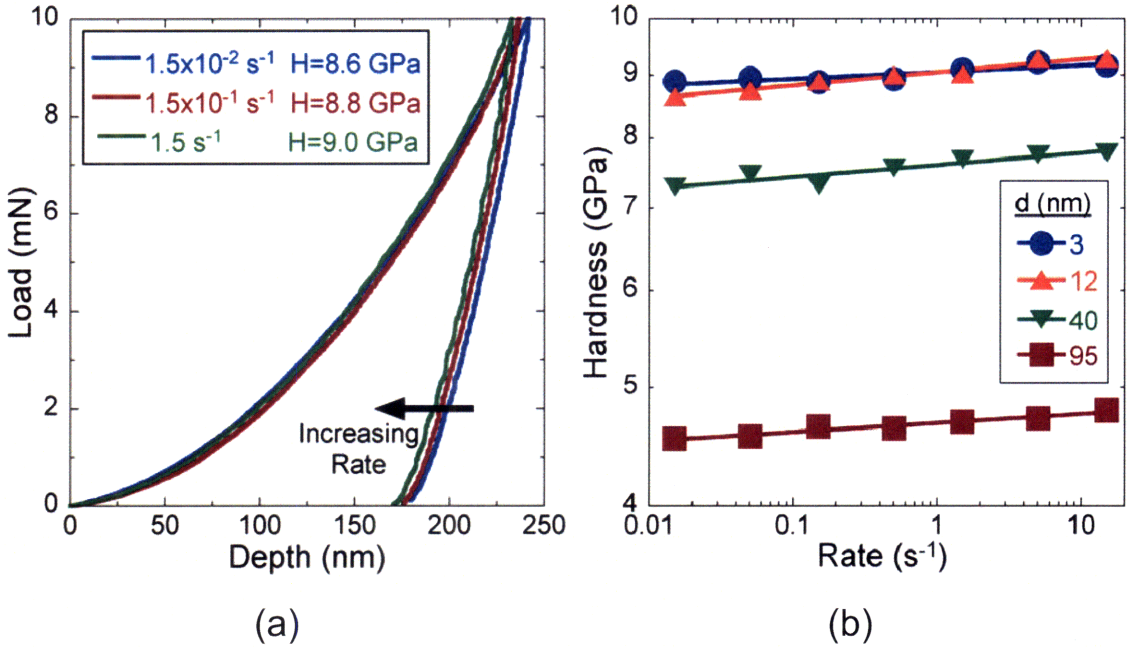

Figure 4.4: (a) Typical load-displacement curves for nanoindentation of a d = 20 nm grain size specimen at three strain rates. The curves shift to lower contact depths with increasing strain rate, corresponding to higher hardness values. (b) Hardness compiled as a function of strain rate for four representative grain size specimens; error bars are smaller than the data points in this figure.

Applying the relation for activation volume given by Eq. (1.2) to our data for nanocrystalline alloys, we obtain the plot shown in Figure 4.5, which catalogs V as a function of grain size. Here, the activation volume is normalized by the cubed Burger's vector (b^3) to facilitate comparison with the literature. As discussed in Section 4.2, at least 30 individual hardness measurements contribute to each reported H value, and because the hardness-rate trends in

Figure 4.4 (b) were each determined from tests conducted at seven different strain rates, a minimum of 210 independent indentation experiments were used to obtain each reported value of apparent activation volume. The error bars on V in Figure 4.5 reflect the full uncertainty on the raw hardness data, the linear regression procedure used to determine $\partial \ln \dot{\varepsilon} / \partial H$, and the variability in b^3 due to solid solution effects of W.

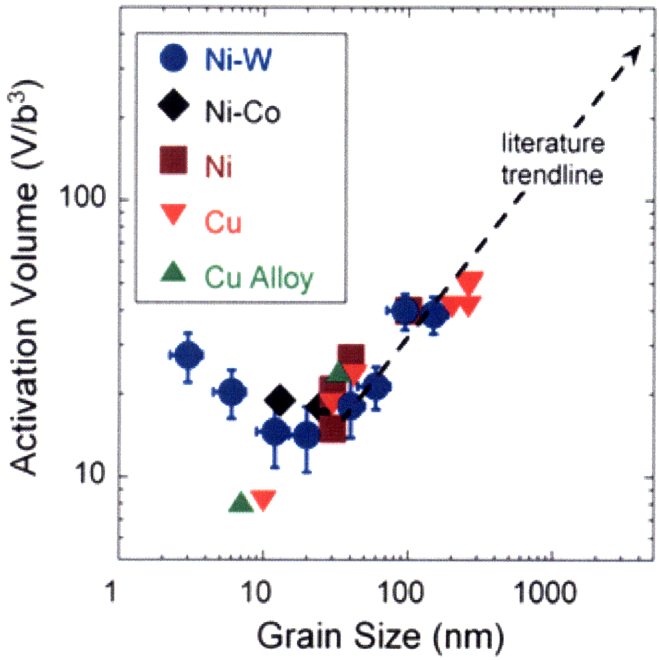

Figure 4.5: Activation volume for deformation of nanocrystalline Ni-W alloys, along with literature data for Ni [10, 47, 54], Ni-Co [53], Cu [46, 48-51, 53], and Cu alloy [49] systems. The activation volume is normalized by the cubed Burger's vector, b^3, and the present data reveal an inflection near a grain size of 10-20 nm.

For large grain sizes in Figure 4.5 (d > 20 nm), our data is in excellent agreement with the available literature data for V from various nanocrystalline materials [10, 46, 47, 49-53, 62, 247]; these literature data are shown in the range of grain sizes covered in Figure 4.5, and although not observed due to the truncation of grain size at 5 μm, additional literature results at grain sizes larger than 5 μm are also used to establish the included trendline. Like the prior work in this area, our data suggest that finer grain sizes have lower apparent activation volumes, at least for d ≥ 20nm. However, we also see that at a finite grain size around 10 nm, a clear minimum exists in the apparent activation volume, corresponding to a maximum in rate dependence. At grain

sizes below this critical value, the activation volume increases with decreasing grain size, corresponding to a drop in the rate sensitivity. To our knowledge, this transition has never before been observed or predicted, but it is an expected response based on the arguments presented in the introduction. A transition to glass-like inhomogeneous flow (or shear banding) at the finest nanocrystalline grain sizes should be accompanied by a divergence of V to very high values. The inflection in rate sensitivity across the Hall-Petch breakdown regime thus connects the known elevated rate dependence of nanocrystalline metals with the rate-independent strength of amorphous solids.

4.4 Pressure sensitivity of deformation

The pressure or normal-stress dependence of deformation is commonly quantified by measuring strength asymmetry via multiaxial mechanical tests [248-250], or by, e.g., comparing tensile and compressive yield strengths [55, 56, 58, 59]. Alternatively, a recent paper by Ganneau et al. [251] shows how indentation data can be used to assess the pressure or normal-stress sensitivity of cohesive-frictional materials. During indentation, the imposed state of stress will depend on the tip geometry employed. Using finite element calculations, Ganneau et al. showed how to determine the hardness-to-cohesion ratio (H/c) as a function of both the indenter geometry (i.e. apex angle) and the material's characteristic friction angle (φ), a measure of normal-stress sensitivity. As discussed in reference to Eq. (1.3), a more commonly cited measure of normal-stress sensitivity is the classical Mohr-Coulomb coefficient, α, which is directly related to φ:

$$\alpha = \tan\varphi \tag{4.2}$$

If two different indenter tips of known geometries are employed, their hardness ratio (H_1/H_2) is therefore a function of α, as shown in Figure 4.6 after Ref. [251], and take the form of a power series for both the Berkovich (H_B) and cube corner (H_{CC}) geometries. Because the former leads to a considerably higher confining pressure in the contact zone as compared with the sharper cube-corner, a pressure-dependent material will have a value of H_B/H_{CC} greater than unity, from which the friction angle, φ, can be extracted.

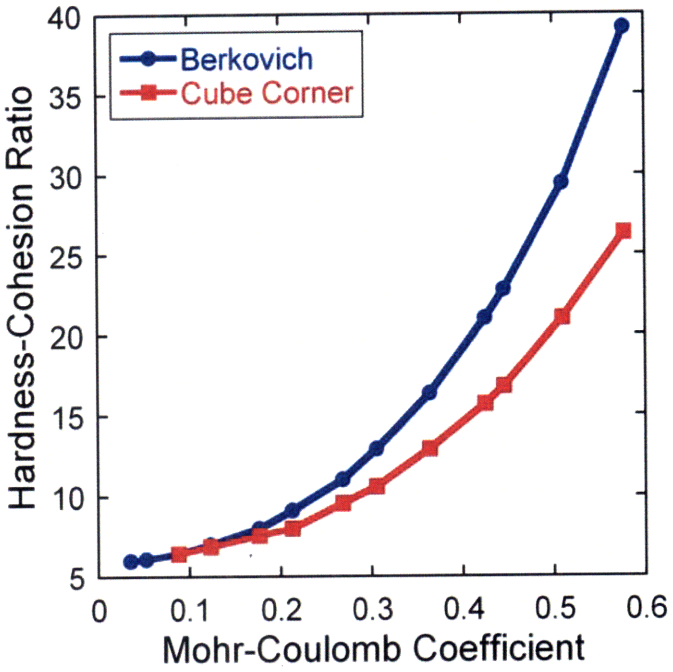

Figure 4.6: Hardness-cohesion ratio as a function of the Mohr-Coulomb coefficient for Berkovich and cube corner geometries, following Ref. [251]. The H/c ratios for the two geometries diverge as the pressure sensitivity increases (i.e. higher α), which results from the higher confining pressure imposed by the Berkovich tip relative to the cube corner.

Before applying the above procedure to estimate the pressure dependence of deformation in nanocrystalline Ni-W, there are two important caveats that must be addressed. First, the limit analysis implemented by Ganneau et al. [251] does not account for strain hardening in the calculation of the external work rate. However, because strain hardening is found to be negligible for nanocrystalline metals in general [54], and for Ni-W alloys in particular [78, 205], we expect that it is negligible as a source of error here. Second, for the experiments up to this point, we have measured the indentation contact area indirectly from an empirical area function based on a calibration using fused silica. While this is a suitable procedure for examining flow characteristics or rate sensitivity with a single indenter geometry, when trying to quantify the pressure dependence of deformation via a two-tip method, fused silica is no longer an appropriate calibration material due to its finite pressure sensitivity. The technique of Ganneau et al. relies on an unbiased assessment of the contact area, so in this section we resort to direct microscopic observations to measure the projected contact area and calculate hardness.

An array of indentations was performed on each specimen with each of the two tip geometries, using a 10 mN applied load and an indentation strain rate of 1.5 s^{-1}. The projected contact areas of 10 impressions from each array were measured with SEM. Figure 4.7(a, b) show typical micrographs of indentations in the d = 20 nm alloy made with (a) Berkovich and (b) cube corner geometry tips. The sharper indenter geometry (Figure 4.7(b)) produces greater pile-up and a noticeably larger projected contact area as compared with the more blunt Berkovich indenter (Figure 4.7(a)). Figure 4.7(c) compares the projections of these two impressions, making the difference in load-bearing area explicit. Because these indentations were performed with the same applied maximum load, Figure 4.7(a) corresponds to a higher hardness than does Figure 4.7(b). This hardness ratio, H_B/H_{CC}, is translated into a friction angle following the procedure of Ganneau et al. described above.

Figure 4.8 summarizes our measurements of the friction coefficient for nanocrystalline Ni-W alloys, presented along with a variety of existing literature data from other nanocrystalline metals. A representative value of $\alpha \sim 0.12$ is also shown at d = 1 nm for amorphous alloys [65]. Not only does our data agree with existing experimental results for nanocrystalline Ni, Zn, and Cu alloys (with d > 20 nm) [55-60], but the pressure sensitivity of our d = 3 nm specimen also aligns well with simulation results on nanocrystalline Ni of the same grain size [63]. More importantly, the current data set now populates the formerly unoccupied region spanning the Hall-Petch breakdown regime. The measured friction coefficients for samples with d = 6, 12, and 20 nm demonstrate a clear maximum in the vicinity of the Hall-Petch breakdown, and bridge the experimental results for d > 20 nm to the finite pressure-dependent strength of amorphous metals.

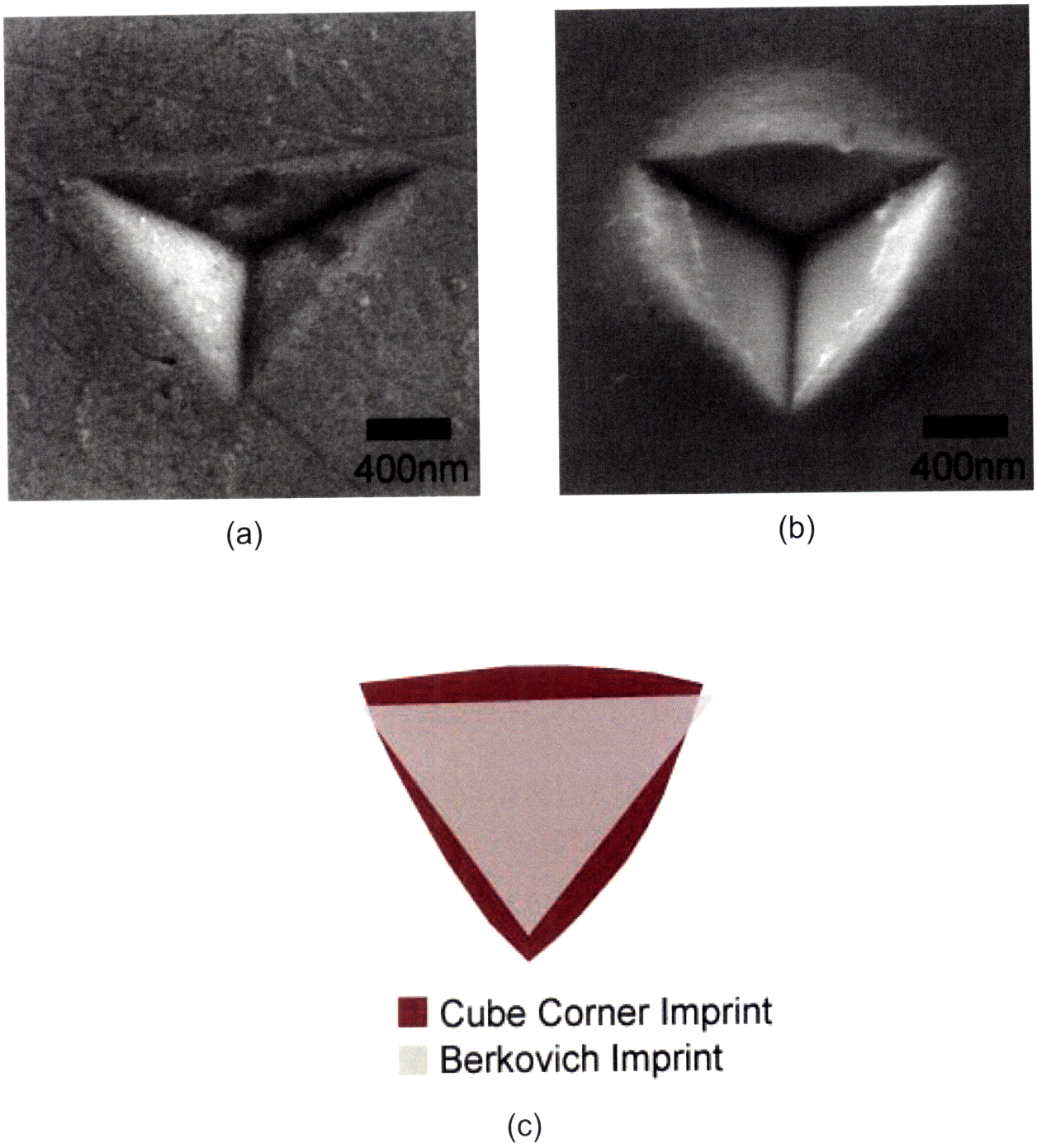

Figure 4.7: SEM images of indentations made with (a) a Berkovich and (b) a cube corner indenter geometry on a Ni-W alloy of 20 nm grain size. (c) Representation of the two imprints from (a) and (b) showing that the cube corner indenter requires a larger projected area to support the same applied load (10 mN).

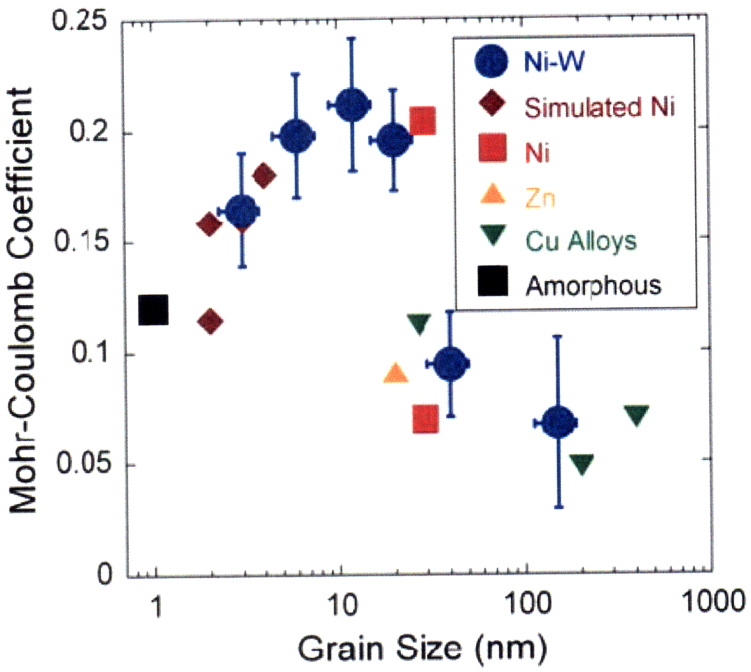

Figure 4.8: The Mohr-Coulomb friction coefficient, α, as a function of grain size. A maximum is observed for the present nanocrystalline Ni-W alloys at a grain size near 10-20 nm. Also shown are results from various literature data on Ni [57, 60] and Zn [58, 59], and Cu alloys [55, 56] which all lie to the right of the maximum, as well as simulation results on nanocrystalline Ni [63] that are exclusively to the left of the maximum. An approximate value of α typical of amorphous metals is also shown for reference at a grain size of 1 nm [65].

4.5 Implications

To summarize the findings presented above, the emergence of glass-like deformation behavior has been found to accompany the Hall-Petch breakdown in nanocrystalline Ni-W. In addition to changes in the strength scaling, we see a transition to inhomogeneous flow (shear banding) at small grain sizes, as supported by the observation of slip steps on deformed surfaces and displacement bursts in indentation curves. We have also observed how this mechanistic shift is manifested in several complementary mechanical properties. At a finite grain size around 15 nm, we report maxima in both the rate and pressure sensitivity of deformation. As described in the introduction, these inflections are required to bridge the mechanical property scaling of nanocrystalline metals with the limiting behavior of amorphous solids.

To our knowledge, multiple mechanical property inflections have never before been seen in a single set of experiments spanning the Hall-Petch breakdown regime. For example, the literature data shown for rate sensitivity in Figure 4.5 [10, 46, 47, 49-53, 62, 247] are collected from various sources representing a variety of different metals and alloys. They do not individually or collectively demonstrate the presence of a scaling breakdown. The present data align well with these literature results, but add a new, important inflection in the trend at finer grain sizes which connects to the rate-independent strength of amorphous metals. Similarly, the prior experimental data for pressure sensitivity in Figure 4.8 [55-60, 63, 65] are also collected from various sources, but do not demonstrate a maximum in pressure sensitivity because they are at grain sizes above the inflection point. When these data are supplemented by the simulation data of Lund et al. [63], the possibility of an inflection is suggested, but it is the present data set that offers the first convincing demonstration of a pronounced maximum in pressure sensitivity at a finite grain size.

These inflections shed new light on the nature of the Hall-Petch breakdown, and how it is observed in an experimental setting. In particular, it is interesting to see in Figure 4.1 that at low indentation strain rates, the breakdown appears as a smooth plateau in hardness as d decreases below ~20 nm, while at higher rates a subtle but discernible peak hardness emerges. It has been a standing question for some time whether the Hall-Petch breakdown is (or should be) accompanied by a true strength inflection, or merely an inflection in slope [4, 80]. We see now that deformation rate plays an important role here, with higher rates promoting the development of a peak in strength and a regime of so-called "inverse Hall-Petch" behavior. Clearly, this effect is a direct consequence of the inflection in rate dependence observed in Figure 4.5. This observation may help to unify experimental observations based on microindentation (at very low rates) with molecular simulation results (at very high rates). In such experiments the Hall-Petch breakdown is commonly observed as a plateau [4, 77], while in simulations a pronounced peak is observed [81, 90]. In fact, extrapolating our results to a common simulation strain rate of 10^8 s^{-1}, we expect a hardness peak at a grain size of ~12 nm more than 1 GPa above the value at the amorphous limit. This estimation lines up well with the strength peak observed in simulated nanocrystalline copper [81]. These observations also foreshadow the results of Chapter 5, in which we will explore the issue of rate dependence in more detail.

A further interesting aspect of the property inflections found here is that they all occur at the same grain size (to within the resolution of our experiments). Thus, d ~ 10-20 nm can be identified not only as "the strongest size" [84], but as the most rate- and pressure-sensitive size as well. This may have significant practical implications for applications where simultaneous optimization of all three properties is desirable. For example, in applications involving high rate deformation in general and shock loading in particular, additional strength increments can be expected to arise from both the high applied strain rates and the presence of a confining pressure wave (i.e. internal pressure due to limited lateral relaxation). Indeed, recent work by Bringa et al. [252] has shown that pressure-induced suppression of grain boundary-mediated plasticity does promote enhanced strength during shock loading of simulated nanocrystalline metals, and experimental work is underway to explore the consequences of such effects [10, 55, 253-258].

Finally, we propose that the present work may also offer a connection to the growing literature on amorphous-nanocrystalline composites, synthesized by partially devitrifying metallic glasses. If we assume that the grain boundaries in our specimens are essentially amorphous with a thickness of 1 nm, then our d = 3 and 6 nm samples may be viewed as amorphous-matrix composites containing ~30% 3 nm, and ~60% 6 nm crystal reinforcements, respectively. These structures may resemble some partially devitrified metallic glasses, which commonly contain ~2-50 nm nanocrystals with volume fractions up to 75% [259-263]. When such amorphous composites are subjected to deformation, marked changes are observed relative to fully amorphous specimens [259, 260, 262-264]. In general, the observations imply that larger nanocrystals of a higher number density may help distribute shear bands over a larger volume, apparently promoting homogeneous flow. Our results show substantial suppression of plastic instabilities as grain size changes from d = 3 to 6 nm, and are thus in line with such observations.

4.6 Concluding remarks

Various nanoindentation techniques have been applied to evaluate the mechanical behavior of nanocrystalline Ni-W alloys across the entire Hall-Petch breakdown regime. We find that grain boundary-induced strengthening of nanocrystalline Ni-W obeys the Hall-Petch relation down to at least d ~ 20 nm, followed by a breakdown regime and even apparent weakening. At the finest

grain sizes approaching the amorphous limit, this breakdown is accompanied by shear banding as commonly observed in metallic glasses, evidenced both by shear offsets around residual impression sites and discrete discontinuities in the indentation responses. Such results mark an explicit transition in the flow behavior, from homogeneous, polycrystal-like flow to unstable, localized plasticity characteristic of amorphous metals.

We have also shown that the Hall-Petch breakdown is accompanied by critical inflections in two additional mechanical properties:

- The apparent activation volume for deformation decreases (corresponding to an enhancement in rate sensitivity) as grain size is refined to d = 10-20 nm, where a subsequent minimum is realized. The increase in V with further grain size reduction connects the elevated rate sensitivity of nanocrystalline metals to the rate-independent strength of amorphous solids.
- The sensitivity of deformation to pressure or normal-stress, described by the Mohr-Coulomb friction coefficient, becomes more pronounced with grain size reduction, and peaks in the range of d = 10-20 nm. For grain sizes below d ~ 10 nm, the friction coefficient converges upon the finite value commonly used to describe the pressure sensitivity of amorphous metals.

These mutually consistent inflections in strength, rate sensitivity, and pressure sensitivity are all a direct consequence of the emergence of inhomogeneous flow at the finest nanocrystalline grain sizes. The Hall-Petch breakdown thus corresponds to a mechanistic shift to glass-like plasticity, bridging the deformation behavior of nanocrystalline and amorphous metals.

Chapter 5: The Hall-Petch breakdown at high strain rates

The experimental study of the Hall-Petch breakdown described in Chapter 4 demonstrated that the rate sensitivity of deformation maximizes at a grain size of about 10-20 nm, which results from the emergence of glass-like shear banding at finer grain sizes. This result suggests that the character of the Hall-Petch breakdown should in fact be rate dependent; low rates should favor a subtle shift in the Hall-Petch slope, somewhat higher rates should reflect an apparent plateau in strength, and at sufficiently high rates, a strength maximum and a weakening "inverse Hall-Petch" regime should be observed. Although there is increasing interest in the high-rate testing of nanocrystalline materials [10, 55, 253-258] as highlighted in Section 4.5, no experimental studies to date have explored the Hall-Petch breakdown regime systematically at high rates. Our purpose in this chapter is to present such a study, with specific emphasis on strength scaling under dynamic loading situations, and verify that the "inverse Hall-Petch" weakening regime emerges at high strain rates. The work in this chapter has been submitted to Applied Physics Letters and is currently under review [265].

5.1 Experimental procedures

High rate mechanical testing was performed using a Micro Materials Nanotest 600 configured for single impact dynamic hardness measurements. Following the procedure outlined in Refs. [266, 267], an indenter mounted to a pendulum is accelerated into the sample surface, and the displacement, h, is tracked during the impact and rebound of the tip. Specimens were prepared using standard metallographic techniques to achieve a surface roughness of < 10 nm, and each sample was subjected to 70 impact tests using a diamond Berkovich tip. The average dynamic hardness values are reported here, with error bars given by the standard deviation.

The raw displacement-time (h-t) data generated during impact of a 12 nm grain size specimen is shown over the full acquisition range in the upper panel of Figure 5.1(a), and the lower panel displays the corresponding velocity, calculated from the h-t data as a moving-average slope over seven data points. A transient region is initially observed for $t < 50$ ms, followed by

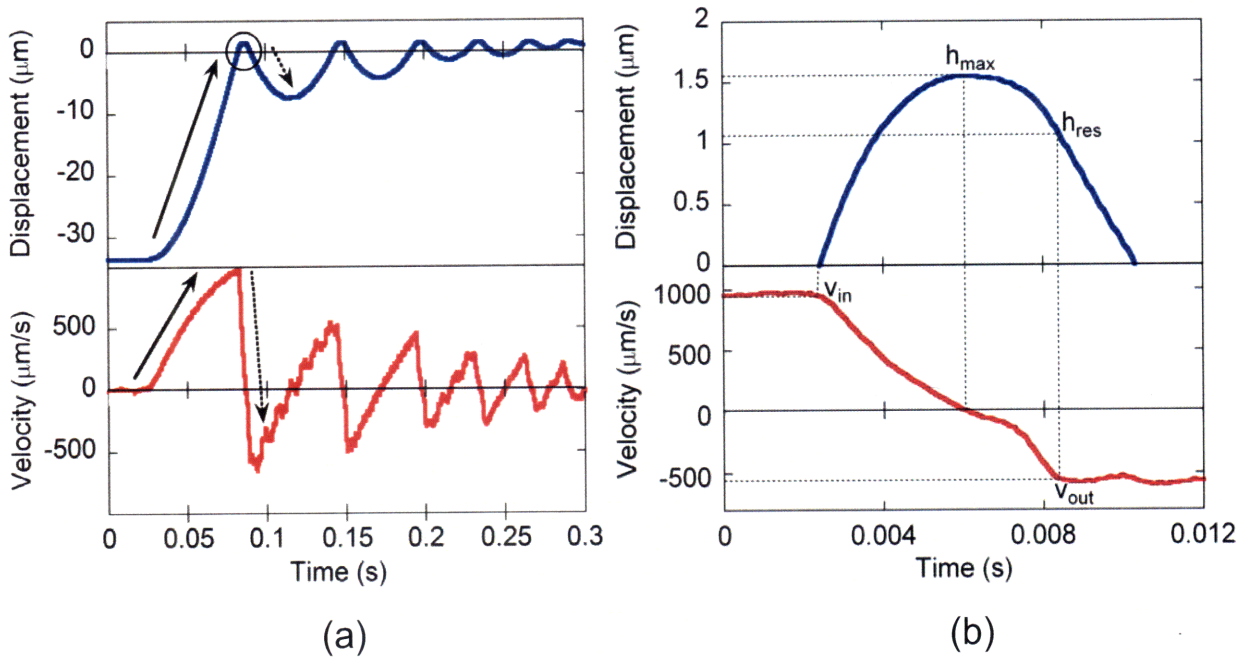

Figure 5.1: Representative raw data from an impact test on a 12 nm grain size Ni-W specimen, where the upper panels demonstrate the output displacement time data, from which the velocities, shown in the lower panels, are calculated. (a) Displacement and velocity over the full acquisition time, where the solid arrows denote initial acceleration of the tip, and the dotted arrows deceleration as the tip is driven into the specimen surface. The primary impact event circled in (a) is magnified in (b), where the critical displacements and corresponding velocities are highlighted. Note that the time scale has been arbitrarily assigned in (b).

acceleration of the indenter tip towards the sample surface, which is denoted by the solid arrows. The region of the curve associated with impact-induced deformation is circled, with a magnified view shown in the upper panel of Figure 5.1(b). The point of initial contact is identified by the onset of tip deceleration, as indicated by the dotted arrows, and is assigned as h = 0; the velocity at contact is denoted v_{in}. Although indentation strain rate is a function of depth, it can be roughly approximated as $\dot{\varepsilon} \approx v_{in} \cdot h_{max}^{-1}$, where h_{max} is the maximum penetration depth, and is of order ~1 μm in our experiments. With a typical initial contact velocity of ~1 mm·s^{-1}, this calculation yields a characteristic rate of about 10^3 s^{-1} for all of our tests, and we assign this value a liberal error bar of ±50%.

Two additional measurements are required to characterize the energy dissipated as plastic work, which include the residual plastic depth, h_{res}, and outgoing velocity, v_{out}, and are identified in Figure 5.1(b). Both of these quantities require inspection of the second impact event to determine the absolute displacement at the point at which the tip re-establishes contact with the surface. Figure 5.2 shows a magnified view of the first two impact and rebound events, truncated to the range $0.06 \leq t \leq 0.19$ s. Following the initial rebound, the indenter tip is

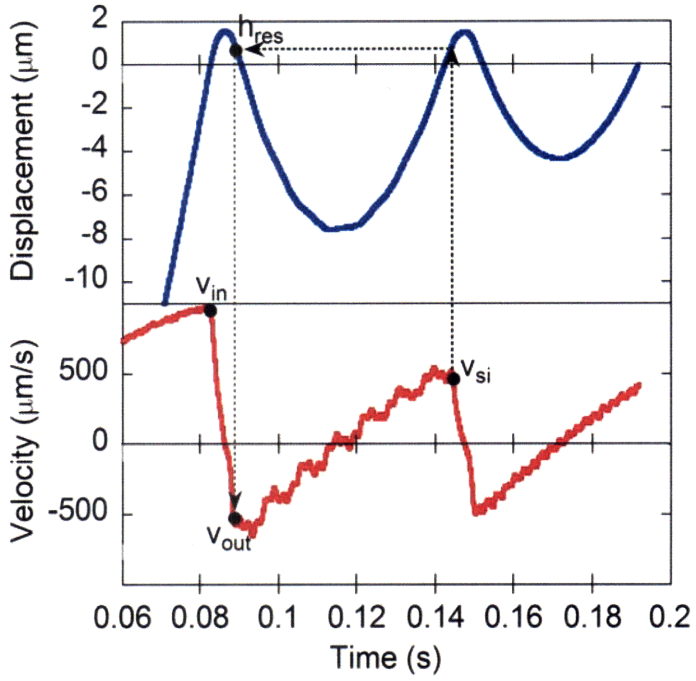

Figure 5.2: Magnified view of the first two impact events from Figure 5.1(a). Calculating h_{res} and v_{out} rely on accurately identifying the point of deceleration (denoted with velocity v_{si}) associated with the tip coming back into contact with the sample surface after the initial rebound event.

accelerated back towards the sample, and re-contacts the surface within the residual impression created by the preceding impact event. Upon re-establishing contact, the point of initial deceleration corresponding to v_{si} in Figure 5.2 defines the residual depth, and the corresponding point on the initial rebound curve is identified as h_{res}, with velocity v_{out}. These displacement and velocity measurements are extracted from every test with the use of the analysis script presented in Appendix C, and are used in the next section to calculate the dynamic hardness.

5.2 Dynamic hardness and the Hall-Petch breakdown at high strain rates

Equating the change in kinetic energy of the indenter to the plastic work done during impact gives:

$$\frac{1}{2}m\left(v_{in}^2 - v_{out}^2\right) = \int_0^{h_{res}} P dh \tag{5.1}$$

Here, m is the effective mass of the pendulum and tip (equal to 0.21 kg in this work) [267], v_{out} and h_{res} are the velocity and displacement upon exit of the tip from the sample surface (defined in Figure 5.1), respectively, and P is the indentation load. Hardness, H, is defined as the ratio of the load to projected contact area, A_c, where for a self-similar indenter geometry, $A_c = c \cdot h^2$ with the constant c = 24.5 for our Berkovich tip. Assuming that H is constant over the duration of the test, it can be substituted into Eq. (5.1) for P, yielding an effective dynamic hardness, H_d:

$$H_d = \frac{3m\left(v_{in}^2 - v_{out}^2\right)}{2ch_{res}^3} \tag{5.2}$$

H_d derives from the energy balance presented in Eq. (5.2), and quantifies the energy per unit volume dissipated as plastic work during impact-induced deformation.

The dynamic hardness measurements from the present Ni-W alloys are summarized in Figure 5.3. For comparison, the quasi-static nanoindentation data from a similar set of experimental materials are also shown, reproduced from Section 4.2. At large nanocrystalline grain sizes, the dynamic data are consistent with classical Hall-Petch scaling, and are in agreement with the quasi-static hardness measurements to within errors. As expected, we observe a clear divergence from Hall-Petch scaling in the vicinity of ~20 nm grain size in all of these data sets. However, whereas the quasi-static tests generally exhibit a trend more akin to a hardness plateau in the breakdown regime, the dynamic indentation tests show a discernible peak strength at a grain size of about 12 nm, followed by a regime of softening toward the amorphous limit. Because of the

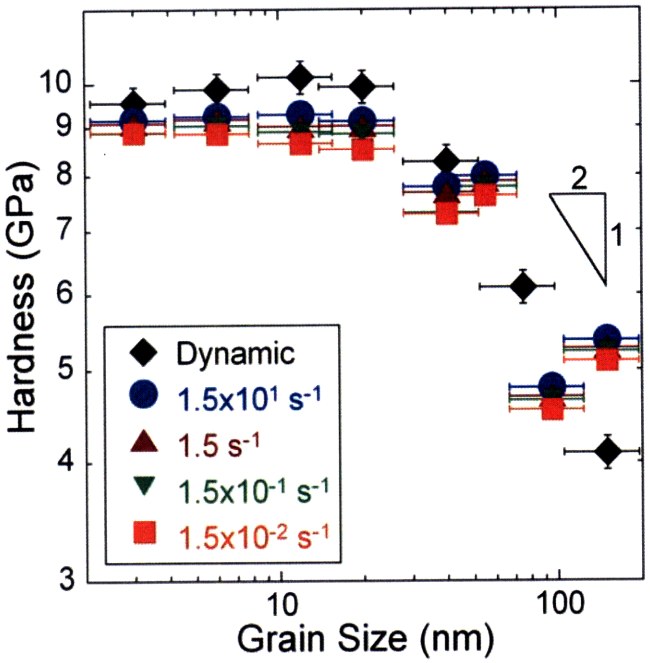

Figure 5.3: Dynamic hardness as a function of grain size on double logarithmic scales. Hall-Petch scaling is observed down to a grain size of ~20 nm, followed by a breakdown manifested as a strengthening peak and region of "inverse Hall-Petch" weakening. The quasi-static hardness measurements from Section 4.2 are included for reference.

large statistical samples used here (70 tests per data point in Fig. 3), we can have high confidence (>95% as determined through a Welch's t-test) that the peak we observe at high rates is statistically significant.

Further analysis shows that the emergence of the peak strength is related directly to a maximum in the rate sensitivity of deformation. This is seen most easily by plotting the data in the manner suggested by the constitutive law:

$$\dot{\varepsilon} = \dot{\varepsilon}_o \exp\left(\frac{V \cdot H}{3\sqrt{3} \cdot kT}\right) \tag{5.3}$$

where $\dot{\varepsilon}_o$ is a grain size-dependent pre-exponential constant, V is the activation volume, and kT has its usual meaning. Hardness-rate trends are plotted in Figure 5.4 for our specimens with d ≤

50 nm; the quasi-static results from Section 4.3 are included for reference, and are fitted with Eq. (5.3). When our new measurements of H_d are supplemented into Figure 5.4 at the approximate strain rate of 10^3 s^{-1}, they align well with the quasi-static data to within measurement and extrapolation errors. What is more, the activation volumes in Figure 5.4 first decrease and then increase as grain size traverses the Hall-Petch breakdown, reflecting the maximum in rate sensitivity at a grain size of ~10-20 nm. This maximum is responsible for accentuating the "inverse Hall-Petch" trend at sufficiently high rates, which further supports the connection proposed in Chapter 4 between quasi-static experimental results and high-rate atomistic simulations.

We observe in passing that an additional effect can manifest in high-rate impact tests on nanocrystalline metals, which relates to the influence of pressure on their strength. As discussed in Section 4.4, nanocrystalline metals exhibit a grain size-dependent pressure sensitivity that also maximizes in the vicinity of the Hall-Petch breakdown. In some high-rate loading situations, such as in shock loading, high confining pressures may induce an additional strength increment [252-254]. In the present experiments, we are using only a modest impact velocity (~1 $mm \cdot s^{-1}$), and derive a high rate by confining ourselves to small displacements (~1 μm). Therefore, the elastic pressure wave velocity is much greater than the impact velocity, and we expect no significant effect of confining pressure on the measured values of H_d. However, we note that more conventional impact situations involving higher velocities and larger length scales may well benefit from the finite pressure sensitivity of nanocrystalline metals in the Hall-Petch breakdown regime.

5.3 High strain rate flow behavior of nanocrystalline Ni-W alloys

A final interesting aspect of the high-rate response of our specimens is revealed by inspecting the plastic zones around the impact sites, which were imaged with SEM in the same manner as the impressions shown in Section 4.2; these are included in Figure 5.4 adjacent to the corresponding H-$\dot{\varepsilon}$ trends. First, we note that shear banding is conspicuously evident in the 3 nm grain size

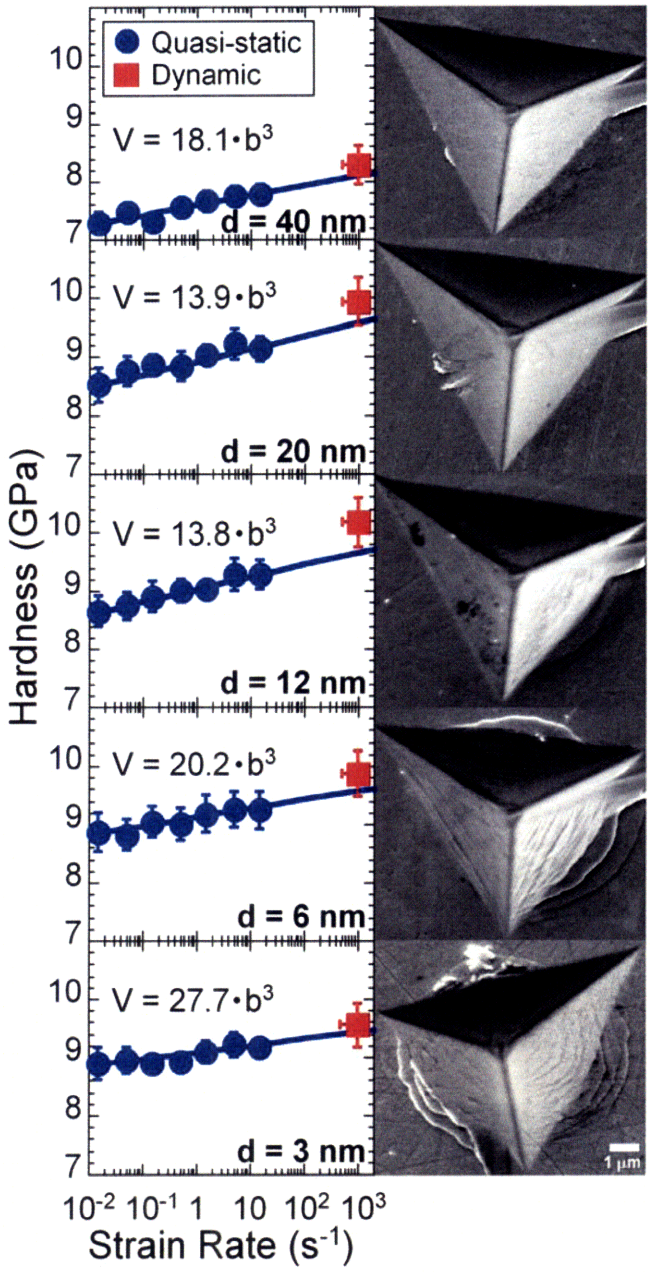

Figure 5.4: Hardness as a function of strain rate for specimens with grain sizes in the range $3 \leq d \leq 40$ nm. The dynamic measurements from the present work align well with the extrapolation from quasi-static nanoindentation results reproduced from Chapter 4. Corresponding SEM images of the residual impressions reveal discernible shear offsets around the impact sites for grain sizes as large as 12 nm. (Some of the impressions have a scar across them, made upon withdrawal of the tip; these scars are formed after the conclusion of the test and are not relevant to the discussion).

specimen. This is an expected result, since this grain size is very near the amorphous limit, and "structural" shear bands similar to those in metallic glasses form even under quasi-static conditions, as demonstrated in Section 4.2. What is more interesting at present is that at slightly larger grain sizes (e.g., 6 and 12 nm), shear offsets can also be identified around the impact sites. Under quasi-static loading, these materials do not exhibit such obvious signs of shear localization (cf. Figure 4.2), indicating that the high strain rate applied in this study increases the propensity for inhomogeneous flow. It is not clear if these are "structural" shear bands such as those in metallic glasses, or perhaps classical adiabatic shear bands that are promoted by the fine grain structure in these specimens. In either case, the residual impressions in Figure 5.4 strongly imply that nanocrystalline grain size influences the inclination for shear band formation at high strain rates, which has important implications for optimizing the nanostructure for impact applications.

5.4 Concluding remarks

To summarize, the breakdown of Hall-Petch strength scaling was investigated in nanocrystalline Ni-W alloys at high strain rates, using dynamic indentation testing at grain sizes ranging from 3 to 150 nm. Focusing on the first two impact events, the energy dissipated as plastic work has been calculated for each grain size specimen, from which the dynamic hardness is determined. Whereas the breakdown in Hall-Petch scaling may appear as a strength plateau at quasi-static strain rates on nanocrystalline Ni-W alloys, it involves a strengthening peak and "inverse Hall-Petch" weakening regime at higher strain rates. This effect was shown to be the result of a grain size-dependent rate sensitivity that exhibits a maximum at a grain size near 10-20 nm. Evidence of shear band formation was also observed around the impact sites on specimens with $d < 20$ nm, consistent with a transition to glass-like mechanisms at the finest grain sizes, but with an increased tendency for shear localization at high rates.

Chapter 6: Mechanical behavior of heat treated Ni-W alloys

The grain size-dependent activation volume presented in Chapter 4 was shown to have important implications for the nature of the Hall-Petch breakdown in Chapter 5, where the minimum activation volume, corresponding to a maximum in rate sensitivity, accentuates a strengthening peak across the breakdown regime. In addition to quantifying the rate sensitivity, the activation volume is a signature of the underlying deformation mechanisms, with the inflection in scaling signifying the onset of inhomogeneous flow at the finest nanocrystalline grain sizes. This is further understood through inspection of the constitutive law for thermally-activated plastic flow, which describes the shear strain rate under uniaxial tension, $\dot{\gamma}$, in terms of the Gibbs activation energy for deformation, ΔG [268]:

$$\dot{\gamma} = \dot{\gamma}_o \exp\left(\frac{\Delta G}{kT}\right) \tag{6.1}$$

where $\dot{\gamma}_o$ is a pre-exponential constant. We can identify the activation volume by expressing ΔG as a function of the effective stress, τ_e, and Helmholtz free energy for deformation, ΔF [47]:

$$\Delta G = \Delta F - \tau_e \cdot V \tag{6.2}$$

where the activation volume now explicitly represents the characteristic volume over which the effective stress acts to overcome the local barrier to deformation. For the present nanocrystalline alloys, the inflection in V therefore denotes a shift in the rate-controlling mechanism for deformation.

A number of studies [10, 41, 46-51, 53, 54, 61, 79, 268-272] have evaluated such activation quantities for nanocrystalline FCC metals in relation to their coarse grain counterparts, and have correlated smaller activation volumes with finer nanocrystalline grain sizes, as illustrated in Figure 1.2; subtle changes in the activation energies have also been demonstrated. While we

were able to quantify the grain size-dependence of the activation volume in Chapter 4 from room temperature mechanical tests, determination of the activation energy for deformation is a more complex task, requiring property measurements across multiple test temperatures. The present nanocrystalline Ni-W alloys are ideally suited for such a study due to their excellent thermal stability [135, 273], where grain growth is suppressed to temperatures > 400 °C. However, as discussed in Chapter 1, low homologous temperature annealing (< 400 °C) of nanocrystalline metals, and Ni-W alloys in particular [133, 135, 274], can lead to unexpected strengthening, often attributed to grain boundary relaxation.

In this chapter, we first investigate the strength scaling behavior of heat treated nanocrystalline Ni-W alloys using ambient temperature nanoindentation testing, with emphasis on the influence of thermally-induced structural relaxations. Following this, fully relaxed Ni-W specimens are subjected to elevated temperature indentation tests to characterize the temperature dependence of strength, and ultimately calculate the activation energy for deformation across the nanocrystalline regime.

6.1 The role of structural relaxation in nanoscale plasticity

Nanocrystalline Ni-W alloys were electrodeposited and annealed following the procedures in Chapter 3 to promote relaxation of the grain boundaries. The grain sizes investigated span the Hall-Petch breakdown, and only the largest nanocrystalline grain size of 70 nm exhibited slight grain growth at both annealing temperatures. The sample preparation and nanoindentation procedures are analogous to those presented in Section 4.1, where a minimum of 30 indentation curves are again used to calculate the average hardness and standard deviation at each of the seven indentation strain rates. By characterizing the rate dependence of strength, the activation volume for deformation can be calculated following the procedure described in Section 4.3.

Figure 6.1 shows the hardness-grain size trends for the as-deposited and annealed Ni-W specimens on double logarithmic scales; the hardness error bars on these data are on the order of the data point size. For an indentation strain rate of 1.5×10^{-1} s^{-1}, the hardness of the

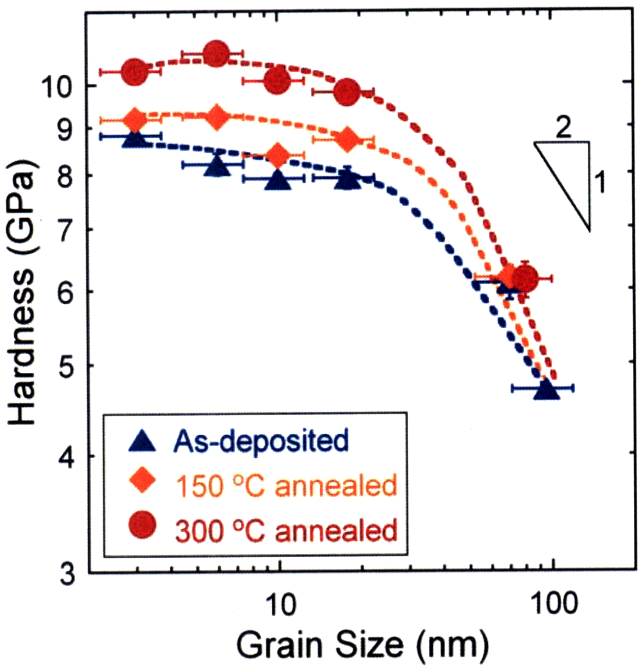

Figure 6.1: Hardness as a function of grain size on double logarithmic scales for as-deposited and relaxed Ni-W alloys at an indentation strain rate of 1.5 x 10^{-1} s^{-1}. The dashed trend lines are included for clarity, and shift to higher hardness values as the annealing temperature is increased, especially in the vicinity of the Hall-Petch breakdown.

as-deposited specimens imply Hall-Petch scaling at larger nanocrystalline grain sizes, and a breakdown regime below d ~ 20 nm. Upon annealing, the trends shift to higher hardness values, and the magnitude of this shift exhibits a grain size dependence. While the hardness of the largest nanocrystalline grain size specimen is unaffected by annealing, the observed strengthening increments increase with decreasing grain size in the Hall-Petch breakdown regime, down to about 6 nm. However, at a grain size of 3 nm, the observed hardening becomes less pronounced, thus generating subtle strengthening peaks in the annealed trends. This suggests that the grain boundary relaxation process, often described as a removal of excess dislocations from non-equilibrium grain boundaries [145-148], becomes less influential at the finest nanocrystalline grain sizes.

To gain a further understanding as to the effect of grain boundary relaxation on the underlying deformation behavior, we have calculated the activation volume as a function of grain size,

which is illustrated in Figure 6.2; as-deposited data from Chapter 4 are included for reference.

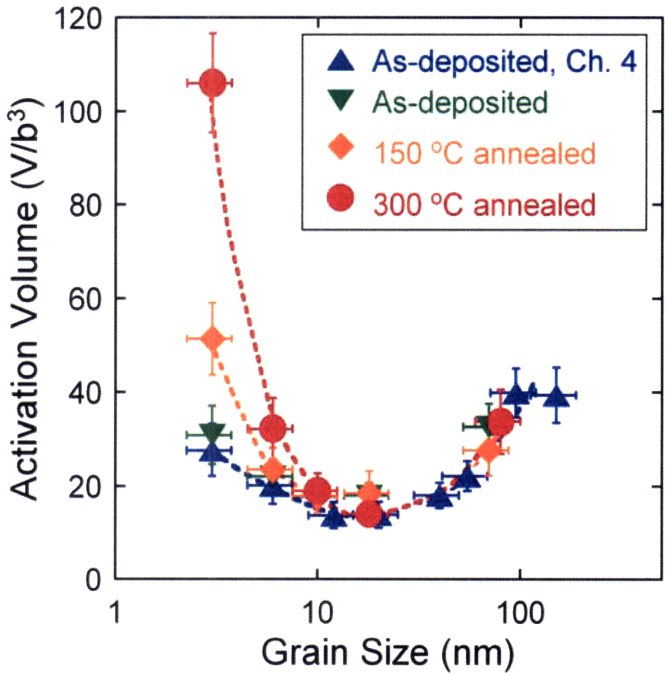

Figure 6.2: Activation volume for the present Ni-W alloys in as-prepared and relaxed states, normalized by the cubed Burger's vector, b^3. Measurements of V from Chapter 4 are included for reference, as well as general trend lines. While the activation volumes for the relaxed specimens are in-line with the as-deposited values for grain sizes ≥12 nm, finer grain size specimens exhibit noticeable increases in V with increasing annealing temperature.

For grain sizes down to ~ 12 nm, annealing has no effect on the measured values of V, indicating that the fundamental deformation mechanisms are unchanged by grain boundary relaxation over this range. Dislocation-mediated processes, initially in the form of unit dislocations, eventually transitioning to partials, are the anticipated carrier of plasticity at these grain sizes (cf. Figure 1.4). If we assume that plasticity is in fact mediated by the emission of dislocations from existing grain boundary sources, as proposed by Asaro et al. [61], removal of excess grain boundary dislocations effectively reduces the number of sources available to nucleate intragranular partial and/or unit dislocations. In the absence of competing mechanisms, fewer emission sources would act to enhance the critical shear stress required to initiate slip, accounting for the observed strengthening upon relaxation of the boundaries, but without

changing the fundamental mechanisms as implied by the consistent activation volume. Furthermore, because the grain boundary volume fraction scales inversely with grain size, the relaxation process can be expected to more strongly influence the strengthening behavior of finer nanocrystalline metals with a much higher interfacial area, thus rationalizing the grain size-dependent hardening behavior observed in Figure 6.1.

While the activation volume is relatively unaffected by the annealing process at grain sizes above the Hall-Petch breakdown, a subtle increase in V is observed at d = 6 nm, which becomes much more pronounced at the finest grain size of 3 nm. Interestingly, shear localization emerged in the as-deposited d = 3 nm specimen (cf. Section 4.2), and such structural shear banding is usually associated with rate-independent strength. Following this logic, we may imagine that the increase in V for the annealed samples, corresponding to a reduction in rate sensitivity, implies an increased propensity for inhomogeneous flow after annealing at the finest nanocrystalline grain sizes. Inspection of the plastic zones around the residual impressions by SEM confirms this implication, as illustrated in Figure 6.3. Whereas small shear offsets are observed around the indentation site on the as-deposited specimen in Figure 6.3(a), the shear steps in the pile-up on annealed samples are much more pronounced, as observed in Figure 6.3(b) and (c). The reduced rate sensitivity and corroborating observations of enhanced shear banding in the plastic zones demonstrate that the structural relaxation process induced by low homologous temperature annealing promotes inhomogeneous flow at the finest nanocrystalline grain sizes.

An interesting aspect of the present results, pertaining primarily to the 3 nm grain size sample, is that the deformation behavior upon relaxation is strikingly similar to that observed in molecular dynamics simulations of nanoindentation on metallic glasses, performed by Shi and Falk [275, 276]. These authors studied the effect of quench rate on the shear banding behavior, with emphasis on the role of local atomic order. Whereas rapidly quenched structures, characterized by a high degree of disorder similar to the as-deposited state, exhibit smaller shear bands and a lower hardness, structures quenched at slower rates with a higher degree of local order, more

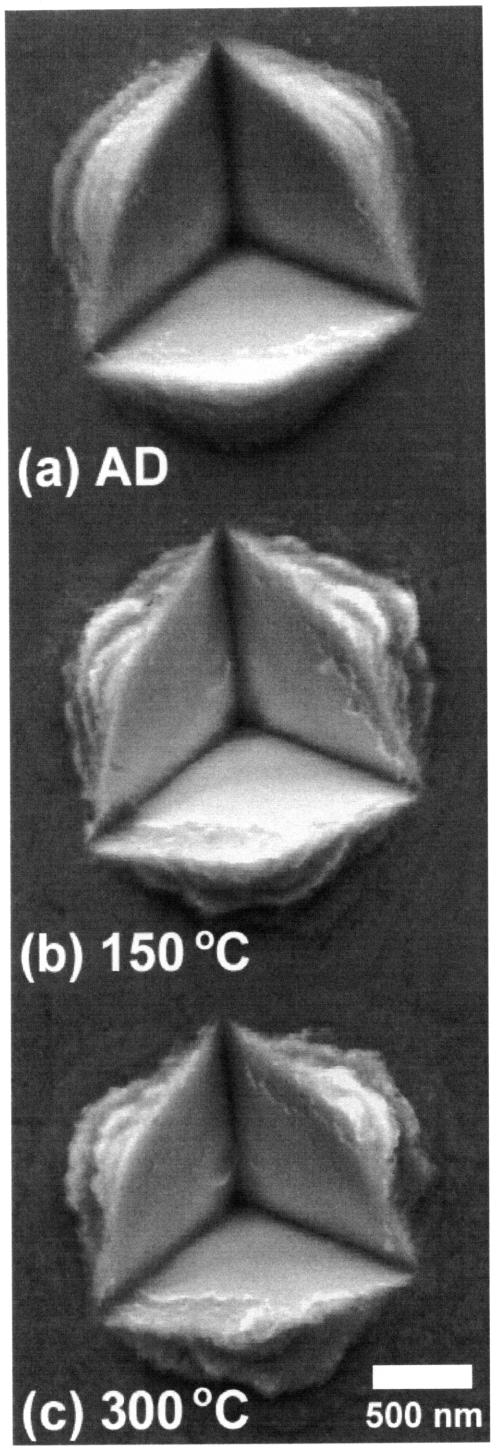

Figure 6.3: Scanning electron micrographs of the residual impressions on 3 nm grain size Ni-W specimens, in the (a) as-deposited condition, and annealed at (b) 150 °C and (c) 300 °C. An increase in the shear offset width is evident from (a)-(c), indicating that grain boundary relaxation promotes inhomogeneous flow at the finest nanocrystalline grain sizes.

akin to our relaxed samples, reveal larger shear bands and are stronger than their rapidly quenched counterparts. We observe experimentally that structural relaxation, i.e. local ordering, indeed promotes glass-like shear banding, thus further substantiating that the finest nanocrystalline metals behave like metallic glasses.

6.2 Elevated temperature deformation behavior of heat treated Ni-W alloys

Having characterized the effect of structural relaxation, we can now turn our attention to elevated temperature mechanical tests, which are advantageous as they enable an evaluation of the activation energy for thermally-activated plastic flow. Combined with the activation volume measurements, activation energies would facilitate a more comprehensive discussion of the underlying deformation mechanisms. In this section, we present such a study, where three fully relaxed nanocrystalline grain size specimens, indicated in Table 3.3, are subjected to elevated temperature mechanical tests in order to calculate the activation energies. We begin by introducing the high temperature nanoindentation techniques and methodology for determining the activation energy of deformation. Implications for the nanoscale deformation physics are subsequently discussed, with emphasis on competing mechanisms and the shift to interface-mediated plasticity.

6.2.1 High-temperature nanoindentation procedures

The indentation experiments were conducted with a Hysitron Ubi1 nanoindenter, modified for elevated temperature indentation testing. Specimens prepared with standard metallographic techniques to a roughness of < 10 nm were clamped down to a copper stage, which was surrounded with NiCr resistively heated wires to control the sample temperature. The transducer and piezotube were isolated with a water-cooled copper transducer shield, and an extended zero thermal expansion Berkovich tip was used in testing. As in the room temperature testing, a maximum load of 10 mN and constant strain rate of 1.5 s^{-1} (cf. Section 4.1) were employed, and both the pre- and post-test drift rates were used in the analysis. A minimum of 25 indentation curves were used to calculate the hardness at each of six different temperatures, incrementally increased by 25 °C over the range $25 \leq T \leq 150$ °C. The area function was calibrated on fused

silica at room temperature, and its consistency was verified at 150 °C, representing the highest temperature used in testing.

Because a large number of tests are required to determine the average hardness and standard deviation, the samples remain at temperature for extended periods of time, longer than days in some cases. To ensure that the specimens are indeed fully relaxed prior to indentation testing, we evaluated the Vickers microhardness, using a Clark Instruments model DMH2 microindenter, as a function of temperature and time for the 3 nm grain size specimen; the results are shown in Figure 6.4. Note that the grain size calculated from x-ray diffraction data remain unaffected by

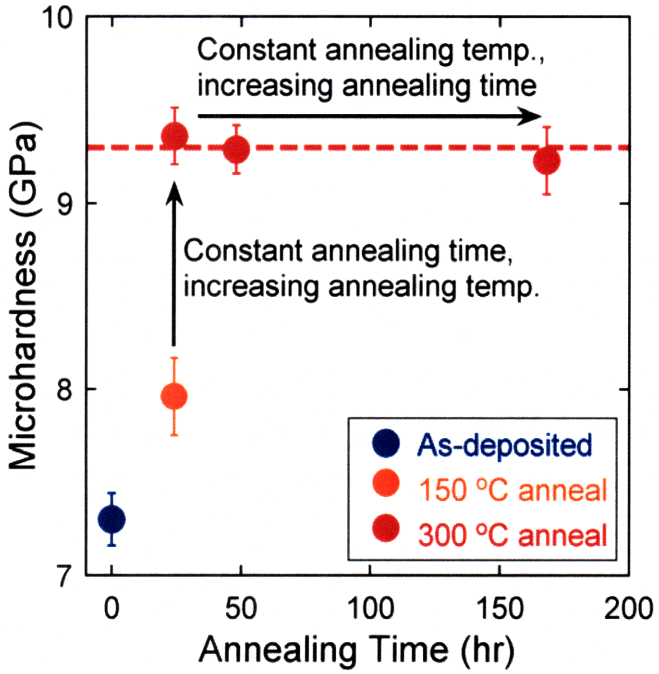

Figure 6.4: Microhardness for the 3 nm grain size Ni-W specimen annealed to different extents. For a given annealing time of 24 hours, an increase in the annealing temperature leads to an increase in strength, attributed to grain boundary relaxation in Section 6.1, followed by a time-independent plateau; grain size also remains constant.

the various heat treatments in Figure 6.4 to within measurement error. Once the sample is heat treated at 300 °C for 24 hours, subsequent annealing does not alter the hardness, indicating that the specimen is in a fully relaxed state. Therefore, the three grain size samples used in the high

temperature indentation experiments were subjected to a 24 hour anneal at 300 °C prior to testing.

6.2.2 Determination of the activation energy

The Gibbs activation energy for deformation in Eq. (6.1) is a function of the temperature, stress, and strain rate, and is expanded in terms of the Helmholtz free energy, effective stress, and activation volume in Eq. (6.2). Application of this relation to calculate ΔF would require not only measurements of τ_e at multiple test temperatures, but also the temperature dependence of the activation volume. The latter characterization would require a large number of tests across the full range of indentation strain rates employed in Chapter 4, and at elevated temperatures where the drift rate becomes more unstable [277], an extremely low yield percentage can be anticipated for data acquired at low strain rates. An alternative means of extracting the activation energy is presented by Conrad et al. [278], where the following equation is derived for the enthalpy of activation:

$$\Delta H = -k \cdot T^2 \left[\frac{\left(\frac{\partial \tau}{\partial T} \right)_{\dot{\gamma}} - \frac{\tau}{\mu} \left(\frac{\partial \mu}{\partial T} \right)}{\left(\frac{\partial \tau}{\partial (\dot{\gamma}/\dot{\gamma}_o)} \right)_T} \right] \tag{6.3}$$

with μ equal to the shear modulus. The leading term in the numerator is exactly the quantity we are addressing in this section, i.e. the dependence of yield stress on temperature at a constant strain rate. The second term incorporates the change in modulus with temperature, which is scaled by the ratio of the stress to the shear modulus. The contribution of this term is negligible as compared to the leading term (roughly an order of magnitude less), and is thus ignored in the present analysis. The denominator describes the change in yield stress with strain rate at a constant temperature, which is inversely proportional to the activation volume (cf. Eq. (1.2)). Substituting Eq. (1.2) into Eq. (6.3), and incorporating an approximate conversion between hardness and yield stress, we obtain:

$$\Delta H = -T \cdot V \left(\frac{\partial \tau}{\partial T} \right)_{\dot{\gamma}} \tag{6.4}$$

where V is measured at temperature T (i.e. at ambient temperature as in Chapter 4). The activation enthalpy for deformation at this temperature is denoted ΔH, which is often assumed equivalent to the activation energy (ΔH $\propto$ Q) [279]. It is important to note that ΔH is different from ΔF presented in Eq. (6.2), as the latter incorporates entropic contributions by measuring V as a function of T. For the purposes of the present study, we will be determining the activation enthalpy via Eq. (6.4).

Figure 6.5 illustrates the yield stress, as determined from the nanoindentation hardness measurements, as a function of temperature (in Kelvins) for grain sizes of 80, 18, and 3 nm.

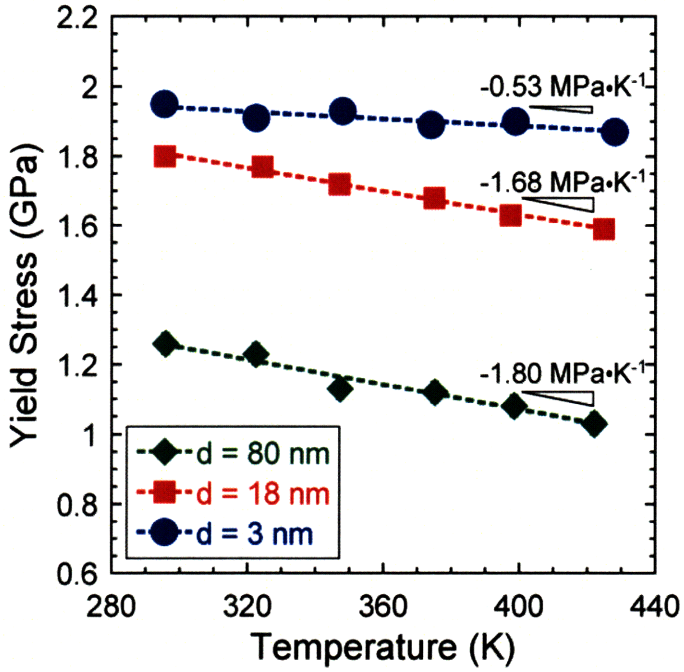

Figure 6.5: Yield stress as a function of temperature for three nanocrystalline grain size specimens, as calculated from the indentation hardness. A linear regression procedure is used to determine each of the slopes, which are included for reference.

Error bars cannot be seen because they are on the order of the data point size for both variables. A least squares fit was used to determine the indicated slopes, which are observed to vary with grain size. Substituting these results and the grain-size dependent activation volumes from Chapter 4 into Eq. (6.4), the activation energy for deformation can be calculated as a function of grain size, and is shown in Figure 6.6. A decrease in activation energy is observed across the

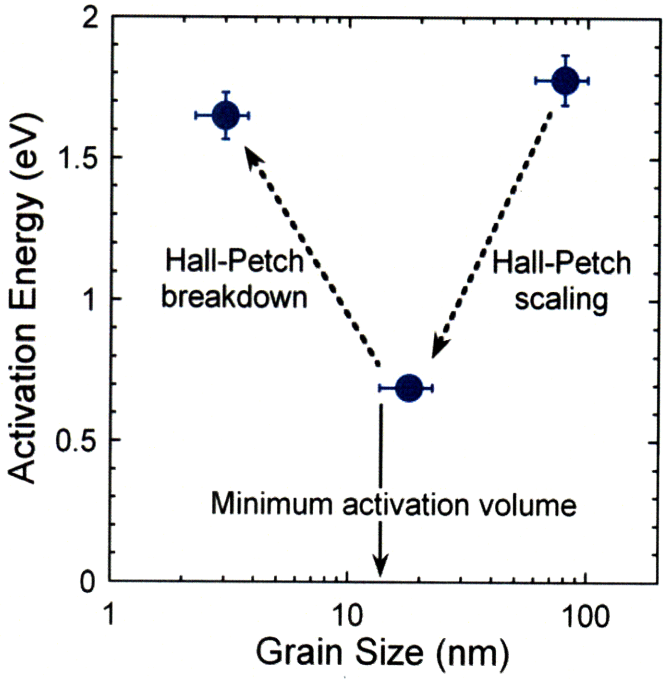

Figure 6.6: Activation energy as a function of grain size determined from Eq. (6.4). Hall-Petch scaling and breakdown regimes, and the grain size associated with the minimum activation volume, are indicated. An inflection is observed in the activation energy, implying fundamental changes in the underlying deformation mechanisms.

Hall-Petch strength scaling regime, followed by a minimum in the vicinity of the activation volume inflection, and subsequent increase at the finest nanocrystalline grain sizes across the breakdown regime. Such behavior substantiates the shift in deformation mechanisms across the Hall-Petch breakdown initially proposed in Chapter 4, and is the topic of the following section.

6.2.3 Implications for the underlying deformation mechanisms

Table 6.1 summarizes the measurements of the activation volume from Section 6.1 and the activation energies determined in the previous section as a function of nanocrystalline grain size.

Table 6.1: Activation quantities for the three grain size specimens subjected to elevated temperature nanoindentation testing. The respective W contents and activation energy normalized by the shear modulus and cubed Burger's vector are also included.

Grain Size (nm)	Composition (at % W)	Activation Volume (V/b^3)	Activation Energy (eV)	$\Delta H/(\mu \cdot b^3)$
80	3.9	33.8	1.8	0.15
18	15.2	14.1	0.7	0.09
3	26.6	105.5	1.6	0.21

Also included in the last column is the activation energy normalized by the shear modulus and cubed Burger's vector, representing a useful parameter in the study of dislocation dynamics. Mutually consistent inflections in both activation quantities are observed, which supports a transition in the nanoscale deformation physics. For the 80 and 18 nm grain size specimens, the values of $\Delta H/(\mu \cdot b^3)$ are ≤ 0.15, with associated activation volumes of 33.8 and $14.1 \cdot b^3$, respectively; for forest dislocation interactions, these quantities are in the range 0.2–1.0 [280] and 100–1000 b^3 [41, 47, 50], respectively; we conclude that this mechanism is not rate controlling at either grain size.

The unusual scaling of activation volume in the nanocrystalline regime has been attributed to dislocation emission from grain boundary ledges [61, 150], nucleating from either existing boundary dislocations or stress concentrations, with V taking on values of $10–50 \cdot b^3$. At larger nanocrystalline grain sizes, the deformation process is expected to involve unit dislocations, whereas emission of partial dislocations should come to control the strength in the vicinity of the Hall-Petch breakdown. This could potentially account for the observed reduction in activation energy, since the emission of partials should require less energy than unit dislocations. The reduced activation energy at d = 18 nm is also in agreement with measurements performed on

nanocrystalline metals of similar grain size [47, 272]. Furthermore, additional complexities associated with the alloying content can also influence the activation energy. The 80 nm grain size sample has a W content of only 3.9 at %, while the 18 nm grain size sample has 15.2 at % W. The latter specimen will inherently have a much lower stable stacking fault energy [281], and nucleation of a leading partial will therefore require less energy [61], rationalizing the lower activation energy at d = 18 nm. Of course, the effect of W and the competing dislocation mechanisms described above are strongly connected. In any case, these rationalizations collectively support grain boundary-accommodated dislocation activity as the rate-limiting deformation process for the two larger grain size samples.

For the finest nanocrystalline specimen, the activation quantities deviate significantly from the trends observed at larger nanocrystalline grain sizes, where V diverges to $> 100 \cdot b^3$, and ΔH more than doubles from the value measured at 18 nm to 1.6 eV. In light of these activation quantities, Coble creep and diffusion-mediated grain boundary sliding, with expected activation volumes and energies based on grain boundary diffusion of $\sim 1 \cdot b^3$ [50] and ~0.5 eV [47, 129], can be ruled out as the rate-limiting processes. Furthermore, dislocation plasticity of the form described above is not expected to be the dominant deformation mechanism at such fine grain sizes [90, 95]. As demonstrated in Chapters 4 and 5, shear localization becomes the dominant form of plasticity at the finest nanocrystalline grain sizes, and the divergence of V supports such a mechanistic transition as shear localization has large characteristic activation volumes. A recent model by Joshi and Ramesh [112-114] investigated the onset of shear instabilities accommodated by grain rotation in BCC and FCC nanocrystalline metals, and for the latter, demonstrated that shear localization is delayed to finer grain sizes, in accordance with the transition to inhomogeneous, glass-like flow. These observations suggest that the rate-controlling mechanism transitions to a shear localization process, similar to the structural shear bands found in metallic glasses, as the nanocrystalline grain size approaches the amorphous limit.

6.3 Concluding remarks

The deformation behavior of heat treated Ni-W alloys was investigated in this chapter, with emphasis on the role of grain boundary relaxation and elevated temperature mechanical testing. Grain boundary relaxation was demonstrated to promote strengthening across the Hall-Petch

breakdown, and inhomogeneous flow at the finest nanocrystalline grain sizes. Activation energies were determined from high temperature nanoindentation tests, and presented with the corresponding activation volumes to provide a more comprehensive discussion of the underlying deformation mechanisms. Based on the magnitudes of these quantities, classical dislocation plasticity, such as forest interactions, was ruled out as possible deformation processes. By comparison with existing analytical models, grain boundary-mediated dislocation plasticity was suggested as the rate-limiting process for grain sizes down to the Hall-Petch breakdown. At finer nanocrystalline grain sizes, the observed increase in activation volume, inflection in activation energy, and observations of shear banding all indicate that shear localization becomes the dominant carrier of plasticity. This result is further substantiated by recent modeling efforts, which predict the onset of shear instabilities in FCC nanocrystalline metals at the finest grain sizes.

Conclusions

Nanocrystalline metals have presented unique opportunities to study interface-dominated physics at the nanoscale, with atomistic simulations representing a central technique in elucidating this behavior. Strong conclusions based on experimental evaluations have been more elusive, stemming from the difficulty in processing homogeneous, defect-free samples for mechanical testing. Alloying has been proposed as a potential route to high-quality nanocrystalline metals, although the theoretical framework necessary to describe nanostructure stability in general binary alloy systems has been lacking. This thesis has addressed both of these topics, first focusing on the thermodynamics and synthesis of nanocrystalline alloys, and then their mechanical properties across the entire nanocrystalline regime. The relevant conclusions of this thesis are summarized below.

In Chapter 2, an analytical model was developed based on the principles of statistical thermodynamics to describe nanostructure stabilization in terms of the energetic state variables central to binary alloy systems. The influences of these parameters were systematically evaluated, and used to interpret equilibrium grain size trends in model alloy systems. Alloys such as Ni-W, which exhibit a moderate heat of mixing, were correlated to grain size-composition trends with a more moderate curvature, scaling at higher alloy compositions. These systems offer more precise control over the nanostructure, representing an improved strategy for the design of stable nanocrystalline metals.

Motivated by the foregoing analysis, in Chapter 3 we synthesized alloys of Ni-W with grain sizes spanning a very broad range (3 – 150 nm) via aqueous electrodeposition. Manipulation of the current waveform and electrolyte temperature enabled explicit control of the alloy composition, in turn, producing a variety of nanocrystalline grain sizes. Select specimens were also subjected to heat treatments for subsequent studies of structural relaxation, and to provide fully relaxed samples for high temperature mechanical tests. These materials were used throughout the entirety of this thesis to evaluate multiple mechanical properties, and their inherent dependence on the nanostructure.

In Chapter 4, quasi-static nanoindentation testing was employed to probe the mechanical behavior of the as-deposited Ni-W alloys, with specific emphasis on the Hall-Petch breakdown regime and implications for the underlying deformation behavior. We evaluated the strength, and its rate and pressure dependence, revealing mutually consistent inflections in all three mechanical properties in the vicinity of the Hall-Petch breakdown. The finest grain size specimens exhibited signatures of inhomogeneous flow, similar to shear banding in metallic glasses, marking an explicit transition to glass-like plasticity.

The grain size-dependent rate sensitivity determined in Chapter 4, specifically the maximum revealed in the vicinity of the Hall-Petch breakdown, implies that the character of this breakdown should in fact be rate-dependent. To validate this expectation, the as-deposited nanocrystalline Ni-W specimens were indented at high strain rates in Chapter 5, to study the dynamic strength scaling behavior across the nanocrystalline regime. Whereas the Hall-Petch breakdown manifests as a strength plateau at quasi-static rates, a marked peak strength is observed at high rates, relating directly to the maximum in rate sensitivity. The flow behavior was also demonstrated to depend on strain rate, where high rates increased the propensity for shear banding at larger nanocrystalline grain sizes across the breakdown regime. These findings unify conflicting simulation and experimental observations of the Hall-Petch breakdown, and also hold important implications for applications involving high deformation rate.

In Chapter 6, heat treated nanocrystalline Ni-W samples were also subjected to ambient temperature indentation tests to investigate the strength scaling behavior and rate sensitivity following structural relaxation. The relaxation process promoted strength increases across the Hall-Petch breakdown, attributed to the annihilation of dislocation nucleation sources, and also promoted inhomogeneous flow at the finest nanocrystalline grain sizes. Elevated temperature nanoindentation tests were finally performed on the relaxed samples to extract the activation energy for deformation. These measurements were shown to support grain boundary-mediated dislocation plasticity above the Hall-Petch breakdown, and inhomogeneous shear banding below, substantiating the shift to glass-like plasticity at the finest nanocrystalline grain sizes.

The present work represents a comprehensive study on alloying-induced stabilization of otherwise unstable high-energy interfaces, and their influence on deformation. The findings presented in this thesis, specifically the illumination of the deformation mechanisms associated with the Hall-Petch breakdown, will promote the optimization and exploitation of nanocrystalline metals as advanced structural materials. The present work also naturally suggests a number of key directions for future study, as described in the final section.

Directions for future work

The following topics represent the recommended focus of future research efforts:

- In Chapter 2, an equation was derived by considering the implications of the amorphous limit effectively representing the free energy a binary amorphous phase (cf. Eq. (2.16)), dependent on the solute content, temperature, and mixing and interfacial energies. It is expected that the interaction energies used in this model may be simply related to atomic size mismatches, as is common in discussing the structure and thermodynamics of metallic glasses. Probing this issue further could enable a comparison between thermodynamically stable amorphous solids, and formation of metallic glasses based on topological instabilities [282, 283].
- Aqueous electrodeposition was employed to produce nanocrystalline Ni-W specimens with grain size tailored by the reverse pulsing technique developed in Ref. [77]. Neither that study nor the present work investigated the electrochemical processes responsible for the effectiveness of the reverse pulse in stripping W from the deposit. Detailed electrochemical measurements, such as cyclic voltammetry, should be performed to better understand the complexes present in the electrolyte, and the mechanism responsible for the selective removal of W.
- A shift to glass-like deformation behavior was identified in Chapter 4, and proposed to offer a connection to amorphous-nanocrystalline composites. The finest nanocrystalline specimens should be characterized to a greater extent with high-resolution TEM to further elucidate the atomic structure, especially in the regions of the grain boundaries. Following this, a devitrified metallic glass, with a similar volume fraction and size distribution of nanocrystals, should be produced and characterized by nanoindentation to explore the continuity between these materials, in an effort to shed some light on the shear banding behavior in the finest nanocrystalline specimens.
- An increased inclination for shear banding was demonstrated at high strain rates, although the present work did not explicitly determine whether these are "structural" shear bands, as in metallic glasses, or adiabatic shear bands. Further characterization, such as by the fusible coating technique [284], is required to clarify if these are in fact

"structural" shear bands that form preferentially at high rate, perhaps due to the suppression of competing deformation mechanisms.

- An argument was suggested to rationalize the decrease in activation energy associated with a grain size reduction from 80 to 18 nm based on changes in the dislocation behavior. Both the change in grain size, and alloying content, can potentially influence the dislocation dynamics. Atomistic simulations, in the same vein as those performed by Van Swygenhoven et al. [25, 26], should be performed to study this effect at the nanoscale and relate to the experimentally determine activation volumes and energies .

Appendix A: Coding script for determining thermodynamically stable states

In Chapter 2, an analytical model is presented to study thermodynamic stability in binary nanocrystalline alloys. The influence of the various energetic variables was investigated, and revealed that the bulk and intergranular interaction energies are central to stabilizing nanocrystalline grain sizes. With a precise knowledge of the state variables for a given binary system, the coding script used in the parametric study can be employed to evaluate the effect of the more elusive system parameters, such as the solution interaction energies. In what follows, the script used in Section 2.2.2 to solve for equilibrium states as a function of the bulk interaction energy, developed in Matlab, is presented, and annotations are included throughout for clarification. While this is specifically aimed to investigate variations of ω_b, trivial modifications to the variable arrays will adapt the script for iterations of other system parameters.

```
Read-in constants
D = 3;
T = 1273;
wgb = 0;                        intergranular interaction energy
Esbaa = 0.01;                   solvent grain boundary energy in eV/at
Esbbb = 0.01;                   solute grain boundary energy in eV/at
t=0.5;
z=12;
R=0.00008617;
Read-in variables
d = xlsread('Input.xls', 1);    grain size array (read in from excel)
X = (0.0001:0.0001:.9999)';     global solute content array
cs = (0.0001:0.0001:.9999)';    intergranular solute content array
wb = (0.025:0.005:0.125)';      bulk interaction energy array in eV/at
Allocate memory for coding variables
cb = zeros(length(cs),1);       bulk solute content array
G = zeros(length(cs),1);
E = zeros(length(X),1);
temp = zeros(length(X),4);
soln = zeros(length(d),7);
Initiates bulk interaction energy iteration loop
for q=1:length(wb)
   h = waitbar(0,[('Calculating wb= '),num2str(wb(q))]);
Initiates master grain size iteration loop
  clear soln
  clear ref
  for i=1:length(d)
Rough calculations to zoom in on X-cs solution space
    for j=1:length(X)
      for k=1:length(cs)
        psi = 1-( ( (d(i)-t)/d(i) )^D );
```

```
    cb (k) = (X(j)-cs(k)*psi)/(1-psi);
    if cb(k) < 0
       break
    else if cb(k) > 1
          break
       else
       G (k) = z*(1-psi)*cb(k)*(1-cb(k))*wb(q)+...
      ...+(z/2)*psi*(1-cs(k))*Esbaa+(z/2)*psi*cs(k)*Esbbb+z*psi*cs(k)*(1-cs(k))*wgb+...
      ...+(z/2)*psi*((cs(k)*(cs(k)-cb(k))-(1-cs(k))*(cs(k)-cb(k)))*wgb-(cs(k)-...
       ...-cb(k))*((Esbbb-Esbaa)/2))+R*T*( psi*( cs(k)*log(cs(k)) + (1-cs(k))*log(1-...
       ...-cs(k)) )+(1-psi)*( cb(k)*log(cb(k)) + (1-cb(k))*log(1-cb(k)) ) );
       end
    end
   if k>1
       if G(k)> G(k-1)
          break                    this will break the loop through cs
       else
          continue
       end
    end
end
E (j) = (z/2)*Esbaa - z*cs(k-1)*(wb(q) - wgb*(1-1/(2*(1-psi))) - ((Esbbb-Esbaa)/2)*(1-...
  ...-1/(2*(1-psi)))) - z*(((cb(k-1)^2)-2*cb(k-1)*cs(k-1))*wb(q) + (cs(k-1)^2)*wgb*(1-...
 ...-1-/(2*(1-psi)))) + (z/(2*(1-psi)))*((cs(k-1)*(cs(k-1)-cb(k-1))+cb(k-1)*(1-cs(k-1)))*...
  ...*wgb + cb(k-1)*((Esbbb-Esbaa)/2))+...
  ...R*T*(cs(k-1)*log(cs(k-1)/cb(k-1)) + (1-cs(k-1))*log((1-cs(k-1))/(1-cb(k-1))));
if E(j) > 0
   temp(j,1)=X(j);
   temp(j,2)=cb(k-1);
   temp(j,3)=cs(k-1);
   temp(j,4)=E(j);
```

```
    else
      temp(j,1)=X(j);
      temp(j,2)=cb(k-1);
      temp(j,3)=cs(k-1);
      temp(j,4)=E(j);
      break                              this will break the loop through X
    end
  end
```

Refining the equilibrium values

```
    lowercase variables used here analogous to their counterparts above
  xr = (temp((j-1),1):0.00001:temp(j,1))';
  ref = zeros(length(xr),6);
  gr = zeros(length(xr),1);
  for r = 1:length(xr);
    for m=1:length(cs)
      psi = 1-( ( (d(i)-t)/d(i) )^D );
      cb (m) = (xr(r)-cs(m)*psi)/(1-psi);
      if cb(m) < 0
        break
      else if cb(m) > 1
          break
        else
        gr(m)=z*(1-psi)*cb(m)*(1-cb(m))*wb(q)+(z/2)*psi*(1-cs(m))*Esbaa+...
        ...+(z/2)*psi*cs(m)*Esbbb+z*psi*cs(m)*(1-cs(m))*wgb+...
        ...+ (z/2)*psi*((cs(m)*(cs(m)-cb(m))-(1-cs(m))*(cs(m)-cb(m)))*wgb-(cs(m)-...
        ...-cb(m))*((Esbbb-Esbaa)/2)) + R*T*( psi*( cs(m)*log(cs(m)) + (1-...
        ...-cs(m))*log(1-cs(m)) )+(1-psi)*( cb(m)*log(cb(m)) + (1-cb(m))*log(1-cb(m)) ) );
        end
      end
      if m > 1
        if gr(m)> gr(m-1)
```

```
        break                          this will break the loop through cs
      else
        continue
      end
    else
      continue
    end
end
Following refines the cs solution by reducing the iteration step size
eqcs = (cs(m-2):0.000001:cs(m))';
e = zeros(length(eqcs),1);
for s=1:length(eqcs)
   psi = 1-( ( (d(i)-t)/d(i) )^D );
   cb(s) = (xr(r)-eqcs(s)*psi)/(1-psi);
   if cb(s) < 0
      break
   else if cb(s) > 1
        break
      else
         e(s) = (z/2)*Esbaa - z*eqcs(s)*(wb(q) - wgb*(1-1/(2*(1-psi))) - ((Esbbb-
             ...-Esbaa)/2)*(1-1/(2*(1-psi))))-z*(((cb(s)^2)-2*cb(s)*eqcs(s))*wb(q)+...
            ...+(eqcs(s)^2)*wgb*(1-1/(2*(1-psi)))) + (z/(2*(1-psi)))*((eqcs(s)*(eqcs(s)-
            …-cb(s))+cb(s)*(1-eqcs(s)))*wgb + cb(s)*((Esbbb-Esbaa)/2))+...
           …+R*T*(eqcs(s)*log(eqcs(s)/cb(s)) + (1-eqcs(s))*log((1-eqcs(s))/(1-cb(s))));
      end
   end
   if s > 1
      if e(s) > 0
         break                         breaks eqcs loop
      else
         continue
```

```
            end
          else
            continue
          end
        end
        slope = (e(s)-e(s-1))/(eqcs(s)-eqcs(s-1));
        b = e(s)-slope*eqcs(s);
        eq = -b/slope;
        eqcb = (xr(r)-eq*psi)/(1-psi);
        H = z*(wb(q) - wgb*(1-1/(2*(1-psi))) - ((Esbbb-Esbaa)/2)*(1-1/(2*(1-psi)))) +...
          ...+2*z*wgb*eq*(1-1/(2*(1-psi))) - 2*z*(wb(q)*eqcb + (wgb/2)*(eq-eqcb));
        gbe = slope*eq + b;
        riv = (eq/(1-eq))-(eqcb /(1-eqcb))*exp(H/(R*T));
        ref(r,1)=xr(r);
        ref(r,2)=eqcb;
        ref(r,3)=eq;
        ref(r,4)=H;
        ref(r,5)=gbe;
        ref(r,6)=riv;
        if r > 1
          if abs(ref(r-1,6)) < abs(ref(r,6))
            break                                    breaks the loop through xr
          else
            continue
          end
        else
          continue
        end
      end
```

Cataloguing Equilibrium Solutions

```
      soln(i,1) = d(i);          catalogues equilibrium grain size
```

```
    soln(i,2) = ref(r-1,1);      catalogues global solute content
    soln(i,3) = ref(r-1,2);      catalogues bulk solute content
    soln(i,4) = ref(r-1,3);      catalogues boundary solute content
    soln(i,5) = ref(r-1,4);      catalogues segregation energy
    soln(i,6) = ref(r-1,5);      catalogues equilibrium grain boundary energy
    soln(i,7) = ref(r-1,6);      catalogues value of 1st derivative
    waitbar(i/length(d),h)
  end
Solution Filter   <clear filter>
      filter(1,1) = soln(1,1);      catalogues grain size
      filter(1,2) = soln(1,2);      catalogues global solute content
      filter(1,3) = soln(1,3);      catalogues bulk solute content
      filter(1,4) = soln(1,4);      catalogues boundary solute content
      filter(1,5) = soln(1,5);      catalogues segregation energy
  n = 2;
  for i = 2:length(d)
    if abs(soln(i,4)-soln(i-1,4)) > 0.04*soln(i-1,4)
      continue
    else
      filter(n,1) = soln(i,1);      catalogues grain size
      filter(n,2) = soln(i,2);      catalogues global solute content
      filter(n,3) = soln(i,3);      catalogues bulk solute content
      filter(n,4) = soln(i,4);      catalogues boundary solute content
      filter(n,5) = soln(i,5);      catalogues segregation energy
      n = n + 1;
    end
  end
Writes output file
  xlswrite('output.xls',filter,strcat('wb=',num2str(wb(q))))
  close (h)
end
```

Appendix B: The Hall-Petch breakdown at constant W content

An important feature of experimental alloys studied in Chapter 4 is that their nanocrystalline grain size is linked directly to the alloy composition. The range of grain sizes from 3 to 150 nm is associated with alloy compositions ranging from 27 to 1 at% W, respectively, as observed in Figure 3.2. The origin of this effect has been attributed to a subtle tendency for W to segregate to the grain boundaries in Ni, as confirmed by atom probe tomography observations [190, 285] as well as computer simulations [194], and discussed extensively in Chapter 2. In this appendix, we compare the deformation behavior of the relaxed samples discussed in Section 6.1 with varying W content, to that of specimens with a constant W content of 21.3 at % with grain sizes spanning the Hall-Petch breakdown regime

Grain size was manipulated via isothermal heat treatments, starting with a nanocrystalline specimen very near the amorphous limit, specifically with an as-deposited grain size and alloy composition of 6 nm and 21.3 at %, respectively. A sequence of annealing steps, cataloged in Table B.1, was performed in an inert Ar environment to vary the grain size up to ~40 nm.

Table B.1: Isothermal heat treatments used to vary the grain size for specimens with a given alloy composition of 21.3 at. %, and an as-deposited grain size of 6 nm, as indicated. Note that the heat treated grain sizes span the entire Hall-Petch breakdown.

As-deposited Grain Size (nm)	Annealing Temp. (°C)	Annealing Time (hrs)	Heat Treated Grain Size (nm)
6	300	24	6
	400	24	8
	500	24	10
	550	24	15
	600	24	40
	700	24	N/A- Ni_4W present

The heat treated grain sizes were calculated from the XRD spectra shown in Figure B.1 following the procedure described in Section 3.2, with the annealing temperatures indicated.

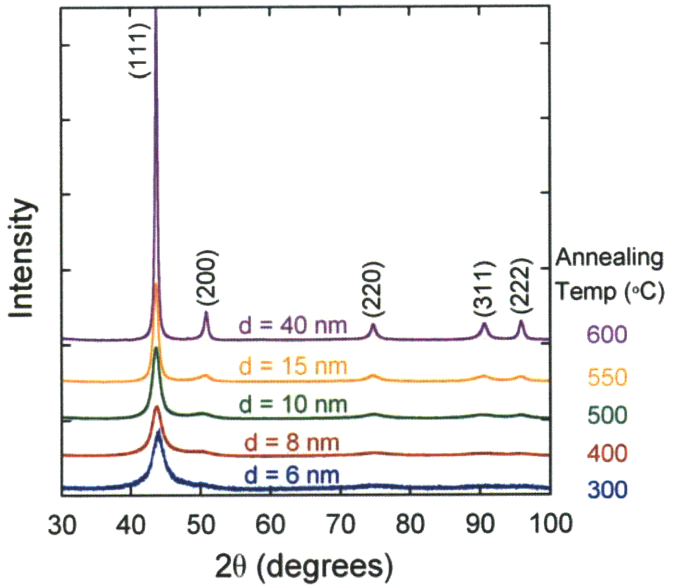

Figure B.1: XRD spectra for specimens exposed to the isothermal heat treatments shown in Table B.1; annealing temperatures and resultant grain sizes are indicated. The diffraction peaks sharpen, and additional FCC reflections become evident, as the annealing temperature is increased.

For a given annealing time of 24 hours, the diffraction peaks become substantially sharper with increasing temperature, indicating an increase in grain size as shown. Although no evidence indicative of intermetallic precipitation was observed up to 600 °C, a sixth sample annealed at 700 °C for 24 hours exhibited formation of a Ni_4W intermetallic phase, as observed most readily in the magnified insets in Figure B.2; the primary FCC relations are also present. An additional peak corresponding to tungsten oxide is detected, and attributed to surface oxidation during heat treatment. This particular specimen is not used in any subsequent nanoindentation testing, as any comparisons made to the other annealed samples would be inconsistent due to the presence of the Ni_4W intermetallic phase.

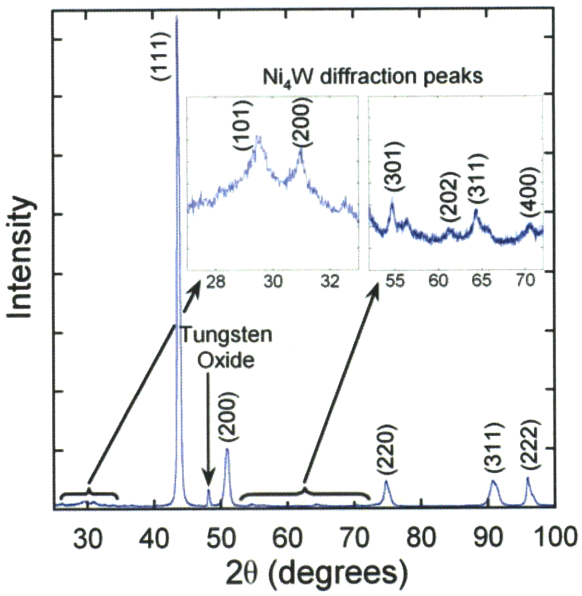

Figure B.2: XRD spectrum for an as-deposited 6 nm grain size Ni-W specimen annealed at 700 °C for 24 hours. Primary FCC Ni reflections are observed, as are diffraction peaks corresponding to the Ni_4W intermetallic phase. The latter peaks are seen more clearly in the insets, which show a magnified view of the indicated regions. An additional tungsten oxide peak is evident, which is due solely to a small amount of remnant oxide remaining after a rough polishing step following the heat treatment.

The strength scaling behavior for the 21.3 at % W specimens is shown in Figure B.3, along with the data for the 300 °C annealed Ni-W samples from Figure 6.1; nanoindentation procedures used to generate these data, and sample preparation methods, are described in Section 4.1, and error bars are again on the order of the data point size. Note that hardness values are the same at d = 6 nm, as this was the as-deposited grain size prior to application of the isothermal heat treatments. The 21.3 at % W alloys are noticeably harder across the Hall-Petch breakdown regime, exhibiting a maximum hardness at a grain size of ~18 nm. Whereas the hardness measured on the varying W specimens suggested weakening at the finest grain sizes (cf. Section 6.1), these data explicitly demonstrate an "inverse Hall-Petch" weakening regime, even at quasi-static strain rates.

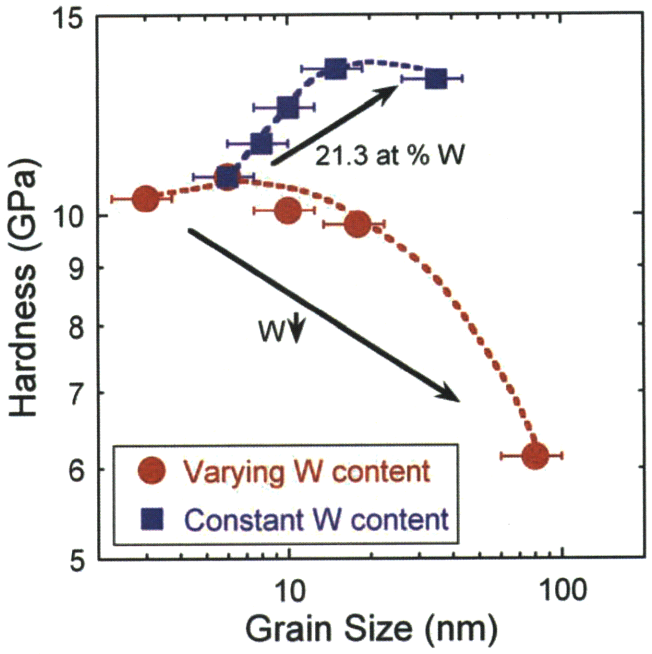

Figure B.3: Hardness as a function of grain size for the isothermally annealed Ni-W alloys with a given W content of 21.3 at % at 1.5 x 10^{-1} s^{-1}; the hardness values for the 300 °C heat treated alloys is reproduced from Figure 6.1, and trend lines are included for reference. The 21.3 at % W alloys are substantially harder than the varying W content samples across the Hall-Petch breakdown regime.

The hardness data for each of the five grain sizes with 21.3 at % W was fitted with Eq. 1.2 over seven indentation strain rates to determine the activation volumes shown in Figure B.4. The measurements of V from Figure 6.2 for the 300 °C annealed samples are also included, with the direction of decreasing W content indicated. For grain sizes less than ~12 nm, the activation volume for the 21.3 at % W and varying W alloys align to within measurement error. However, as the grain size is increased across the Hall-Petch breakdown regime, the activation volume for the constant W samples deviates from the scaling observed for the varying W content alloys, and this deviation becomes more pronounced at larger nanocrystalline grain sizes where the difference in W content becomes even greater. All other things being equal, the enhanced W content leads to an apparent increase in the activation volume, implying a fundamental change in the underlying deformation mechanisms.

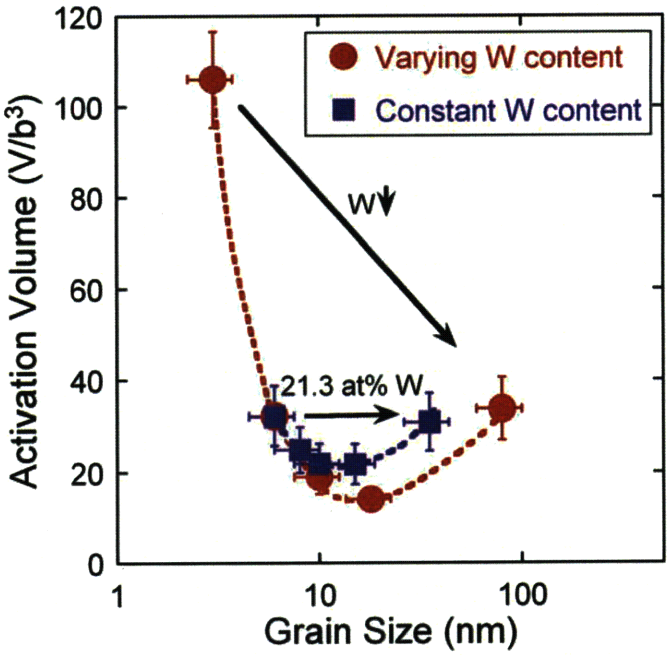

Figure B.4: Activation volume as a function of grain size for the 21.3 at % W alloys, plotted along with varying W content measurements from Figure 6.2; trend lines are included for reference. While the measurements of V for the 21.3 at % W samples align with the varying W data at fine nanocrystalline grain sizes, a noticeable deviation is observed when the grain size exceed ~ 10 nm.

To rationalize the anomalous increase in activation volume at higher W contents, we first assume that plasticity is mediated by emission of partial dislocations from grain boundary sources; the same assumption that was employed in explaining the activation volume of the relaxed specimens in Chapter 6. The behavior of these partial dislocations will be governed by the planar fault energy curves, particularly the ratio of the stable to unstable stacking fault energies [32, 34, 36]. Alloying Ni with W has been demonstrated to significantly decrease the stable stacking fault energy [281], which to first order, will essentially increase the width of the stacking fault created by emission of the leading partial, prior to generation of the trailing partial [286]. Molecular dynamics simulations have shown that extended partial dislocations emitted in nanocrystalline grains interact with the confining grain boundaries as they traverse from one end of the grain to the other [25, 36]. The volume over which the deforming shear stress acts will effectively increase due to these extended interactions, thus manifesting as a higher activation volume such as observed in the data in Figure B.4. What is more, the motion of the partial

dislocations through the grains will be hindered by the interaction of the extended stacking faults with the grain boundaries, and can be expected to lead to strengthening [31, 35, 36, 287]. This supports the presence of a hardness peak in Figure B.3 across the Hall-Petch breakdown regime. The "inverse Hall-Petch" behavior observed in heat treated nanocrystalline Ni-W alloys under quasi-static deformation rates can therefore be attributed to the influence of W on partial dislocation-mediated plasticity.

Appendix C: Methodology for analyzing high rate indentation data

The strength scaling behavior of nanocrystalline Ni-W alloys was investigated at high strain rates in Chapter 5 using dynamic indentation testing. A generalized methodology was highlighted to analyze the raw displacement-time data based on the first two impact events, and the coding script employed in this analysis, developed in Visual Basic interfacing with Excel, is presented in this appendix. To briefly summarize the procedure, the first step was to determine the incoming (maximum) velocity, which is subsequently used to identify the point of initial contact as $h = 0$, and shift the displacement data. The maximum depth incorporating this displacement shift was extracted, followed by determination of the residual depth according the procedure outlined in Section 5.1. The velocity associated with the residual depth represents the velocity of the tip upon exit from sample surface, denoted as the outgoing velocity. Based on these various procedures, we divide the script into specific subsections, which are connected to the displacement and velocity trends taken on coarse grained Ni, which were also used to validate the technique by comparison with Vickers micrhardness measurements. The variability in the raw data is also characterized, and accounted for in the data analysis and dynamic hardness calculations.

```
Sub DataProcessing()
'**********Calculates and indexes max velocity**********
Dim a As Integer
a = Worksheets("calc").Cells(2, 13)
Dim b As Integer
b = Worksheets("calc").Cells(2, 14)

Worksheets("Calc").Cells(8, 6) =
Application.WorksheetFunction.Max(Worksheets("Calc").Range("C5:C3996"))

  h = 5
  flag = 0

  Do While flag = 0

    If Worksheets("Calc").Cells(h, 3) = Worksheets("Calc").Cells(8, 6) Then

      flag = 1

    Else

      h = h + 1

    End If

  Loop
```

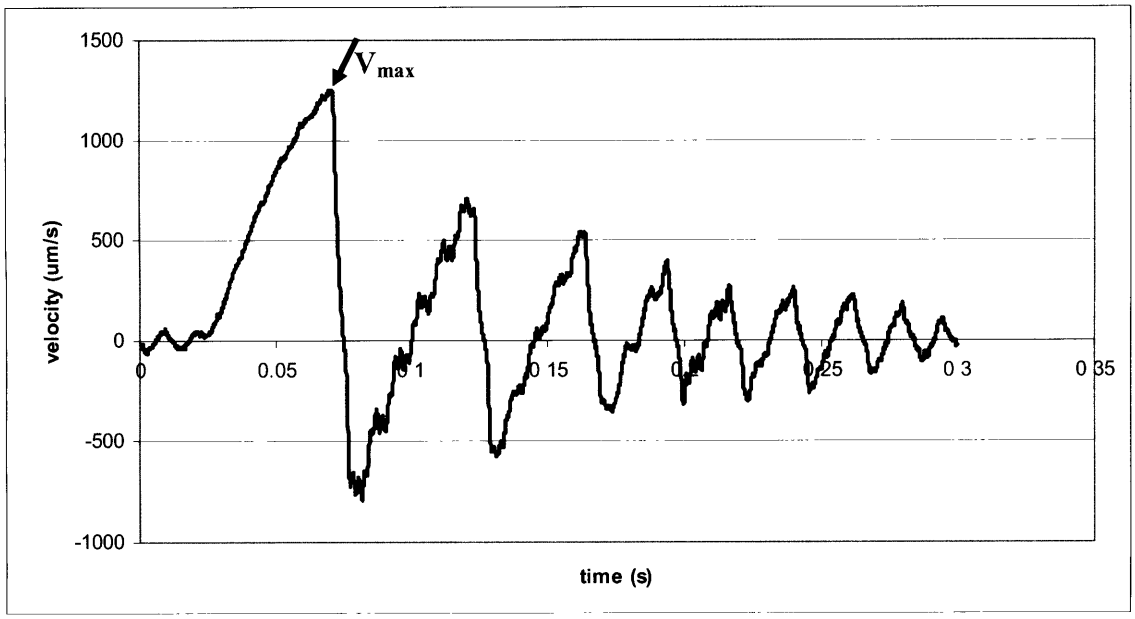

'*********determines incoming velocity and displacement offset***************

```
d = h - a
Worksheets("Calc").Cells(7,                    6)                    =
Application.WorksheetFunction.Min(Worksheets("Calc").Range(Worksheets("Calc").Cells(d,
3), Worksheets("Calc").Cells(h, 3)))
d = h
Do While Worksheets("calc").Cells(d, 3) > Worksheets("Calc").Cells(7, 6)
  d = d + 1
Loop
Worksheets("calc").Cells(2, 6) = Worksheets("calc").Cells(d, 3)
Worksheets("calc").Cells(2, 7) = Worksheets("calc").Cells(d, 2)

i = 1
Do While i < 4001
 Worksheets("Calc").Cells(i,4)=Worksheets("calc").Cells(i, 2)-Worksheets("calc").Cells(2, 7)
  i = i + 1
Loop
```

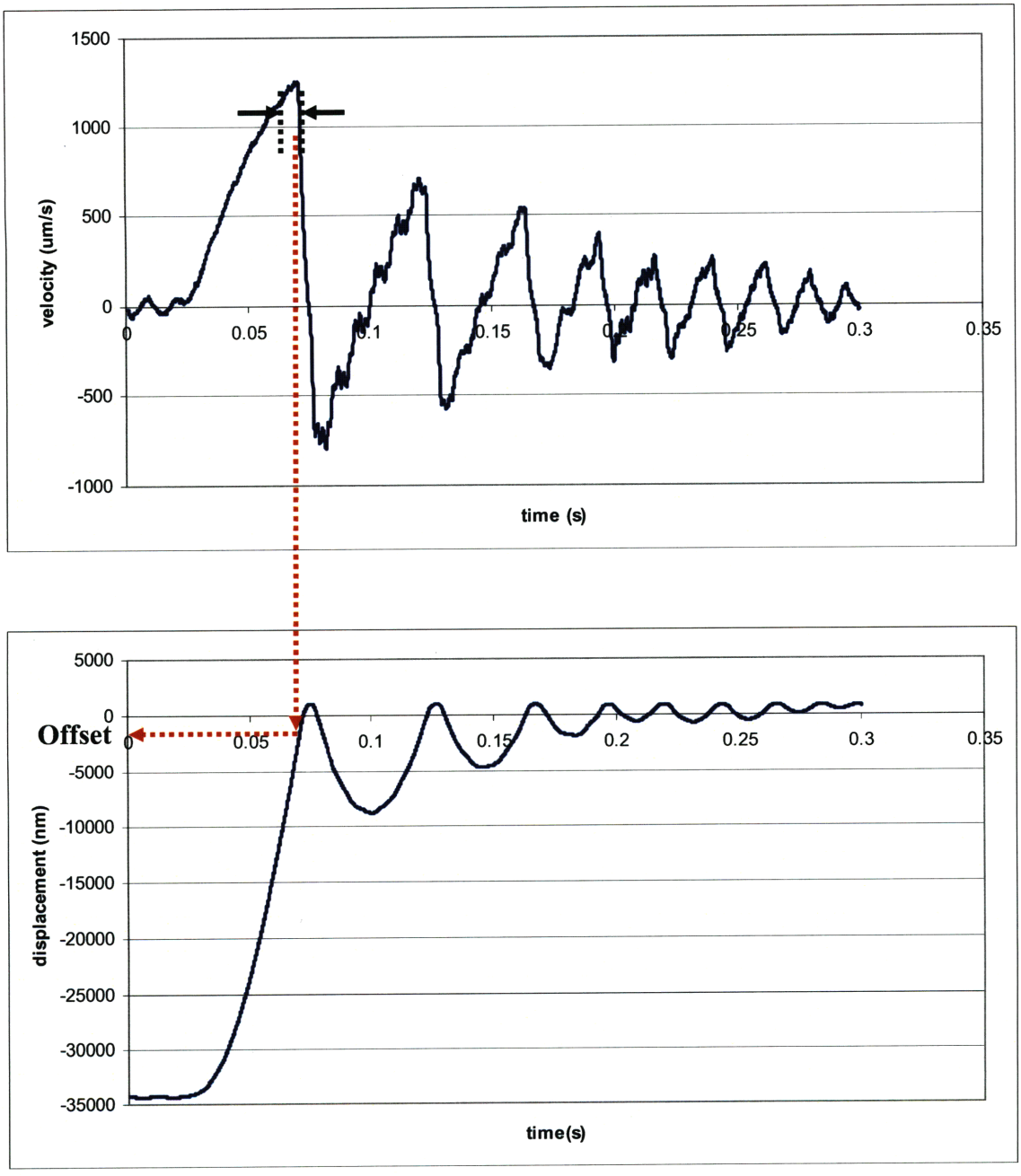
1500
1000
500
0
-500
-1000
velocity (um/s)
0
0.05
0.1
0.15
0.2
0.25
0.3
0.35
time (s)
5000
0
-5000
-10000
-15000
-20000
-25000
-30000
-35000
displacement (nm)
Offset
0
0.05
0.1
0.15
0.2
0.25
0.3
0.35
time(s)

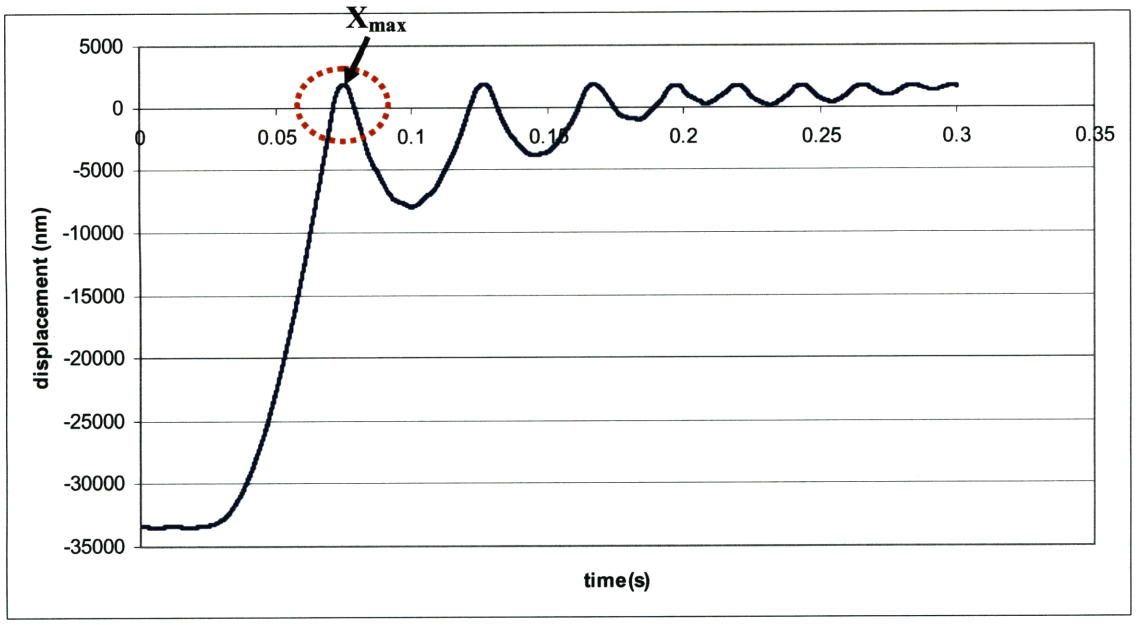

'**********determines max depth**********

```
m = d + 1
Do While Worksheets("Calc").Cells(m, 4) > 0
   m = m + 1
Loop

Worksheets("Calc").Cells(2, 8) = Application.WorksheetFunction.Max(Worksheets("Calc").Range(Worksheets("Calc").Cells(d, 4), Worksheets("Calc").Cells(m, 4)))
```

'**********determines residual depth**********

```
q = m + 1
Do While Worksheets("Calc").Cells(q, 4) < 0
   q = q + 1
Loop
r = q + 1
Do While Worksheets("Calc").Cells(r, 4) > 0
   r = r + 1
Loop
```

Catalogues 2nd impulse global max velocity:

```
Worksheets("Calc").Cells(8, 7) = Application.WorksheetFunction.Max(Worksheets("Calc").Range(Worksheets("Calc").Cells(m, 3), Worksheets("Calc").Cells(r, 3)))
```

Indexes 2nd impulse global max cell:

```
flag = 0
s = m
Do While flag = 0
  If Worksheets("calc").Cells(s, 3) = Worksheets("calc").Cells(8, 7) Then
    flag = 1
  Else
    s = s + 1
  End If
Loop
Worksheets("Calc").Cells(8, 8) = s
```

Catalogues min velocity in vicinity of 2nd max to characterize fluctuations:

```
Worksheets("Calc").Cells(9,7)=Application.WorksheetFunction.Min(Worksheets("Calc").Range
        (Worksheets("Calc").Cells(s - b,3), Worksheets("Calc").Cells(s + b, 3)))
```

Determines zero displacement correpsonding to 2nd impulse sample exi:t

```
Do While Worksheets("calc").Cells(s, 3) > 0
  s = s + 1
Loop
```

Searches velocity to determine point of decent:

```
s = s - 1
flag = 0
Do While flag = 0
```

```
    If Worksheets("calc").Cells(s - 1, 3) < Worksheets("calc").Cells(s, 3) And
      Worksheets("calc").Cells(s - 1, 3) > Worksheets("Calc").Cells(9, 7) Then
       flag = 1
    Else
       s = s - 1
    End If
Loop
```

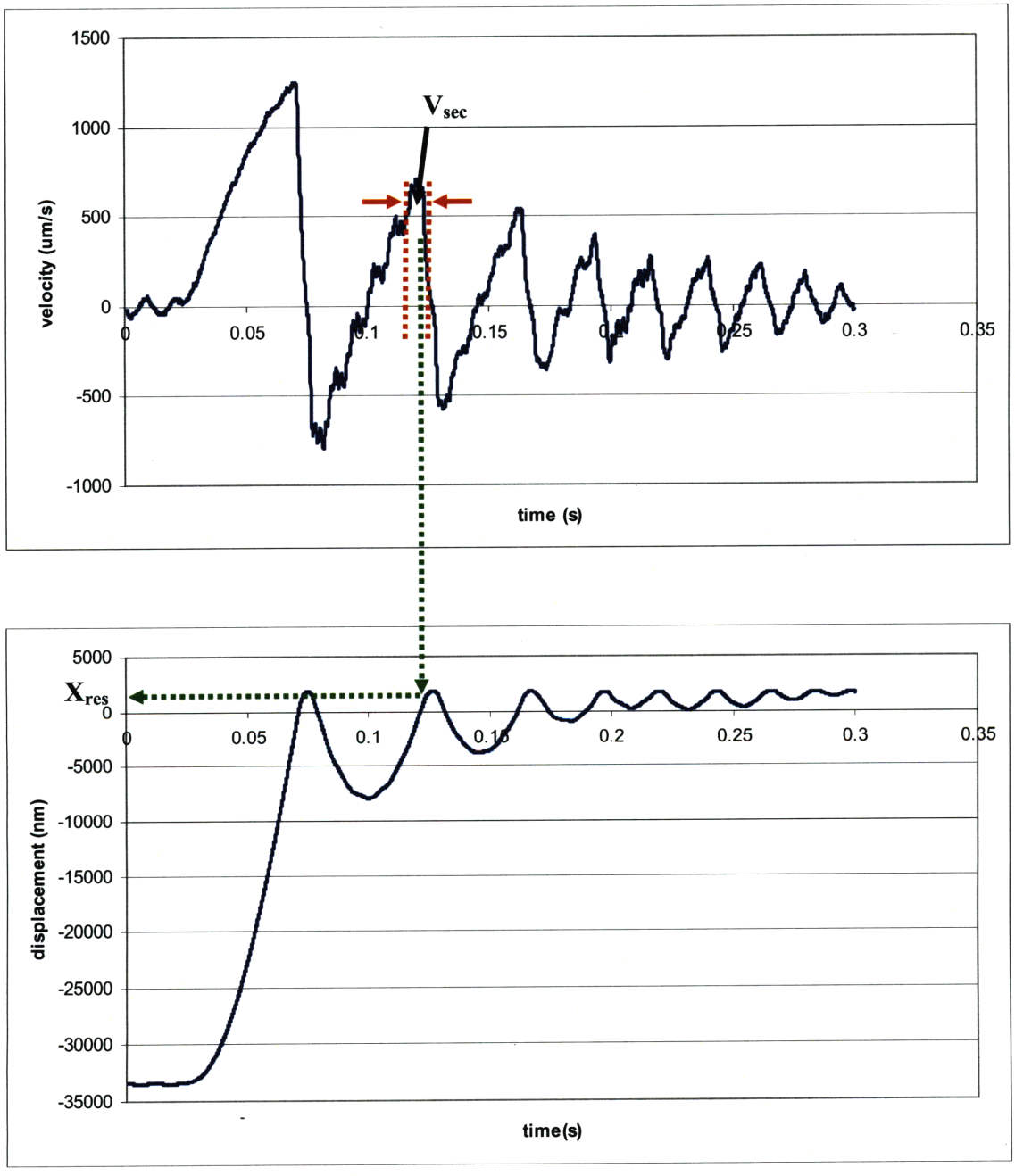

Extracts 2nd impulse velocity incorporating local data fluctuations:

```
   Do While Worksheets("calc").Cells(s, 3) > Worksheets("Calc").Cells(9, 7)
      s = s + 1
   Loop

   Worksheets("calc").Cells(7, 7) = Worksheets("calc").Cells(s, 3)
   Worksheets("calc").Cells(7, 8) = Worksheets("calc").Cells(s, 1)
   Worksheets("calc").Cells(2, 9) = Worksheets("calc").Cells(s, 4)

'*********determines output velocity***************
   t = m
   Do While Worksheets("calc").Cells(t, 4) > Worksheets("calc").Cells(2, 9)
      t = t - 1
   Loop

   If Abs(Worksheets("Calc").Cells(t + 1, 4) - Worksheets("Calc").Cells(2, 9)) <
Abs(Worksheets("Calc").Cells(t, 4) - Worksheets("Calc").Cells(2, 9)) Then
      Worksheets("Calc").Cells(2, 11) = Worksheets("Calc").Cells(t - 1, 3)
   Else
      Worksheets("Calc").Cells(2, 11) = Worksheets("Calc").Cells(t, 3)
   End If
   j = j + 1
Loop
End Sub
```

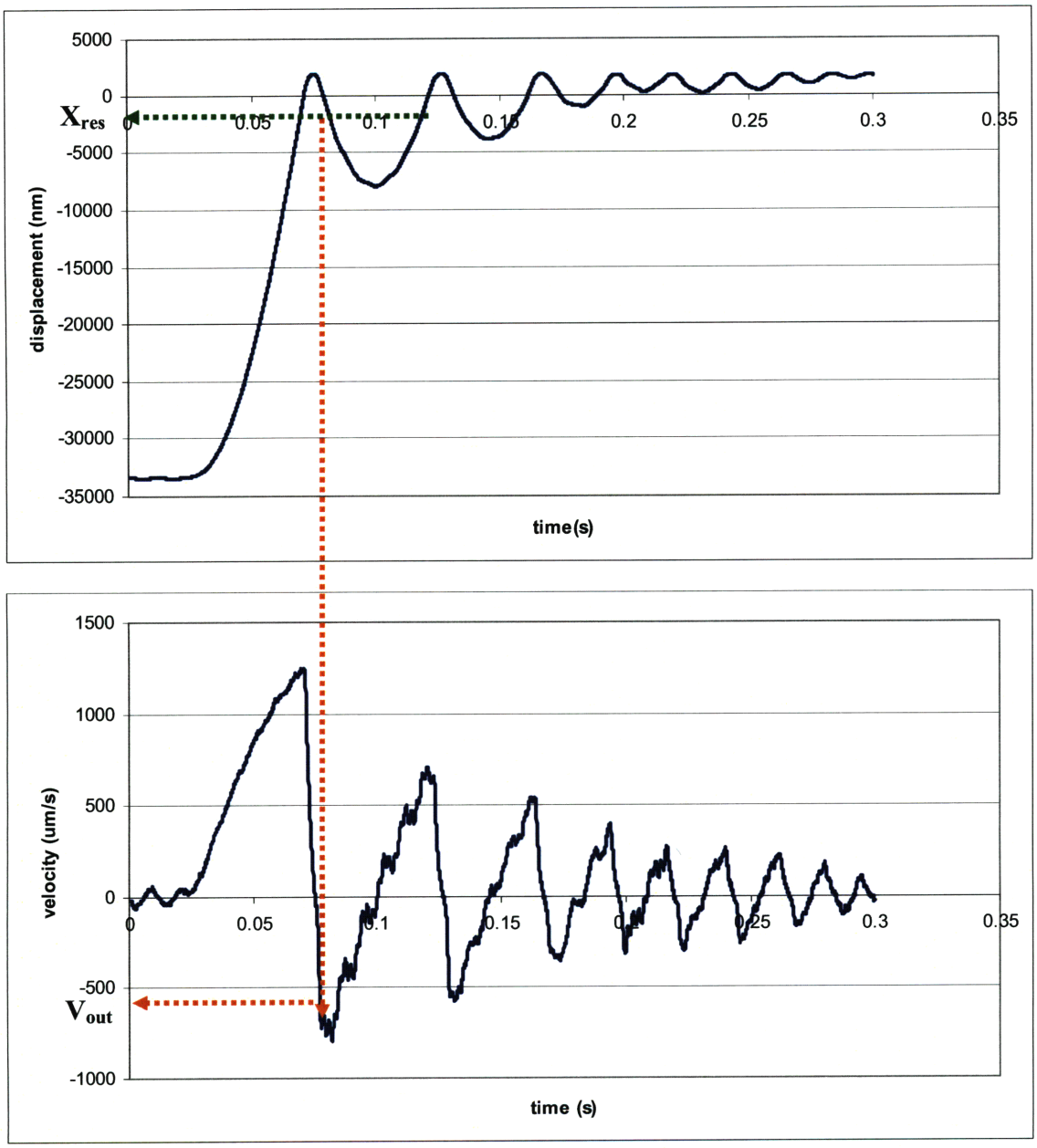
5000
0
-5000
-10000
-15000
-20000
-25000
-30000
-35000
displacement (nm)
X_{res}
0
0.05
0.1
0.15
0.2
0.25
0.3
0.35
time(s)
1500
1000
500
0
-500
-1000
velocity (um/s)
V_{out}
0
0.05
0.1
0.15
0.25
0.3
0.35
time (s)

References

[1] Dao M, Lu L, Asaro RJ, De Hosson JTM, Ma E. *Toward a quantitative understanding of mechanical behavior of nanocrystalline metals*. 2007;55:4041-4065.

[2] Gleiter H. *Nanostructured materials: Basic concepts and microstructure*. Acta Materialia 2000;48:1-29.

[3] Kumar KS, Van Swygenhoven H, Suresh S. *Mechanical behavior of nanocrystalline metals and alloys*. Acta Materialia 2003;51:5743-5774.

[4] Meyers MA, Mishra A, Benson DJ. *Mechanical properties of nanocrystalline materials*. Progress in Materials Science 2006;51:427-556.

[5] Suryanarayana C, Koch CC. *Nanocrystalline materials - Current research and future directions*. Hyperfine Interactions 2000;130:5-44.

[6] Van Swygenhoven H, Weertman JR. *Deformation in nanocrystalline metals*. Materials Today 2006;9:24-31.

[7] Hall EO. *The deformation and ageing of mild steel III. Discussion of results* Proc. Phys. Soc. B (UK) 1951;64:747-753.

[8] Petch NJ. *The upper yield stress of polycrystalline iron* Acta Metallurgica 1964;12:59-65.

[9] Karimpoor AA, Erb U. *Mechanical properties of nanocrystalline cobalt*. Physica Status Solidi a-Applications and Materials Science 2006;203:1265-1270.

[10] DallaTorre F, VanSwygenhoven H, Victoria M. *Nanocrystalline Electrodeposited Ni: Microstructure and Tensile Properties*. Acta Materialia 2002;50:3957-3970.

[11] Ebrahimi F, Bourne GR, Kelly MS, Matthews TE. *Mechanical properties of nanocrystalline nickel produced by electrodeposition*. Nanostructured Materials 1999;11:343-350.

[12] Gleiter H. *Nanocrystalline Solids*. Journal of Applied Crystallography 1991;24:79-90.

[13] Hughes GD, Smith SD, Pande CS, Johnson HR, Armstrong RW. *Hall-Petch Strengthening for the Microhardness of 12 Nanometer Grain Diameter Electrodeposited Nickel*. Scripta Metallurgica 1986;20:93-97.

[14] Jang JSC, Koch CC. *The Hall-Petch Relationship in Nanocrystalline Iron Produced by Ball Milling*. Scripta Metallurgica Et Materialia 1990;24:1599-1604.

[15] Weertman JR. *Hall-Petch Strengthening in Nanocrystalline Metals*. Materials Science and Engineering a-Structural Materials Properties Microstructure and Processing 1993;166:161-167.

[16] Ebrahimi F, Ahmed Z, Li HQ. *Tensile properties of electrodeposited nanocrystalline FCC metals*. Materials and Manufacturing Processes 2006;21:687-693.

[17] Li HQ, Ebrahimi F, Choo H, Liaw PK. *Grain size dependence of tensile behavior in nanocrystalline Ni-Fe alloys*. Journal of Materials Science 2006;41:7636-7642.

[18] Erb U. *Electrodeposited Nanocrystals: Synthesis, Properties and Industrial Applications*. Nanostructured Materials 1995;6:533-538.

[19] Kumar KS, Suresh S, Chisholm MF, Horton JA, Wang P. *Deformation of electrodeposited nanocrystalline nickel*. Acta Materialia 2003;51:387-405.

[20] Meyers MA, Mishra A, Benson DJ. *The deformation physics of nanocrystalline metals: Experiments, analysis, and computations*. Jom 2006;58:41-48.

[21] Bitzek E, Brandl C, Derlet PM, Van Swygenhoven H. *Dislocation cross-slip in nanocrystalline fcc metals*. Physical Review Letters 2008;100:-.

[22] Derlet PM, Van Swygenhoven H, Hasnaoui A. *Atomistic simulation of dislocation emission in nanosized grain boundaries*. Philosophical Magazine 2003;83:3569-3575.
[23] Shan ZW, Wiezorek JMK, Stach EA, Follstaedt DM, Knapp JA, Mao SX. *Dislocation dynamics in nanocrystalline nickel*. Physical Review Letters 2007;98:-.
[24] Tschopp MA, McDowell DL. *Grain Boundary Dislocation Sources in Nanocrystalline Copper*. Scripta Materialia 2008;58:299-302.
[25] Van Swygenhoven H, Derlet PM, Froseth AG. *Nucleation and propagation of dislocations in nanocrystalline fcc metals*. Acta Materialia 2006;54:1975-1983.
[26] Van Swygenhoven H, Derlet PM, Hasnaoui A. *Atomic mechanism for dislocation emission from nanosized grain boundaries*. Physical Review B 2002;66:-.
[27] Yamakov V, Wolf D, Salazar M, Phillpot SR, Gleiter H. *Length-scale effects in the nucleation of extended dislocations in nanocrystalline Al by molecular-dynamics simulation*. Acta Materialia 2001;49:2713-2722.
[28] Yamakov V, Wolf D, Phillpot SR, Mukherjee AK, Gleiter H. *Dislocation processes in the deformation of nanocrystalline aluminium by molecular-dynamics simulation*. Nature Materials 2002;1:45-48.
[29] Zhu T, Li J, Samanta A, Kim HG, Suresh S. *Interfacial plasticity governs strain rate sensitivity and ductility in nanostructured metals*. Proceedings of the National Academy of Sciences of the United States of America 2007;104:3031-3036.
[30] Louchet F, Weiss J, Richeton T. *Hall-Petch law revisited in terms of collective dislocation dynamics*. Physical Review Letters 2006;97:-.
[31] Bobylev SV, Gutkin MY, Ovid'ko IA. *Partial and split dislocation configurations in nanocrystalline metals*. Physical Review B 2006;73:-.
[32] Van Swygenhoven H, Derlet PM, Froseth AG. *Stacking fault energies and slip in nanocrystalline metals*. Nature Materials 2004;3:399-403.
[33] Wu XL, Zhu YT, Ma E. *Predictions for partial-dislocation-mediated processes in nanocrystalline Ni by generalized planar fault energy curves: An experimental evaluation*. Applied Physics Letters 2006;88:-.
[34] Brandl C, Derlet PM, Van Swygenhoven H. *General-stacking-fault energies in highly strained metallic environments: Ab initio calculations*. Physical Review B 2007;76:-.
[35] Shehadeh MA, Lu G, Chen Z, Kioussis N, Ghoniem NM. *Multiplane-induced widening of stacking faults in fcc metals*. Applied Physics Letters 2007;91:-.
[36] Van Swygenhoven H. *Footprints of plastic deformation in nanocrystalline metals*. Materials Science and Engineering: A 2008;483-484:33-39.
[37] Wu X, Zhu YT, Chen MW, Ma E. *Twinning and stacking fault formation during tensile deformation of nanocrystalline Ni*. Scripta Materialia 2006;54:1685-1690.
[38] Wu XL, Ma E. *Dislocations in nanocrystalline grains*. Applied Physics Letters 2006;88:-.
[39] Shan ZW, Stach EA, Wiezorek JMK, Knapp JA, Follstaedt DM, Mao SX. *Grain boundary-mediated plasticity in nanocrystalline nickel*. Science 2004;305:654-657.
[40] Jang D, Atzmon M. *Grain-boundary relaxation and its effect on plasticity in nanocrystalline Fe*. Journal of Applied Physics 2006;99:-.
[41] Wang YM, Hamza AV, Ma E. *Activation volume and density of mobile dislocations in plastically deforming nanocrystalline Ni*. Applied Physics Letters 2005;86:3.
[42] Ma E. *Watching the nanograins roll*. Science 2004;305:623-624.

[43] Liao XZ, Zhou F, Lavernia EJ, Srinivasan SG, Baskes MI, He DW, Zhu YT. *Deformation mechanism in nanocrystalline Al: Partial dislocation slip*. Applied Physics Letters 2003;83:632-634.
[44] Shan ZW, Wiezorek JMK, Knapp JA, Follstaedt DM, Stach EA, Mao SX. *Large lattice strain in individual grains of deformed nanocrystalline Ni*. Applied Physics Letters 2008;92:-.
[45] Wu XL, Ma E. *Dislocations and twins in nanocrystalline Ni after severe plastic deformation: the effects of grain size*. Materials Science and Engineering: A 2008;483-484:84-86.
[46] Chen J, Lu L, Lu K. *Hardness and strain rate sensitivity of nanocrystalline Cu*. Scripta Materialia 2006;54:1913-1918.
[47] Wang YM, Hamza AV, Ma E. *Temperature-dependent strain rate sensitivity and activation volume of nanocrystalline Ni*. Acta Materialia 2006;54:2715-2726.
[48] Wei Q, Cheng S, Ramesh KT, Ma E. *Effect of nanocrystalline and ultrafine grain sizes on the strain rate sensitivity and activation volume: fcc versus bcc metals*. Materials Science and Engineering A 2004;381:71-79.
[49] Chen J, Shi YN, Lu K. *Strain rate sensitivity of a nanocrystalline Cu-Ni-P alloy*. Journal of Materials Research 2005;20:2955-2959.
[50] Conrad H. *Grain size dependence of the plastic deformation kinetics in Cu*. Materials Science and Engineering a-Structural Materials Properties Microstructure and Processing 2003;341:216-228.
[51] Elmustafa AA, Tambwe MF, Stone DS. *Activation volume analysis of plastic deformation in fcc materials using nanoindentation*. Materials Research Society Proceedings 2003;750:Y8.14.11-16.
[52] Lian JS, Gu CD, Jiang Q, Jiang ZH. *Strain rate sensitivity of face-centered-cubic nanocrystalline materials based on dislocation deformation*. Journal of Applied Physics 2006;99:076103.
[53] Zehetbauer M, Seumer V. *Cold Work-Hardening in Stage-Iv and Stage-V of Fcc Metals .1. Experiments and Interpretation*. Acta Metallurgica Et Materialia 1993;41:577-588.
[54] Wang YM, Ma E. *Strain hardening, strain rate sensitivity, and ductility of nanostructured metals*. Materials Science and Engineering a-Structural Materials Properties Microstructure and Processing 2004;375-77:46-52.
[55] Jia D, Ramesh KT, Ma E, Lu L, Lu K. *Compressive Behavior of an Electrodeposited Nanostructured Copper at Quaisstatic and High Strain Rates*. Scripta Materialia 2001;24:613-620.
[56] Lu L, Wang LB, Ding BZ, Lu K. *High-Tensile Ductility in Nanocrystalline Copper*. Journal of Materials Research 2000;15:270-273.
[57] Schuster BE, Wei Q, Zhang H, Ramesh KT. *Microcompression of nanocrystalline nickel*. Applied Physics Letters 2006;88:103112.
[58] Zhang X, Wang H, Narayan J, Koch CC. *Evidence for the formation mechanism of nanoscale microstructures in cryomilled Zn powder*. Acta Materialia 2001;49:1319-1326.
[59] Zhang X, Wang H, Scattergood RO, Narayan J, Koch CC. *Mechanical properties of cyromilled nanocrystalline Zn studied by the miniaturized disk bend test*. Acta Materialia 2002;50:3527-3533.
[60] Wang YM, Cheng S, Wei QM, Ma E, Nieh TG, Hamza A. *Effects of annealing and impurities on tensile properties of electrodeposited nanocrystalline Ni*. Scripta Materialia 2004;51:1023-1028.

[61] Asaro RJ, Suresh S. *Mechanistic models for the activation volume and rate sensitivity in metals with nanocrystalline grains and nano-scale twins*. Acta Materialia 2005;53:3369-3382.
[62] Wei Q, Cheng S, Ramesh KT, Ma E. *Effect of nanocrystalline and ultrafine grain sizes on the strain rate sensitivity and activation volume: fcc versus bcc metals*. Materials Science and Engineering a-Structural Materials Properties Microstructure and Processing 2004;381:71-79.
[63] Lund AC, Schuh CA. *Strength Asymmetry in Nanocrystalline Metals Under Multiaxial Loading*. Acta Materialia 2005;53:3193-3205.
[64] Donovan PE. *A Yield Criterion for Pd40ni40p20 Metallic-Glass*. Acta Metallurgica 1989;37:445-456.
[65] Lund AC, Schuh CA. *Yield Surface of a Simulated Metallic Glass*. Acta Materialia 2003;51:5399-5411.
[66] Carlton CE, Ferreira PJ. *What is behind the inverse Hall-Petch effect in nanocrystalline materials?* Acta Materialia 2007;55:3749-3756.
[67] Carlton CE, Ferreira PJ. *Dislocation motion-induced strain in nanocrystalline materials: Overlooked considerations*. Materials Science and Engineering a-Structural Materials Properties Microstructure and Processing 2008;486:672-674.
[68] Cheng S, Spencer JA, Milligan WW. *Strength and Tension/Compression Asymmetry in Nanostructured and Ultrafine Grain Metals*. Acta Materialia 2003;51:4505-4518.
[69] Conrad H, Jung K. *Effects of grain size from millimeters to nanometers on the flow stress of metals and compounds*. Journal of Electronic Materials 2006;35:857-861.
[70] Zhu YT, Langdon TG. *Influence of grain size on deformation mechanisms: An extension to nanocrystalline materials*. Materials Science and Engineering a-Structural Materials Properties Microstructure and Processing 2005;409:234-242.
[71] Bobylev SV, Gutkin MY, Ovid'ko IA. *Generation of glide split-dislocation half-loops by grain boundaries in nanocrystalline Al*. Physics of the Solid State 2006;48:1495-1505.
[72] Tang F, Schoenung JM. *Strain softening in nanocrystalline or ultrafine-grained metals: A mechanistic explanation*. Materials Science and Engineering a-Structural Materials Properties Microstructure and Processing in press (2008).
[73] Jung J. *A Note on the Influence of Hydrostatic-Pressure on Dislocations*. Philosophical Magazine a-Physics of Condensed Matter Structure Defects and Mechanical Properties 1981;43:1057-1061.
[74] Nieh TG, Wadsworth J. *Hall-Petch Relation in Nanocrystalline Solids*. Scripta Metallurgica Et Materialia 1991;25:955-958.
[75] Chokshi AH, Rosen A, Karch J, Gleiter H. *On the Validity of the Hall-Petch Relationship in Nanocrystalline Materials*. Scripta Metallurgica 1989;23:1679-1683.
[76] Conrad H. *Grain-size dependence of millimeters to nanometers*. Metallurgical and Materials Transactions a-Physical Metallurgy and Materials Science 2004;35A:2681-2695.
[77] Detor AJ, Schuh CA. *Tailoring and patterning the grain size of nanocrystalline alloys*. Acta Materialia 2007;55:371-379.
[78] Giga A, Kimoto Y, Takigawa Y, Higashi K. *Demonstration of an inverse Hall-Petch relationship in electrodeposited nanocrystalline Ni-W alloys through tensile testing*. Scripta Materialia 2006;55:143-146.
[79] Jang D, Atzmon M. *Grain-size dependence of plastic deformation in nanocrystalline Fe*. Journal of Applied Physics 2003;93:9282-9286.
[80] Koch CC, Narayan J. *The Inverse Hall-Petch Effect- Fact or Artifact?* Materials Research Society Proceedings 2001;634:B5.1.1-B5.1.11.

[81] Schiotz J, Jacobsen KW. *A maximum in the strength of nanocrystalline copper.* Science 2003;301:1357-1359.
[82] Schuh CA, Nieh TG, Iwasaki H. *The effect of solid solution W additions on the mechanical properties of nanocrystalline Ni.* Acta Materialia 2003;51:431-443.
[83] Schuh CA, Nieh TG, Yamasaki T. *Hall-Petch breakdown manifested in abrasive wear resistance of nanocrystalline nickel.* 2002;46:735-740.
[84] Argon AS, Yip S. *The strongest size.* Philosophical Magazine Letters 2006;86:713-720.
[85] Yip S. *Nanocrystals - The strongest size.* Nature 1998;391:532-533.
[86] Asaro RJ, Krysl P, Kad B. *Deformation mechanism transitions in nanoscale fcc metals.* Philosophical Magazine Letters 2003;83:733-743.
[87] Van Swygenhoven H, Derlet PM, Budrovic Z, Hasnaoui A. *Unconventional deformation mechanism in nanocrystalline metals?* Zeitschrift Fur Metallkunde 2003;94:1106-1110.
[88] Van Swygenhoven H, Spaczer M, Caro A, Farkas D. *Competing plastic deformation mechanisms in nanophase metals.* Physical Review B 1999;60:22-25.
[89] Wolf D, Yamakov V, Phillpot SR, Mukherjee AK. *Deformation mechanism and inverse Hall-Petch behavior in nanocrystalline materials.* Zeitschrift Fur Metallkunde 2003;94:1091-1097.
[90] Yamakov V, Wolf D, Phillpot SR, Mukherjee AK, Gleiter H. *Deformation mechanism crossover and mechanical behaviour in nanocrystalline materials.* Philosophical Magazine Letters 2003;83:385-393.
[91] Wei YJ, Su C, Anand L. *A computational study of the mechanical behavior of nanocrystalline fcc metals.* Acta Materialia 2006;54:3177-3190.
[92] Schiotz J, Vegge T, Di Tolla FD, Jacobsen KW. *Atomic-scale simulations of the mechanical deformation of nanocrystalline metals.* Physical Review B 1999;60:11971-11983.
[93] Farkas D, Froseth A, Van Swygenhoven H. *Grain boundary migration during room temperature deformation of nanocrystalline Ni.* Scripta Materialia 2006;55:695-698.
[94] Schiotz J. *Atomic-scale modeling of plastic deformation of nanocrystalline copper.* Scripta Materialia 2004;51:837-841.
[95] Van Swygenhoven H, Derlet PA. *Grain-boundary sliding in nanocrystalline fcc metals.* Physical Review B 2001;64:-.
[96] Monk J, Hyde B, Farkas D. *The role of partial grain boundary dislocations in grain boundary sliding and coupled grain boundary motion.* Journal of Materials Science 2006;41:7741-7746.
[97] Farkas D, Mohanty S, Monk J. *Strain-driven Grain Boundary Motion in Nanocrystalline Materials.* Materials Science and Engineering a-Structural Materials Properties Microstructure and Processing in press (2008).
[98] Conrad H, Narayan J. *On the grain size softening in nanocrystalline materials.* Scripta Materialia 2000;42:1025-1030.
[99] Zhu B, Asaro RJ, Krysl P, Bailey R. *Transition of deformation mechanisms and its connection to grain size distribution in nanocrystalline metals.* Acta Materialia 2005;53:4825-4838.
[100] Zhu B, Asaro RJ, Krysl P, Zhang K, Weertman JR. *Effects of grain size distribution on the mechanical response of nanocrystalline metals: Part II.* Acta Materialia 2006;54:3307-3320.
[101] Mohamed FA. *Interpretation of nanoscale softening in terms of dislocation-accommodated boundary sliding.* Metallurgical and Materials Transactions a-Physical Metallurgy and Materials Science 2007;38A:340-347.

[102] Mohamed FA. *Correlation between the deformation of nanostructured materials and the model of dislocation accommodated boundary sliding.* Metallurgical and Materials Transactions a-Physical Metallurgy and Materials Science 2008;39A:470-472.
[103] Schuh CA, Hufnagel TC, Ramamurty U. *Overview No.144 - Mechanical behavior of amorphous alloys.* 2007;55:4067-4109.
[104] Argon AS. *Plastic-Deformation in Metallic Glasses.* Acta Metallurgica 1979;27:47-58.
[105] Jiang WH, Pinkerton FE, Atzmon M. *Mechanical behavior of shear bands and the effect of their relaxation in a rolled amorphous Al-based alloy.* Acta Materialia 2005;53:3469-3477.
[106] Lee JY, Han KH, Park JM, Chattopadhyay K, Kim WT, Kim DH. *Deformation and evolution of shear bands under compressive loading in bulk metallic glasses.* Acta Materialia 2006;54:5271-5279.
[107] Mukai T, Nieh TG, Kawamura Y, Inoue A, Higashi K. *Effect of strain rate on compressive behavior of a Pd40Ni40P20 bulk metallic glass.* Intermetallics 2002;10:1071-1077.
[108] Packard CE, Schuh CA. *Initiation of shear bands near a stress concentration in metallic glass.* Acta Materialia 2007;55:5348-5358.
[109] Schuh CA, Nieh TG. *A nanoindentation study of serrated flow in bulk metallic glasses.* Acta Materialia 2003;51:87-99.
[110] Spaepen F. *Microscopic Mechanism for Steady-State Inhomogeneous Flow in Metallic Glasses.* Acta Metallurgica 1977;25:407-415.
[111] Yang B, Nieh TG. *Effect of the nanoindentation rate on the shear band formation in an Au-based bulk metallic glass.* Acta Materialia 2007;55:295-300.
[112] Joshi SP, Ramesh KT. *Stability map for nanocrystalline and amorphous materials.* Physical Review Letters 2008;101:-.
[113] Joshi SP, Ramesh KT. *Rotational diffusion and grain size dependent shear instability in nanostructured materials.* Acta Materialia 2008;56:282-291.
[114] Joshi SP, Ramesh KT. *Grain size dependent shear instabilities in body-centered and face-centered cubic materials.* Materials Science and Engineering a-Structural Materials Properties Microstructure and Processing in press (2008).
[115] Benson DJ, Fu HH, Meyers MA. *On the effect of grain size on yield stress: extension into nanocrystalline domain.* Materials Science and Engineering a-Structural Materials Properties Microstructure and Processing 2001;319:854-861.
[116] Fu HH, Benson DJ, Meyers MA. *Analytical and computational description of effect of grain size on yield stress of metals.* Acta Materialia 2001;49:2567-2582.
[117] Fu HH, Benson DJ, Meyers MA. *Computational description of nanocrystalline deformation based on crystal plasticity.* Acta Materialia 2004;52:4413-4425.
[118] Xiang Q, Guo XM. *The scale effect on the yield strength of nanocrystalline materials.* International Journal of Solids and Structures 2006;43:7793-7799.
[119] Fan GJ, Choo H, Liaw PK, Lavernia EJ. *A model for the inverse Hall-Petch relation of nanocrystalline materials.* Materials Science and Engineering a-Structural Materials Properties Microstructure and Processing 2005;409:243-248.
[120] Jiang B, Weng GJ. *A composite model for the grain-size dependence of yield stress of nanograined materials.* Metallurgical and Materials Transactions a-Physical Metallurgy and Materials Science 2003;34A:765-772.
[121] Jiang B, Weng GJ. *A generalized self-consistent polycrystal model for the yield strength of nanocrystalline materials.* Journal of the Mechanics and Physics of Solids 2004;52:1125-1149.

[122] Kim HS, Estrin Y. *Phase mixture modeling of the strain rate dependent mechanical behavior of nanostructured materials*. Acta Materialia 2005;53:765-772.
[123] Lebensohn RA, Bringa EM, Caro A. *A viscoplastic micromechanical model for the yield strength of nanocrystalline materials*. Acta Materialia 2007;55:261-271.
[124] Warner DH, Molinari JF. *A semi-discrete and non-local crystal plasticity model for nanocrystalline metals*. Scripta Materialia 2006;54:1397-1402.
[125] Kim HS. *A composite model for mechanical properties of nanocrystalline materials*. Scripta Materialia 1998;39:1057-1061.
[126] Derlet PM, Hasnaoui A, Van Swygenhoven H. *Atomistic simulations as guidance to experiments*. Scripta Materialia 2003;49:629-635.
[127] Keblinski P, Phillpot SR, Wolf D, Gleiter H. *Relationship between nanocrystalline and amorphous microstructures by molecular dynamics simulation*. Nanostructured Materials 1997;9:651-660.
[128] Phillpot SR, Wang J, Wolf D, Gleiter H. *Computer simulation of the structure and dynamical properties of grain boundaries in a nanocrystalline model material*. Materials Science and Engineering a-Structural Materials Properties Microstructure and Processing 1995;204:76-82.
[129] Van Swygenhoven H, Caro A. *Plastic behavior of nanophase metals studied by molecular dynamics*. 1998;58:11246-11251.
[130] Van Swygenhoven H, Derlet PM, Hasnaoui A. *Atomistic modeling of strength of nanocrystalline metals*. Advanced Engineering Materials 2003;5:345-350.
[131] Wolf D, Yamakov V, Phillpot SR, Mukherjee A, Gleiter H. *Deformation of nanocrystalline materials by molecular-dynamics simulation: relationship to experiments?* Acta Materialia 2005;53:1-40.
[132] Shen TD, Schwarz RB, Feng S, Swadener JG, Huang JY, Tang M, Zhang H, Vogel SC, Zhao YS. *Effect of solute segregation on the strength of nanocrystalline alloys: Inverse Hall-Petch relation*. Acta Materialia 2007;55:5007-5013.
[133] Detor AJ, Schuh CA. *Microstructural evolution during the heat treatment of nanocrystalline alloys*. Journal of Materials Research 2007;22:3233-3248.
[134] Gutkin MY, Ovid'ko IA, Pande CS. Yield stress of nanocrystalline materials: role of grain-boundary dislocations, triple junctions and Coble creep. vol. 84: Taylor & Francis, 2004. p.847 - 863.
[135] Hwang WS, Lee JJ. *Effects of heat treatment on hardness of nanocrystalline Ni-W electrodeposits*. Eco-Materials Processing & Design Vii 2006;510-511:1126-1129.
[136] Volpp T, Goring E, Kuschke WM, Arzt E. *Grain size determination and limits to Hall-Petch behavior in nanocrystalline NiAl powders*. Nanostructured Materials 1997;8:855-865.
[137] Sanders PG, Weertman JR. *Plastic deformation of nanocrystalline metals*. Solid State Phenomena 1994;35-36:249-262.
[138] da Silva M, Klement U. *A comparison of thermal stability in nanocrystalline Ni- and Co-based materials*. Zeitschrift Fur Metallkunde 2005;96:1009-1014.
[139] Hibbard G, Aust KT, Palumbo G, Erb U. *Thermal stability of electrodeposited nanocrystalline cobalt*. Scripta Materialia 2001;44:513-518.
[140] Hibbard G, Erb U, Aust KT, Klement U, Palumbo G. *Thermal stability of nanostructured electrodeposits*. Metastable, Mechanically Alloyed and Nanocrystalline Materials 2002;386-3:387-396.

[141] Klement U, Da Silva M. *Thermal stability of electrodeposited nanocrystalline Ni- and Co-based materials*. Journal of Iron and Steel Research International 2007;14:173-178.
[142] Klement U, Erb U, ElSherik AM, Aust KT. *Thermal stability of nanocrystalline Ni*. Materials Science and Engineering a-Structural Materials Properties Microstructure and Processing 1995;203:177-186.
[143] Choi P, da Silva M, Klement U, Al-Kassab T, Kirchheim R. *Thermal stability of electrodeposited nanocrystalline Co-1.1at.%P*. Acta Materialia 2005;53:4473-4481.
[144] Hentschel T, Isheim D, Kirchheim R, Muller F, Kreye H. *Nanocrystalline Ni-3.6 at.% P and its transformation sequence studied by atom-probe field-ion microscopy*. Acta Materialia 2000;48:933-941.
[145] Gleiter H. *Nanostructured materials: State of the art and perspectives*. Nanostructured Materials 1995;6:3-14.
[146] Hasnaoui A, Van Swygenhoven H, Derlet PM. *On non-equilibrium grain boundaries and their effect on thermal and mechanical behaviour: a molecular dynamics computer simulation*. Acta Materialia 2002;50:3927-3939.
[147] Sanders PG, Fougere GE, Thompson LJ, Eastman JA, Weertman JR. *Improvements in the synthesis and compaction of nanocrystalline materials*. Nanostructured Materials 1997;8:243-252.
[148] Zhang XH, Wang HY, Kassem M, Narayan J, Koch CC. *Origins of stored enthalpy in cryomilled nanocrystalline Zn*. Journal of Materials Research 2001;16:3485-3495.
[149] Masumura RA, Hazzledine PM, Pande CS. *Yield stress of fine grained materials*. Acta Materialia 1998;46:4527-4534.
[150] Cheng S, Spencer JA, Milligan WW. *Strength and tension/compression asymmetry in nanostructured and ultrafine-grain metals*. Acta Materialia 2003;51:4505-4518.
[151] Koch C. *Top-down synthesis of nanostructured materials: Mechanical and Thermal Processing Methods*. Rev. Adv. Mater. Sci. 2003;5:91-99.
[152] Valiev RZ, Islamgaliev RK, Alexandrov IV. *Bulk nanostructured materials from severe plastic deformation*. Progress in Materials Science 2000;45:103-189.
[153] Koch CC. *Synthesis of nanostructured materials by mechanical milling: Problems and opportunities*. Nanostructured Materials 1997;9:13-22.
[154] Malow TR, Koch CC. *Grain growth in nanocrystalline iron prepared by mechanical attrition*. Acta Materialia 1997;45:2177-2186.
[155] Iyer RS, Sastry SML. *Consolidation of nanoparticles - Development of a micromechanistic model*. Acta Materialia 1999;47:3079-3098.
[156] Lu L, Shen YF, Chen XH, Qian LH, Lu K. *Ultrahigh strength and high electrical conductivity in copper*. Science 2004;304:422-426.
[157] Elsherik AM, Erb U. *Synthesis of Bulk Nanocrystalline Nickel by Pulsed Electrodeposition*. Journal of Materials Science 1995;30:5743-5749.
[158] Ebrahimi F, Ahmed Z. *The effect of current density on properties of electrodeposited nanocrystalline nickel*. Journal of Applied Electrochemistry 2003;33:733-739.
[159] Natter H, Schmelzer M, Hempelmann R. *Nanocrystalline Nickel and Nickel-Copper Alloys: Synthesis, Characterization, and Thermal Stability*. Journal of Materials Research 1998;13:1186-1197.
[160] Robertson A, Erb U, Palumbo G. *Practical applications for electrodeposited nanocrystalline materials*. Nanostructured Materials 1999;12:1035-1040.

[161] Bakonyi I, TothKadar E, Pogany L, Cziraki A, Gerocs I, VargaJosepovits K, Arnold B, Wetzig K. *Preparation and characterization of dc-plated nanocrystalline nickel electrodeposits.* Surface & Coatings Technology 1996;78:124-136.
[162] Choo RTC, Toguri JM, Elsherik AM, Erb U. *Mass-Transfer and Electrocrystallization Analyses of Nanocrystalline Nickel Production by Pulse Plating.* Journal of Applied Electrochemistry 1995;25:384-403.
[163] Qu NS, Zhu D, Chan KC, Lei WN. *Pulse electrodeposition of nanocrystalline nickel using ultra narrow pulse width and high peak current density.* Surface & Coatings Technology 2003;168:123-128.
[164] Haber JA, Buhro WE. *Kinetic instability of nanocrystalline aluminum prepared by chemical synthesis; Facile room-temperature grain growth.* Journal of the American Chemical Society 1998;120:10847-10855.
[165] Zhou F, Lee J, Lavernia EJ. *Grain growth kinetics of a mechanically milled nanocrystalline Al.* Scripta Materialia 2001;44:2013-2017.
[166] Joshi N, Aswal DK, Debnath AK, Gupta SK, Yakhmi JV. *Growth of nanocrystalline Pd films on Si(111).* Applied Surface Science 2004;228:302-305.
[167] Pande CS, Masumura RA. *Grain growth and deformation in nanocrystalline materials.* Materials Science and Engineering a-Structural Materials Properties Microstructure and Processing 2005;409:125-130.
[168] Birringer R. *Nanocrystalline Materials.* Materials Science and Engineering a-Structural Materials Properties Microstructure and Processing 1989;117:33-43.
[169] Gunther B, Kumpmann A, Kunze HD. *Secondary Recrystallization Effects in Nanostructured Elemental Metals.* Scripta Metallurgica et Materialia 1992;27:833-838.
[170] Malow TR, Koch CC. *Thermal stability of nanocrystalline materials.* Metastable, Mechanically Alloyed and Nanocrystalline Materials, Pts 1 and 2 1996;225:595-604.
[171] Ebrahimi F, Li HQ. *Grain growth in electrodeposited nanocrystalline fcc Ni-Fe alloys.* Scripta Materialia 2006;55:263-266.
[172] Hibbard GD, Aust KT, Erb U. *Thermal stability of electrodeposited nanocrystalline Ni-Co alloys.* Materials Science and Engineering a-Structural Materials Properties Microstructure and Processing 2006;433:195-202.
[173] Li HQ, Ebrahimi F. *An investigation of thermal stability and microhardness of electrodeposited nanocrystalline nickel-21% iron alloys.* Acta Materialia 2003;51:3905-3913.
[174] Humphreys FJ, Hatherly M. Recrystallization and related annealing phenomena. Tarrytown, NY: Pergamon, 1995.
[175] Kirchheim R. *Grain coarsening inhibited by solute segregation.* Acta Materialia 2002;50:413-419.
[176] Krill CE, Ehrhardt H, Birringer R. *Thermodynamic stabilization of nanocrystallinity.* Zeitschrift Fur Metallkunde 2005;96:1134-1141.
[177] Weissmuller J. *Alloy effects in nanostructures.* Nanostructured Materials 1993;3:261-272.
[178] Weissmuller J. *Alloy Thermodynamics in Nanostructures.* Journal of Materials Research 1994;9:4-7.
[179] Weissmuller J. *Some Basic Notions on Nanostructured Solids.* 1994;179:102-107.
[180] Sutton AP, Balluffi RW. Interfaces in crystalline materials. Oxford: Clarendon, 1995.
[181] Millett PC, Selvam RP, Saxena A. *Stabilizing nanocrystalline materials with dopants.* Acta Materialia 2007;55:2329-2336.

[182] Weissmuller J, Krauss W, Haubold T, Birringer R, Gleiter H, . *Atomic structure and thermal stability of nanostructured Y-Fe alloys*. Nanostructured Materials 1992;1:439-447.
[183] Liu F, Kirchheim R. *Nano-scale grain growth inhibited by reducing grain boundary energy through solute segregation*. Journal of Crystal Growth 2004;264:385-391.
[184] Liu F, Kirchheim R. *Grain boundary saturation and grain growth*. Scripta Materialia 2004;51:521-525.
[185] Darling KA, Chan RN, Wong PZ, Semones JE, Scattergood RO, Koch CC. *Grain-size Stabilization in Nanocrystalline FeZr Alloys*. Scripta Materialia 2008;59:530-533.
[186] Schlossmacher P, Yamasaki T. *Structural analysis of electroplated amorphous-nanocrystalline Ni-W*. Mikrochimica Acta 2000;132:309-313.
[187] Yamasaki T, Schlossmacher P, Ehrlich K, Ogino Y. *Formation of amorphous electrodeposited Ni-W alloys and their nanocrystallization*. Nanostructured Materials 1998;10:375-388.
[188] Yamasaki T, Tomohira R, Ogino Y, Schlossmacher P, Ehrlich K. *Formation of ductile amorphous & nanocrystalline Ni-W alloys by electrodeposition*. Plating and Surface Finishing 2000;87:148-152.
[189] Li HQ, Ebrahimi F. *Synthesis and characterization of electrodeposited nanocrystalline nickel-iron alloys*. Materials Science and Engineering a-Structural Materials Properties Microstructure and Processing 2003;347:93-101.
[190] Detor AJ, Miller MK, Schuh CA. *Solute distribution in nanocrystalline Ni-W alloys examined through atom probe tomography*. Philosophical Magazine 2006;86:4459-4475.
[191] Farber B, Cadel E, Menand A, Schmitz G, Kirchheim R. *Phosphorus segregation in nanocrystalline Ni-3.6 at.% P alloy investigated with the tomographic atom probe (TAP)*. Acta Materialia 2000;48:789-796.
[192] Millett PC, Selvan RP, Bansal S, Saxena A. *Atomistic simulation of grain boundary energetics - Effects of dopants*. Acta Materialia 2005;53:3671-3678.
[193] Millett PC, Selvam RP, Saxena A. *Molecular dynamics simulations of grain size stabilization in nanocrystalline materials by addition of dopants*. Acta Materialia 2006;54:297-303.
[194] Detor AJ, Schuh CA. *Grain boundary segregation, chemical ordering and stability of nanocrystalline alloys: Atomistic computer simulations in the Ni–W system*. Acta Materialia 2007;55:4221.
[195] Ishida K. *Effect of grain size on grain boundary segregation*. Journal of Alloys and Compounds 1996;235:244-249.
[196] Meng QP, Rong YH, Hsu TY. *Distribution of solute atoms in nanocrystalline materials*. Materials Science and Engineering a-Structural Materials Properties Microstructure and Processing 2007;471:22-27.
[197] Swaminarayan S, Srolovitz DJ. *Surface segregation in thin films*. Acta Materialia 1996;44:2067-2072.
[198] Beke DL, Cserhati C, Szabo IA. *Segregation inhibited grain coarsening in nanocrystalline alloys*. Journal of Applied Physics 2004;95:4996-5001.
[199] Cserhati C, Szabo IA, Beke DL. *Size effects in surface segregation*. Journal of Applied Physics 1998;83:3021-3027.
[200] Hellman OC, Seidman DN. *Measurement of the Gibbsian interfacial excess of solute at an interface of arbitrary geometry using three-dimensional atom probe microscopy*. Materials

Science and Engineering a-Structural Materials Properties Microstructure and Processing 2002;327:24-28.
[201] Miedema AR. *Heat of Formation of Alloys*. Philips Technical Review 1976;36:217-231.
[202] Miedema AR. *Heat of Formation of Solid Alloys .2.* Journal of the Less-Common Metals 1976;46:67-83.
[203] Miedema AR, Boom R, Deboer FR. *Heat of Formation of Solid Alloys*. Journal of the Less-Common Metals 1975;41:283-298.
[204] Atanassov N, Gencheva K, Bratoeva M. *Properties of nickel-tungsten alloys electrodeposited from sulfamate electrolyte*. Plating and Surface Finishing 1997;84:67-71.
[205] Iwasaki H, Higashi K, Nieh TG. *Tensile deformation and microstructure of a nanocrystalline Ni-W alloy produced by electrodeposition*. Scripta Materialia 2004;50:395-399.
[206] Nasu T, Sakurai M, Kamiyama T, Usuki T, Tokumitsu K, Yamasaki T. *Microstructure of M-W (M=Fe, Ni) alloys produced by electrodeposition and mechanical alloying*. Thermec'2003, Pts 1-5 2003;426-4:4585-4590.
[207] Nasu T, Sakurai M, Kamiyama T, Usuki T, Uemura O, Tokumitsu K, Yamasaki T. *Structural comparison of M-W (M = Fe, Ni) alloys produced by electrodeposition and mechanical alloying*. Materials Science and Engineering a-Structural Materials Properties Microstructure and Processing 2004;375-77:163-170.
[208] Nasu T, Sakurai M, Kamiyama T, Usuki T, Uemura O, Yamasaki T. *EXAFS study on amorphous and nanocrystalline M-W (M=Fe, Ni) alloys produced by electrodeposition*. Journal of Non-Crystalline Solids 2002;312:319-322.
[209] Obradovic MD, Bosnjakov GZ, Stevanovic RM, Maksimovic MD, Despic AR. *Pulse and direct current plating of Ni-W alloys from ammonia-citrate electrolyte*. Surface & Coatings Technology 2006;200:4201-4207.
[210] Obradovic MD, Stevanovic RM, Despic AR. *Electrochemical deposition of Ni-W alloys from ammonia-citrate electrolyte*. Journal of Electroanalytical Chemistry 2003;552:185-196.
[211] Wu YY, Chang DY, Kim DS, Kwon SC. *Influence of boric acid on the electrodepositing process and structures of Ni-W alloy coating*. Surface & Coatings Technology 2003;173:259-264.
[212] Wu YY, Chang DY, Kim DS, Kwon SC. *Effects of 2-butyne-1,4-diol on structures and morphologies of electroplating Ni-W alloy*. Surface & Coatings Technology 2003;162:269-275.
[213] Wu YY, Chang DY, Kwon SC, Kim D. *Ni-W alloy electrodeposition from a bath containing an organic amine substitute for inorganic ammonia*. Plating and Surface Finishing 2003;90:46-49.
[214] Younes O, Gileadi E. *Electroplating of high tungsten content Ni/W alloys*. Electrochemical and Solid State Letters 2000;3:543-545.
[215] Younes O, Gileadi E. *Electroplating of Ni/W alloys - I. Ammoniacal citrate baths*. Journal of the Electrochemical Society 2002;149:C100-C111.
[216] Younes O, Zhu L, Rosenberg Y, Shacham-Diamand Y, Gileadi E. *Electroplating of amorphous thin films of tungsten/nickel alloys*. Langmuir 2001;17:8270-8275.
[217] Younes-Metzler O, Zhu L, Gileadi E. *The anomalous codeposition of tungsten in the presence of nickel*. Electrochimica Acta 2003;48:2551-2562.
[218] Zhu L, Younes O, Ashkenasy N, Shacham-Diamand Y, Gileadi E. *STM/AFM studies of the evolution of morphology of electroplated Ni/W alloys*. Applied Surface Science 2002;200:1-14.

[219] Hwang WS, Cho WS. *The effect of tungsten content on nanocrystalline structure of Ni-W alloy electrodeposits*. Eco-Materials Processing & Design Vii 2006;510-511:1062-1065.
[220] Franz S, Marlot A, Cavallotti PL, Landolt D. *Pulse plating of Ni-W alloys from model electrolytes*. Transactions of the Institute of Metal Finishing 2008;86:92-97.
[221] Zhang Z, Zhou F, Lavernia EJ. *On the analysis of grain size in bulk nanocrystalline materials via X-ray diffraction*. Metallurgical and Materials Transactions a-Physical Metallurgy and Materials Science 2003;34A:1349-1355.
[222] Chassaing E, Roumegas MP, Trichet MF. *Electrodeposition of Ni-Mo Alloys with Pulse Reverse Potentials*. Journal of Applied Electrochemistry 1995;25:667-670.
[223] Landolt D, Marlot A. *Microstructure and composition of pulse-plated metals and alloys*. Surface & Coatings Technology 2003;169:8-13.
[224] Marlot A, Kern P, Landolt D. *Pulse plating of Ni-Mo alloys from Ni-rich electrolytes*. Electrochimica Acta 2002;48:29-36.
[225] Bradley P, Roy S, Landolt D. *Pulse-plating of copper-nickel alloys from a sulfamate solution*. Journal of the Chemical Society-Faraday Transactions 1996;92:4015-4019.
[226] Bradley PE, Janossy B, Landolt D. *Pulse plating of cobalt-iron-copper alloys*. Journal of Applied Electrochemistry 2001;31:137-144.
[227] Bradley PE, Landolt D. *A surface coverage model for pulse-plating of binary alloys exhibiting a displacement reaction*. Electrochimica Acta 1997;42:993-1003.
[228] Bradley PE, Landolt D. *Pulse-plating of copper-cobalt alloys*. Electrochimica Acta 1999;45:1077-1087.
[229] Gianola DS, Van Petegem S, Legros M, Brandstetter S, Van Swygenhoven H, Hemker KJ. *Stress-assisted discontinuous grain growth and its effect on the deformation behavior of nanocrystalline aluminum thin films*. Acta Materialia 2006;54:2253-2263.
[230] Gianola DS, Warner DH, Molinari JF, Hemker KJ. *Increased strain rate sensitivity due to stress-coupled grain growth in nanocrystalline Al*. Scripta Materialia 2006;55:649-652.
[231] Zhang K, Weertman JR, Eastman JA. *Rapid stress-driven grain coarsening in nanocrystalline Cu at ambient and cryogenic temperatures*. Applied Physics Letters 2005;87:-.
[232] Jin M, Minor AM, Ge D, Morris JW. *Study of deformation behavior of ultrafine-grained materials through in situ nanoindentation in a transmission electron microscope*. Journal of Materials Research 2005;20:1735-1740.
[233] Wang YB, Li BQ, Sui ML, Mao SX. *Deformation-induced grain rotation and growth in nanocrystalline Ni*. Applied Physics Letters 2008;92:-.
[234] Wang YM, Bringa EM, Victoria M, Carol A, McNaney JM, Smith R, Remington BA. *Deformation of nanocrystalline materials at ultrahigh strain rates - microstructure perspective in nanocrystalline nickel*. Journal De Physique Iv 2006;134:915-920.
[235] Brandstetter S, Zhang K, Escuadro A, Weertman JR, Van Swygenhoven H. *Grain coarsening during compression of bulk nanocrystalline nickel and copper*. Scripta Materialia 2008;58:61-64.
[236] Fan GJ, Fu LF, Qiao DC, Choo H, Liaw PK, Browning ND. *Grain growth in a bulk nanocrystalline Co alloy during tensile plastic deformation*. Scripta Materialia 2006;54:2137-2141.
[237] Schiotz J. *Strain-induced coarsening in nanocrystalline metals under cyclic deformation*. Materials Science and Engineering a-Structural Materials Properties Microstructure and Processing 2004;375-77:975-979.

[238] Haslam AJ, Moldovan D, Yamakov V, Wolf D, Phillpot SR, Gleiter H. *Stress-enhanced grain growth in a nanocrystalline material by molecular-dynamics simulation.* Acta Materialia 2003;51:2097-2112.
[239] Fan GJ, Fu LF, Choo H, Liaw PK, Browning ND. *Uniaxial tensile plastic deformation and grain growth of bulk nanocrystalline alloys.* Acta Materialia 2006;54:4781-4792.
[240] Fan GJ, Wang YD, Fu LF, Choo H, Liaw PK, Ren Y, Browning ND. *Orientation-dependent grain growth in a bulk nanocrystalline alloy during the uniaxial compressive deformation.* Applied Physics Letters 2006;88:-.
[241] Trelewicz JR, Schuh CA. *The Hall-Petch breakdown in nanocrystalline metals: A crossover to glass-like deformation.* Acta Materialia 2007;55:5948-5958.
[242] Oliver WC, Pharr GM. *Measurement of hardness and elastic modulus by instrumented indentation: Advances in understanding and refinements to methodology.* Journal of Materials Research 2004;19:3-20.
[243] Lucas BN, Oliver WC. *Indentation power-law creep of high-purity indium.* Metallurgical and Materials Transactions a-Physical Metallurgy and Materials Science 1999;30:601-610.
[244] Mukai T, Nieh TG, Kawamura Y, Inoue A, Higashi K. *Dynamic response of a Pd40Ni40P20 bulk metallic glass in tension.* Scripta Materialia 2002;46:43-47.
[245] Jiang WH, Atzmon M. *Rate dependence of serrated flow in a metallic glass.* Journal of Materials Research 2003;18:755-757.
[246] Schwaiger R, Moser B, Dao M, Chollacoop N, Suresh S. *Some critical experiments on the strain-rate sensitivity of nanocrystalline nickel.* Acta Materialia 2003;51:5159-5172.
[247] Wang YM, Ma E. *On the origin of ultrahigh cryogenic strength of nanocrystalline metals.* Applied Physics Letters 2004;85:2750-2752.
[248] McNaney JM, Imbeni V, Jung Y, Papadopoulos P, Ritchie RO. *An experimental study of the superelastic effect in a shape-memory Nitinol alloy under biaxial loading.* Mechanics of Materials 2003;35:969-986.
[249] Green DE, Neale KW, MacEwen SR, Makinde A, Perrin R. *Experimental investigation of the biaxial behaviour of an aluminum sheet.* International Journal of Plasticity 2004;20:1677-1706.
[250] Hoferlin E, Van Bael A, Van Houtte P, Steyaert G, De Mare C. *The design of a biaxial tensile test and its use for the validation of crystallographic yield loci.* Modelling and Simulation in Materials Science and Engineering 2000;8:423-433.
[251] Ganneau FP, Constantinides G, Ulm FJ. *Dual-indentation technique for the assessment of strength properties of cohesive-frictional materials.* International Journal of Solids and Structures 2006;43:1727-1745.
[252] Bringa EM, Caro A, Leveugle E. *Pressure effects on grain boundary plasticity in nanophase metals.* Applied Physics Letters 2006;89:-.
[253] Bringa EM, Caro A, Wang YM, Victoria M, McNaney JM, Remington BA, Smith RF, Torralva BR, Van Swygenhoven H. *Ultrahigh strength in nanocrystalline materials under shock loading.* Science 2005;309:1838-1841.
[254] Bringa EM, Rosolankova K, Rudd RE, Remington BA, Wark JS, Duchaineau M, Kalantar H, Hawreliak J, Belak J. *Shock deformation of face-centred-cubic metals on subnanosecond timescales.* Nature Materials 2006;5:805-809.
[255] Wang YM, Bringa EM, McNaney JM, Victoria M, Caro A, Hodge AM, Smith R, Torralva B, Remington BA, Schuh CA, Jamarkani H, Meyers MA. *Deforming nanocrystalline nickel at ultrahigh strain rates.* Applied Physics Letters 2006;88:061917.

[256] Wu XL, Qi Y, Zhu YT. *Partial-mediated slips in nanocrystalline Ni at high strain rate.* Applied Physics Letters 2007;90:-.
[257] Khan AS, Suh YS, Chen X, Takacs L, Zhang HY. *Nanocrystalline aluminum and iron: Mechanical behavior at quasi-static and high strain rates, and constitutive modeling.* International Journal of Plasticity 2006;22:195-209.
[258] Lebensohn RA, Bringa EM, Caro A. *Continuum mesoscale modelling of nanocrystalline fcc metals under shock-loading using an spectral formulation fed by molecular dynamics results.* Journal De Physique Iv 2006;134:17-22.
[259] Inoue A, Zhang W, Tsurui T, Yavari AR, Greer AL. *Unusual room-temperature compressive plasticity in nanocrystal-toughened bulk copper-zirconium glass.* Philosophical Magazine Letters 2005;85:221-229.
[260] Leonhard A, Xing LQ, Heilmaier M, Gebert A, Eckert J, Schultz L. *Effect of crystalline precipitations on the mechanical behavior of bulk glass forming Zr-based alloys.* Nanostructured Materials 1998;10:805-817.
[261] Louzguine-Lugin DV, Inoue A. *Nano-devitrification of glassy alloys.* Journal of Nanoscience and Nanotechnology 2005;5:999-1014.
[262] Eckert J, Das J, Pauly S, Duhamel C. *Mechanical properties of bulk metallic glasses and composites.* Journal of Materials Research 2007;22:285-301.
[263] Sun YF, Li FS, Guan SK, Tang MQ, Shek CH. *Structural characterization and mechanical properties of nanocrystal-containing Cu-Ti-based bulk metallic glass-forming alloys.* Journal of Materials Research 2007;22:352-357.
[264] Shi YF, Falk ML. *A computational analysis of the deformation mechanisms of a nanocrystal-metallic glass composite.* Acta Materialia 2008;56:995-1000.
[265] Trelewicz JR, Schuh CA. *The Hall-Petch breakdown at high strain rates: optimizing grain size for impact applications.* Applied Physics Letters under review (2008).
[266] Constantinides G, Tweedie CA, Holbrook DM, Barragan P, Smith JF, Van Vliet KJ. *Quantifying deformation and energy dissipation of polymeric surfaces under localized impact.* Materials Science and Engineering: A 2008;489:403-412.
[267] Constantinides G, Tweedie CA, Savva N, Smith JF, Van Vliet KJ. Exp Mech. 2008;in review.
[268] Wei Q. *Strain rate effects in the ultrafine grain and nanocrystalline regimes-influence on some constitutive responses.* Journal of Materials Science 2007;42:1709-1727.
[269] Hollang L, Hieckmann E, Brunner D, Holste C, Skrotzki W. *Scaling effects in the plasticity of nickel.* Materials Science and Engineering a-Structural Materials Properties Microstructure and Processing 2006;424:138-153.
[270] Li YJ, Mueller J, Hoppel HW, Goken M, Blum W. *Deformation kinetics of nanocrystalline nickel.* Acta Materialia 2007;55:5708-5717.
[271] Conrad H. *Plastic deformation kinetics in nanocrystalline FCC metals based on the pile-up of dislocations.* Nanotechnology 2007;18:-.
[272] Lohmiller J, Eberl C, Schwaiger R, Kraft O, Balk TJ. *Mechanical spectroscopy of nanocrystalline nickel near room temperature.* Scripta Materialia 2008;59:467-470.
[273] Detor AJ, Schuh CA. *Microstructural evolution during the heat treatment of nanocrystalline alloys.* Journal of Materials Research 2007;In Press.
[274] Yamasaki T. *High-strength nanocrystalline Ni-W alloys produced by electrodeposition and their embrittlement behaviors during grain growth.* Scripta Materialia 2001;44:1497-1502.

[275] Shi YF, Falk ML. *Stress-induced structural transformation and shear banding during simulated nanoindentation of a metallic glass*. Acta Materialia 2007;55:4317-4324.
[276] Shi YF, Falk ML. *Simulations of nanoindentation in a thin amorphous metal film*. Thin Solid Films 2007;515:3179-3182.
[277] Schuh CA, Packard CE, Lund AC. *Nanoindentation and contact-mode imaging at high temperatures*. 2006;21:725-736.
[278] Conrad H, Wiedersich H. *Activation energy for deformation of metals at low temperatures*. Acta Metallurgica 1960;8:128-130.
[279] Reed-Hill RE, Abbaschian R. Physical metallurgy principles. Boston: PWS-Kent Pub., 1992.
[280] Frost HJ, Ashby MF. Deformation-mechanism maps : the placticity and creep of metals and ceramics. Oxford [Oxfordshire] ; New York: Pergamon Press, 1982.
[281] Tiearney TC, Grant NJ. *Measurement of Structural Parameters Important in Creep of Ni-Mo and Ni-W Solid-Solutions*. Metallurgical Transactions a-Physical Metallurgy and Materials Science 1982;13:1827-1836.
[282] Egami T. *Universal criterion for metallic glass formation*. Materials Science and Engineering a-Structural Materials Properties Microstructure and Processing 1997;226:261-267.
[283] Egami T. *Atomistic mechanism of bulk metallic glass formation*. Journal of Non-Crystalline Solids 2003;317:30-33.
[284] Lewandowski JJ, Greer AL. *Temperature rise at shear bands in metallic glasses*. Nature Materials 2006;5:15-18.
[285] Detor AJ, Miller MK, Schuh CA. *Measuring grain-boundary segregation in nanocrystalline alloys: direct validation of statistical techniques using atom probe tomography*. Philosophical Magazine Letters 2007;87:581-587.
[286] Froseth AG, Derlet PM, Van Swygenhoven H. *Dislocations emitted from nanocrystalline grain boundaries: nucleation and splitting distance*. Acta Materialia 2004;52:5863-5870.
[287] Liao XZ, Srinivasan SG, Zhao YH, Baskes MI, Zhu YT, Zhou F, Lavernia EJ, Xu HF. *Formation mechanism of wide stacking faults in nanocrystalline Al*. Applied Physics Letters 2004;84:3564-3566.